UNIVERSITY OF CALIFORNIA, SAN DIEGO

A Reproducing Kernel Particle Method Framework for Modeling Failure of Structures Subjected to Blast Loadings

A dissertation submitted in partial satisfaction of the
requirements for the degree
Doctor of Philosophy

in

Structural Engineering

by

Guohua Zhou

Committee in Charge:

Professor Jiun-Shyan Chen, Chair
Professor Randolph Bank
Professor Yuri Bazilevs
Professor Hyonny Kim
Professor Pui-Shum Shing

2016

The Dissertation of Guohua Zhou is approved, and it is acceptable in quality and form for publication on microfilm and electronically:

Chair

University of California, San Diego

2016

DEDICATION

To my parents, my brothers, and my girlfriend for their constant love and encouragement.

TABLE OF CONTENTS

SIGNATURE PAGE……..……..….. iii

DEDICATION iv

TABLE OF CONTENTS..... v

LIST OF FIGURES ix

LIST OF TABLES..... xiii

ACKNOWLEDGEMENTS..... xiv

VITA xvi

ABSTRACT OF THE DISSERTATION xviii

Chapter 1 Introduction 1

1.1 Motivation..... 2

1.2 Objectives 4

1.3 Outline..... 5

Chapter 2 Literature Review..... 7

2.1 Shock wave modeling techniques..... 8

2.2 Meshfree methods for shock modeling..... 9

2.3 Meshfree methods for fragment-impact problems..... 10

2.4 Fluid-structure interaction in blast problems 11

Chapter 3 Meshfree Shock Hydrodynamic Formulation I: A Lagrangian Reproducing Kernel Particle Method for Shock Hydrodynamics..... 13

3.1 Introduction..... 14

3.2 Reproducing kernel discretization of Lagrangian hydrodynamics 14

3.2.1 Basic equations..... 14

3.2.2 Lagrangian reproducing kernel (RK) approximation 15

3.2.3 Galerkin approximation..... 17

3.3 The flow solver 20
3.3.1 Local Riemann problem for nodal pairs 20
3.3.2 Calculation of pressure gradient by Lagrangian strain smoothing 23
3.3.3 Solution procedures 25
3.4 Numerical examples 26
3.4.1 One-dimensional Sod shock tube problem 26
3.4.2 One-dimensional Noh implosion problem 28
3.4.3 The Sedov blast wave problem 30
3.4.4 The Dukowicz problem 33
3.5 Conclusion 35
Acknowledgements 36
Chapter 4 Meshfree Shock Hydrodynamic Formulation II: A Godunov-type Shock Capturing Algorithm in Galerkin Meshfree Methods for Solid and Fluid Dynamics 37
4.1 Introduction 38
4.2 Galerkin approximation 38
4.3 Lagragian and semi-Lagrangian discrete formulations 43
4.3.1 Lagrangian RKPM with conforming strain smoothing 43
4.3.2 semi-Lagrangian RKPM with non-conforming strain smoothing for extreme deformation 47
4.4 Flow solver 51
4.5 Time integration procedures 53
4.6 Numerical examples 54
4.6.1 One-dimensional elasto-plastic bar impact 55
4.6.2 Two-dimensional plate impact with rarefaction waves 57
4.6.3 Two-dimensional Noh implosion problem 59

4.6.4 Two-dimensional Sedov blast wave problem..... 62
4.7 Conclusion 66
Acknowledgements..... 67
Chapter 5 A Semi-Lagrangian Reproducing Kernel Particle Method Framework for Modeling Transient Dynamic Failure of Concrete Structures Subjected to Blast Loadings 68
5.1 Introduction..... 69
5.2 High explosive modeling 70
5.2.1 High explosive physics and modeling..... 70
5.2.2 One-dimensional TNT slab explosion with detonation and dispersion 72
5.3 Equivalent shock hugoniot for concrete 74
5.4 Fluid-structure interaction model..... 78
5.4.1 FSI modeling via a contact algorithm 78
5.4.2 1D piston problem 82
5.5 Modeling of a reinforced concrete column under blast loading 84
5.6 Conclusion 88
Acknowledgents..... 88
Chapter 6 Numerical Modeling of Explosive Welding Using Semi-Lagrangian Reproducing Kernel Particle Method 90
6.1 Introduction..... 91
6.2 Impact welding modeling 94
6.2.1 Temperature..... 98
6.2.2 Jet formation..... 99
6.2.3 Straight and wavy interface..... 99
6.3 Explosive welding modeling..... 100

6.4 Conclusion 106
Acknowledgements 108
Chapter 7 Conclusions 109
7.1 Summary of the research performed and the novel contributions 110
7.2 Recommendations for future studies 111
Bibliography 112

LIST OF FIGURES

Figure 1.1. Concrete structures subject to blast loading 2

Figure 1.2. Explosive welding process 3

Figure 3.1. The local Riemann problem defined at the middle point of each nodal pair *IJ* in the current configuration (two-dimensional space case for illustration purpose). 21

Figure 3.2. One single Riemann problem pair *IJ* and velocity decomposition..... 21

Figure 3.3. SNNI non-conforming cells in the undeformed configuration..... 24

Figure 3.4. The results of one-dimensional Sod shock tube problem at time t = 0.2. (a) pressure; (b) velocity; (c) density; (d) internal energy. 27

Figure 3.5. The results of one-dimensional Noh implosion problem at time t = 0.125: (a) pressure; (b) velocity;(c) density; (d) internal energy. 29

Figure 3.6. The result of two-dimensional Sedov problem at time t = 1.0. (a) the deformed node distribution;(b) the scatter plot of density v.s. radial distance in different directions..... 31

Figure 3.7. The initial conditions of the Dukowicz problem. 34

Figure 3.8. The exact solution for the Dukowicz problem. 34

Figure 3.9. The result of Dukowicz problem by using Riemann-SNNI at time t =1.25. (a) the deformed node distribution; (b) the density contour plot. 34

Figure 4.1 The local Riemann problem of nodal pair *I-J* 41

Figure 4.2. (a) Conforming SCNI, and (b) non-conforming SNNI smoothing cells. 45

Figure 4.3. Comparison of Lagrangian and semi-Lagrangian reproducing kernel(RK) shape functions: (a) undeformed configuration, (b) Lagrangian RK in the deformed configuration, and (c) semi-Lagrangian RK in the deformed configuration. 47

Figure 4.4. Schematic diagram for one-dimensional elasto-plastic bar impact..... 56

Figure 4.5. One-dimensional elasto-plastic bar impact, axial stress and velocity distribution t = 6 μsec (a) LAG-SCNI-SHOCK, (b) SEMI-LAG-SNNI-SHOCK and (c) LAG-SCNI. 56

Figure 4.6. Two-dimensional plate impact with rarefaction waves, pressure contours at time t 0.25 μsec (a) LAG-SCNI-SHOCK, (b) SEMI-LAG-SNNI-SHOCK and (c) LAG-SCNI. 59

Figure 4.7. Two-dimensional Noh implosion problem, pressure contours at time t = 0.6, (a) LAG-SCNI SHOCK, and (b) SEMI- LAG-SNNI-SHOCK. (dots represent the nodes in the current configuration)..... 60

Figure 4.8. Two-dimensional Noh implosion problem, the scatter plot of density v.s. radial distance at time t = 0.6, (a) LAG-SCNI-SHOCK, and (b) SEMI- LAG-SNNI-SHOCK. 61

Figure 4.9. Two-dimensional Sedov blast wave problem, pressure contour at time t = 1.0. (dots represent the nodes in the current configuration) 63

Figure 4.10. Two-dimensional Sedov blast wave problem at time t = 1.0, the scatter plot of velocity v.s. radial distance. 64

Figure 4.11. Two-dimensional Sedov blast wave problem at time t = 1.0, the scatter plot of density v.s. radial distance. 64

Figure 4.12. Two-dimensional Sedov blast wave problem at time t = 1.0, density distribution along 45° radial direction using varying discretizations. 65

Figure 5.1. High explosive detonation. 70

Figure 5.2. Schematic Hugoniots and Rayleigh line..... 71

Figure 5.3. 1D high explosive, discretized by meshfree nodes. 72

Figure 5.4. Detonation in a 1D high explosive, TNT. 73

Figure 5.5. The detonation wave and the pressure distributions at t = 10 μsec and t = 20 μsec. 74

Figure 5.6. The equation of state in AFC. model..... 76

Figure 5.7. 1D concrete bar impact with velocity 100 m/sec, axial stress distribution. ... 77

Figure 5.8. Interface of fluid and solid. 78

Figure 5.9. Natural kernel contact algorithm by kernel interaction between contacting fluid domain Ω_F and solid domain Ω_S : (a) fluid is impacting toward solid and (b) kernel overlapping and interacting in the contact zone Ω_C marked as shaded area..... 79

Figure 5.10. Determination of the zero level set and the contact surface normal for contact force calculation..... 81

Figure 5.11. Piston problem..... 83

Figure 5.12. FSI computation: displacement history..... 83

Figure 5.13. (a) Geometry and section details of RC column specimen, (b) test setup configuration (adapted from [66]). 84

Figure 5.14. Pressure contours at different time, (a) time: 0.08 msec, (b) time: 0.12 msec, (c) time: 0.16 msec. 85

Figure 5.15. Tensile damage contour at time: 0.20 msec. 86

Figure 5.16. RC column specimen (a) explosive test (adapted from [66]), (b) numerical result. 87

Figure 6.1. (a) Explosive welding process; (b) geometrical analysis. 92

Figure 6.2. Wavy morphology at the weld interface, (a) Ti-Stainless steel [81]; (b) Brass-Copper [76]; (c) Cu-CP Ti [82]. 93

Figure 6.3. Schematic of impact welding. 94

Figure 6.4. Wavy interface and jet formation at time 2.2 μsec..... 97

Figure 6.5. Pressure distribution at time 2.2 μsec..... 97

Figure 6.6. Velocity distribution at time 2.2 μsec. 98

Figure 6.7. Equivalent plastic strain evolution at straight and wavy areas..... 98

Figure 6.8. Configuration used in explosive welding of capsule..... 100

Figure 6.9. 2D section used for the computation (dimensions in meter); yellow: explosive; blue: flyer and base plates; gray: air. 101

Figure 6.10. Evolution of impact angle β in the simulation of original paper (adapted from [75]). 102

Figure 6.11. Evolution of impact angle β. 103

Figure 6.12. Evolution of impact velocity at the collision point. 104

Figure 6.13. Numerical simulation of the explosive welding process: jetting formation (a) time t = 2.0 μsec, (b) time t = 3.0 μsec, (c) time t = 3.5 μsec..... 104

Figure 6.14. Jetting formation in the original paper (adapted from [75]). 106

LIST OF TABLES

Table 6.1. Material constants for the 6061 T0 aluminum alloy (modified Johnson-Cook model). 96

ACKNOWLEDGEMENTS

I would like to express my deepest and most sincere gratitude to my advisor professor Jiun-Shyan (J.S.) Chen for his patient guidance and constant support throughout this work. It has been a great honor to study under his direction and I am grateful to what I have learnt from him. I would also like to thank my committee members: Professor Randolph Bank, Professor Yuri Bazilevs, Professor Pui-Shum Shing and Professor Hyonny Kim for serving on my committee.

I would also like to thank the colleagues I have worked and discussed research work with and they are, Haoyan Wei, Dr. Yantao Zhang, Dr. Shih-Po Lin, Dr. Michael Hillman, Dr. Edouard Yreux, Qizhi He, Dr. Marcus Rüter, Dr. Camille Marodon, Dr. Ramya Rao Basava, Dr. Yuichi Tadano, Chang Liu, Shixue Liang, Jacob Koester, Frank Beckwith and Marco Pasetto. They are very kind people and always willing to help others. And special thanks is given to Dr. Jason Roth for sharing his research code with me and suggestions for research work.

Chapter 3 is currently being prepared for submission for publication of the material. J.S. Chen, G. Zhou, M. Hillman, 'A Lagrangian Reproducing Kernel Particle Method for Shock Hydrodynamics'. The dissertation author was the primary investigator of this material.

Chapter 4 is currently being prepared for submission for publication of the material. J.S. Chen, G. Zhou, M. Hillman, 'A Godunov-type shock capturing algorithm in Galerkin meshfree methods for solid and fluid dynamics'. The dissertation author was the primary investigator of this material.

Chapter 5 is currently being prepared for submission for publication of the material. J.S. Chen, G. Zhou, ‘A Semi-Lagrangian Reproducing Kernel Particle Method Framework for Modeling Transient Dynamic Failure of Concrete Structures Subjected to Blast Loadings’. The dissertation author was the primary investigator of this material.

Chapter 6 is currently being prepared for submission for publication of the material. J.S. Chen, G. Zhou, ‘Numerical modeling of explosive/impact welding using semi-Lagrangian reproducing kernel particle method’. The dissertation author was the primary investigator of this material.

The sponsorship of this research by the US Army Engineer Research Development Center UCSD is also greatly acknowledged.

Lastly, the most sincere and deepest gratitude to my parents and brothers who always believe in me and support me. I am also grateful to my girlfriend Min, for her constant caring, encouragement and support during this journey.

VITA

2008	Bachelor Degree in Civil Engineering, China Agricultural University, Beijing, China
2012	Master of Engineering, Tsinghua University, Beijing, China
2012-2013	Research Assistant, University of California, Los Angeles
2014-2016	Research Assistant, University of California, San Diego
2016	Doctor of Philosophy, University of California, San Diego

PUBLICATIONS AND PRESENTATIONS

Journal Papers:

J.S. Chen, G. Zhou, M. Hillman, 'A Lagrangian Reproducing Kernel Particle Method for Shock Hydrodynamics', *under preparation*.

J.S. Chen, G. Zhou, M. Hillman, 'A Godunov-type Shock Capturing Algorithm in Galerkin Meshfree Methods for Solid and Fluid Dynamics', *under preparation*.

J.S. Chen, G. Zhou, 'A Semi-Lagrangian Reproducing Kernel Particle Method Framework for Modeling Transient Dynamic Failure of Concrete Structures Subjected to Blast Loadings', *under preparation*.

J.S. Chen, G. Zhou, 'Numerical Modeling of Explosive/impact Welding Using Semi-Lagrangian Reproducing Kernel Particle Method', *under preparation*.

S. Cen, G. Zhou, and X. Fu, 2012. A shape-free 8-node plane element unsymmetric analytical trial function method. *International Journal for Numerical Methods in Engineering*, 91(2), pp.158-185.

S. Cen, X. Fu, G. Zhou, M. Zhou, and C. Li, 2011. Shape-free finite element method: the plane hybrid stress-function (HS-F) element method for anisotropic materials. *Science China Physics, Mechanics and Astronomy*, 54(4), pp.653-665.

S. Cen, M. Zhou, X. Fu, G. Zhou, 2010. A 4-node plane stress-function element with drilling degrees of freedom. *Chinese Journal of Mechanics*. 31.

Abstracts and Presentations

G. Zhou, J.S. Chen, M. Hillman, 'A Riemann-SNNI Galerkin meshfree method for solid and fluid dynamics', *USACM Thematic Conference on Isogeometric Analysis and Meshfree Methods, La Jolla, 2016.*

J.S. Chen, G. Zhou, M. Hillman, E. Yreux, J. Roth, T. Slawson, K. Danielson, 'An oscillation limiting and flux conserving meshfree formulation for shock modeling in nonlinear solids', *World Congress on Computational Mechanics XI, Barcelona,Spain, 2014.*

ABSTRACT OF THE DISSERTATION

A Reproducing Kernel Particle Method Framework for Modeling Failure of Structures Subjected to Blast Loadings

by

Guohua Zhou

Doctor of Philosophy in Structural Engineering

University of California, San Diego, 2016

Professor Jiun-Shyan Chen, Chair

The numerical simulation of transient dynamic failure of structures subjected to blast loadings requires the key physics such as strong shocks in fluid (explosive gas and air) and solid media, fluid-structure interaction, material damage and fragmentations, and multi-body contact to be properly considered in the mathematical formulation and the associated numerical algorithms. These dominant phenomena in blast events yield "rough solution" in the conservation equations in the form of moving discontinuities that cannot be effectively modeled by the conventional finite element methods. A semi-Lagrangian

meshfree Reproducing Kernel Particle Method (RKPM) framework is proposed to model such extreme events in this study. In this work, shock waves in both air and solid are modeled by embedding the Godunov flux into the semi-Lagrangian RKPM formulation in a unified manner. The essential shock physics are introduced in the proposed node-based Riemann solver, and the Gibbs oscillation is limited by introducing a gradient smoothing technique. In this thesis, two formulations are proposed and verified by solving a set of multi-dimensional benchmark problems involving strong shocks in fluids and solids. The air-structure interface is treated by a level set enhanced natural kernel contact algorithm, which does not require the definition of potential contact surfaces *a priori*. The blast-induced fragmentation is simulated by the damage model under the semi-Lagrangian RKPM discretization without using the artificial element erosion technique. Several benchmark problems have been solved to verify the accuracy and performance of the proposed numerical formulation. This computational framework is then applied to the simulation of a reinforced concrete column subjected to blast loading and explosive welding processes, demonstrating the effectiveness and robustness of the proposed methods.

Chapter 1

Introduction

1.1 MOTIVATION

Structures subjected to blast loading (Figure 1.1 and Figure 1.2) cannot be effectively modeled by the conventional mesh-based methods due to the complexity of multiple physics in strong shock waves in both fluid and solid, fluid-structure interaction (FSI), high strain rate phenomenon, and material damage and fragmentations. Reliable and robust numerical simulation techniques of such problems is in high demand in defense and commercial industries and meshfree RKPM approach offers a number of unique features particularly suitable for resolving the said challenges in blast events modeling.

Figure 1.1. Concrete structures subject to blast loading (http://www.nydailynews.com/new-york/authorities-rush-assess-damage-ave-subway-blast-article-1.1141228)

In these events, the material damage and fragmentation typically occur and appear as flying debris from concrete structure or the jetting from explosive welding plates.

Meshfree methods [1, 2, 3] are more suitable for modeling problems with fragmentations compared with mesh-based methods such as finite element method (FEM). These methods build their approximation functions based on a set of scattered nodes instead of the mesh. Therefore they are not plagued by mesh alignment, mesh entanglement and fragmentation occurs naturally governed by the constitutive model due to separation of the particles. Among such, semi-Lagrangian meshfree formulation has been shown effective for modeling impact-fragmentation problems [4, 5]. In order to further tackle the problems involving strong shock waves as mentioned above, the shock physics must be addressed for these methods. Therefore it is desirable to develop a physics-based shock modeling technique for simulation of these extreme events involving shock-induced fragmentations.

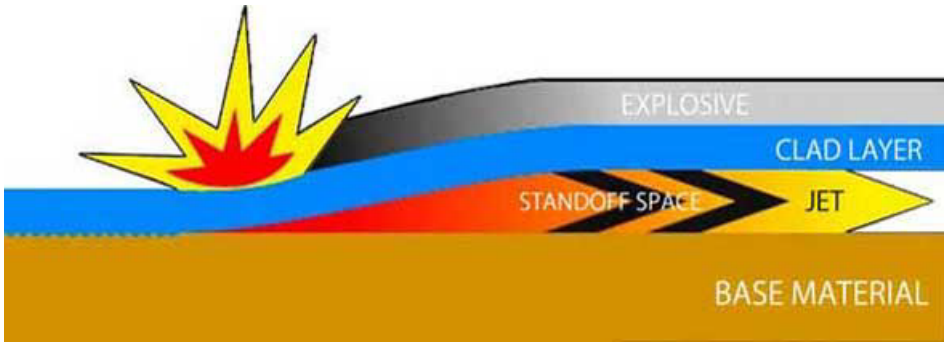

Figure 1.2. Explosive welding process
(http://smt-holland.com/#/explosive_cladding).

Numerically, these fragmentations break the description of the original surfaces and create countless new surfaces, which add the complexity to the FSI scheme. It is common to use an arbitrary-Lagrangian– Eulerian (ALE) formulation for the FSI [6, 7]. However, when fragmentations occur in the concrete structure under blast loadings, ALE methods often flounder because it is difficult to have a robust scheme to move the fluid mesh to accommodate the deformation of the structure where the material separation takes place.

On the other hand, Lagrangian solid and Eulerian fluid can be directly coupled by using Lagrange multipler method or penalty method [8]. However effort must be spent on the interface description, such as using level set method, which could be tedious when countless pieces of debris occur. An effective scheme is required to be developed to handle FSI with the fragmentations.

1.2 OBJECTIVES

The objective of this work is to develop a Reproducing Kernel Particle Method framework for modeling transient dynamic failure of structures under blast loadings. The major tasks of this dissertation are summarized as follows:

- Development of physics-based shock modeling techniques under RKPM meshfree framework for both fluids and solids. Two formulations are proposed to embed the Godunov flux into the RKPM formulation. The Gibbs oscillation control are performed by a gradient smoothing technique in pressure and velocity gradients. The numerical formulations are verified by solving several multi-dimensional benchmark problems involving strong shocks. The proposed approach is applied to model shock-induced fragmentations.
- Development of a meshfree FSI scheme. The fluid-structure interface is treated by the level set enhanced natural kernel contact algorithm, which does not require the definition of potential contact surfaces *a priori*. This approach doesn't require any surface tracking technique, mesh moving or re-meshing scheme, and is applicable to FSI with solid fragmentations.
- Application of this framework to model transient dynamic failure of concrete structures subject to blast loading. A reinforced concrete column subject to blast loading is modeled in this work. The simulation results and experimental data are

in good agreement.

- Application of this framework to model explosive welding. Both impact welding and explosive welding are studied. The numerical results show that the key phenomena are properly captured.

1.3 OUTLINE

The dissertation has been divided into seven chapters. They are outlined as follows:

Chapter 1 discusses the motivation, objectives and outline of this dissertation.

Chapter 2 gives an overview on shock wave modeling techniques, meshfree methods for shock modeling, meshfree methods for fragmentation-impact problems and FSI in blast problems.

Chapter 3 presents the first formulation for shock modeling under RKPM, 'Meshfree Shock Hydrodynamic Formulation I: A Lagrangian Reproducing Kernel Particle Method for Shock Hydrodynamics'. In this formulation, the Godunov flux is embedded into the RKPM formulation by defining the Riemann problem at the middle point of each nodal pair within the domain of influence along the axial direction. And RK gradient approximation is employed to obtain the pressure and energy gradients. It is verified by solving a set of multi-dimensional benchmark problems with strong shock waves.

Chapter 4 presents the second formulation for shock modeling under RKPM, 'Meshfree Shock Hydrodynamic Formulation II: A Godunov-type Shock Capturing Algorithm in Galerkin Meshfree Methods for Solid and Fluid dynamics'. Different from the scheme in Chapter 3, Godunov flux is embedded into the RKPM formulation by defining the Riemann problem based on the node-based flux gradient evaluation technique. This formulation is capable to solve problems involving both shocks and fragmentations.

It is verified by solving several multi-dimensional benchmark problems with strong shock waves in solids and fluids.

Chapter 5 is dedicated to present a framework for modeling transient dynamic failure of concrete structures subject to blast loadings. It includes the details about modeling of high explosive, equivalent shock Hugoniot of concrete material and FSI. Each part is validated by solving corresponding bench mark problems. Finally, the simulation results are compared with experimental data and they are in good agreement.

Chapter 6 applies the framework developed in Chapter 5 to further model explosive/impact welding. The key phenomena, wavy interface and jetting are reproduced quite well in the simulation. And the results are compared with the theoretical prediction and other publications, and they are in good agreement.

Chapter 7 summarizes the research work performed, emphasizes the important original contributions, and discusses future research directions and recommendations.

Chapter 2

Literature Review

2.1 SHOCK WAVE MODELING TECHNIQUES

Shock wave is a propagation of discontinuities in pressure, density, temperature and velocity, and is an essential physics involved in high velocity impact and blast problems which must be carefully addressed. Artificial shock viscosity [9] and Godunov scheme [10] are two main approaches for modelling shocks and are widely used in different methods. von Neumann and Richtmyer [9] introduced the concept of artificial shock viscosity in 1950 permitted for the first time to practically deal with the problems involving strong shock waves. In the formulation, the artificial viscosity is considered as an extra artificial pressure term, added to the conservation of momentum and energy equations. In this manner, the shock wave front is spread over several computational cells depending on the viscosity magnitude. Artificial viscosity techniques are widely used in different methods, such as in finite element methods (FEMs) [11, 12, 13, 14, 15, 16], isogeometric analysis (IGA) [17] and Smoothed particle hydrodynamics (SPH) [18]. Proper selection of artificial viscosity coefficients for sharp and non-oscillatory shock profiles is an essential shortcoming of this method.

Godunov's method proposed by Godunov in 1959 [10] introduces the Riemann problem (RP) solution to resolve discontinuities at the interfaces between cells in finite volume method (FVM). In this method, all quantities in a computational cell are assumed constant given by the cell average. As a result, there are discontinuities across the cell boundaries which form the RP and the solution of RP provides the driving flux. The great advantage of this method is that the essential shock physics are considered and consequently it is free of problem-dependent parameters. Originally, it is only first-order accurate due to the piece-wise constant assumption in each cell. Later, van Leer [19, 20] improved the accuracy to second-order by representing the distribution of variables in each

cell using a piece-wise linear distribution rather than uniform except at the shock front, limited in such a way to preserve monotonicity. This higher order improvement by van Leer popularize Godunov scheme in the computational fluid dynamics community. And later essentially non-oscillatory scheme (ENO) [21] and weighted essentially non-oscillatory schemes (WENO) [22] scheme are proposed to further improve the accuracy.

2.2 MESHFREE METHODS FOR SHOCK MODELING

To address shock physics, Godunov scheme which is originally proposed in finite volume method, has been introduced into the meshfree methods [23, 24, 25, 26, 27, 28, 29]. Inutsuka [26] and, Cha and Whitworth [23] independently proposed the so-call Godunov-type SPH (GSPH) method. In this method, the force acting on each particle is determined by the RP solutions. And the use of the Riemann solver is introduced in a simple analogy of the grid-based method such as FVM. However, on its own this technique of introducing RP solution does not eliminate other low-order SPH errors, in particular the so-called 'E0' zeroth-order error [30] and those errors can de-stabilize the solution [31]. In [32], Luo *et al* developed an edge-based upwind finite element scheme in which the standard weak form is manipulated into a finite volume form and the Roe's numerical flux function is used to replace the original unstable flux to perform an upwind effect. Later, Löhner *et al* extended the idea in [32] to finite point method [28]. In [25, 27], the authors proposed the so-called finite volume particle method (FVPM) and claimed that the meshfree method can be treated as the classic finite volume method with the difference that the geometrical coefficients (cell volume, surface and normal vector) are calculated implicitly via domain integrals rather than given by physical cells. FVPM depends crucially on the accuracy of this integral which can be performed by numerical integration [33, 30].

An acceptable accuracy of these geometrical coefficient integrals is computationally expensive.

Under the Galerkin meshfree framework, a Riemann-SCNI method [34, 35] has been developed to introduce Godunov scheme into the Reproducing Kernel Particle Method (RKPM) [2, 36] by defining local Riemann problems at the interfaces of stabilized conforming nodal integration (SCNI) [37] smoothing cells when performing pressure gradient smoothing. However, it requires a conforming Voronoi discretization and therefore is difficult to be applied for modelling shock-induced fragmentation problems.

2.3 MESHFREE METHODS FOR FRAGMENT-IMPACT PROBLEMS

Belytschko *et al* [38] modeled the impact-penetration problem using FEM. In order to deal with mesh distortion and fragmentations, the element erosion model [38] is employed. This approach is simple but introduces errors in mass conservation, as well as in energy and momentum conservations. On the other hand, it causes numerical diffusion of material damage and leads to artificial material degradation inconsistent with the physical material damage.

In comparison with mesh-based methods, meshfree methods [1, 2, 3] are more suitable for modelling problems involving fragmentations. These methods construct the approximation based on a set of scattered nodes without the connectivity between them (mesh). Therefore, they are not plagued by mesh alignment, mesh entanglement, time-consuming mesh generation, and other issues related to mesh-based methods. In particular, fragmentations occur naturally due to material damage and the separation of particles. The SPH has been applied for simulations of hypervelocity impact and fragmentation [39, 40, 41, 42]. However, the aforementioned instability, lack of linear consistency, and the

existence of zero-energy modes [39] are the common issues in SPH methods that require additional treatments and modifications.

The reproducing kernel particle method (RKPM) [2, 36] was proposed as a correction to SPH in recovering the consistency conditions that are not satisfied in the conventional SPH method. In particular, semi-Lagrangian RKPM [43] has been proposed to model extremely large deformation problems and successfully applied to earth moving simulations [5] and the impact and fragmentation problems [4, 44]. And recently there are further progresses made on this method for modeling fragment-impact problems: the quasi-linear reproducing kernel particle method [45] to improve the accuracy during the linear to constant basis transition; the accelerated, convergent, and stable nodal integration in Galerkin meshfree methods [46] to improve the efficiency and stability; and the level set enhanced natural kernel contact algorithm [44] to improve the accuracy in the contact algorithm for problems involving fragmentations.

2.4 FLUID-STRUCTURE INTERACTION IN BLAST PROBLEMS

In modelling structures under blast loadings, compressible fluid-structure interaction (FSI) severs as the mechanism to impart the strong shock wave from fluid to solid, and requires to be addressed carefully. Structures are typically described by the Lagrangian formulation where it avoids the numerical difficulty associated with convective transport terms and a precise definition of moving boundaries is straightforward. In [47], it also models the compressible fluid with Lagrangian formulation and however large flow distortions lead to the element entanglement. Therefore, usually the fluid is described by Eulerian formulation where the mesh is fixed. Arbitrary-Lagrangian-Eulerian (ALE) formulation is a common framework used for the compressible FSI [6, 7]. An important

ingredient of ALE formation is the mesh-updating algorithm used to adjust the fluid mesh to accommodate the structure deformation. ALE formulation can satisfy the interface condition accurately since the interface is well preserved by Lagrangian description. However, if fragmentations occur in the structure as in blast problems, ALE methods often flounder because it is difficult to have a robust scheme to move the fluid mesh to match the deformation of the structure where the surface cracking and fragmentations take place. Legay et al [8] directly coupled Lagrangian solid and Eulerian fluid by using Lagrange multipler method and penalty method. This approach does not require to update the mesh since it is fully Eulerian description in fluid domain. And efforts must be spent on the interface tracking, such as using Level set method as in [8]. However under the circumstance of concrete structures subjected to near-field detonation as shown in Figure 1.1, there are countless pieces of debris (fragmentations) to be tracked, which is tedious.

Chapter 3

Meshfree Shock Hydrodynamic Formulation I: A Lagrangian Reproducing Kernel Particle Method for Shock Hydrodynamics

3.1 INTRODUCTION

A Lagrangian description of the Reproducing Kernel Particle Method (RKPM) is proposed for modeling shock hydrodynamics. The weak forms of the compressible hydrodynamic equations are discretized by a set of scattered nodes without any background mesh for discretization or domain integration. Shock physics is embedded into the formulation by computing the pressure gradient using the Riemann problem solution in conjunction with gradient smoothing, which also precludes the Gibbs phenomenon. Correspondingly, the weak form of hydrodynamics is integrated using Stabilized Nonconforming Nodal Integration (SNNI) with the embedded Riemann solution, and is termed Riemann-SNNI. The performance of the proposed method for shock dynamics is examined by solving a set of benchmark problems, where results are attained with good accuracy.

This chapter is organized as follows. In section 2, the reproducing kernel discretization of the Lagrangian hydrodynamic equations is presented. In section 3, the compressible flow solver for shock physics under the RKPM framework is introduced. Numerical results are presented in section 4 to demonstrate the effectiveness of the proposed method, and conclusions and discussions are given in section 5.

3.2 REPRODUCING KERNEL DISCRETIZATION OF LAGRANGIAN HYDRODYNAMICS

3.2.1 Basic equations

This work solves the Euler equations of compressible hydrodynamics in the Lagrangian description. We denote by $\Omega_t \in \Re^{n_{sd}}$ the configuration of the problem material

domain at time t, where n_{sd} is the number of spatial dimensions. The domain $\Omega_0 \in \Re^{n_{sd}}$ represents the initial configuration at time $t = 0$. We denote by $\mathbf{x}$ and $\mathbf{X}$ the particle positions in Ω_t and Ω_0 respectively, and the mapping $\boldsymbol{\varphi}$ between the two is $\mathbf{x} = \boldsymbol{\varphi}(\mathbf{X}, t)$. Denote $\mathbf{u}$ as the displacement vector where $\mathbf{u}(\mathbf{X}, t) = \mathbf{x}(\mathbf{X}, t) - \mathbf{X}$.

Without loss of generality, Lagrangian forms of the conservation equations of compressible hydrodynamics in the absence of body force and heat conduction in Ω_t are

$$\rho^{(0)} = \rho \det(\mathbf{F}), \tag{3.1}$$

$$\rho \frac{\mathrm{d}\mathbf{v}}{\mathrm{d}t} = \nabla^{\mathbf{x}} \cdot \boldsymbol{\sigma}, \tag{3.2}$$

$$\rho \frac{\mathrm{d}E}{\mathrm{d}t} = -\nabla^{\mathbf{x}} \cdot (\mathbf{v} \cdot \boldsymbol{\sigma}), \tag{3.3}$$

where $\rho^{(0)}$ and ρ are the densities in the initial and current configuration respectively, $\mathrm{d}(\,)/\mathrm{d}t$ denotes material time derivative, $\mathbf{v} = \mathrm{d}\mathbf{u} / \mathrm{d}t$ is the velocity vector, $\nabla^{\mathbf{x}}$ denotes the gradient with respect to $\mathbf{x}$, $\boldsymbol{\sigma}$ is the Cauchy stress tensor, E is the total energy per unit mass, $\det(\mathbf{F})$ is the determinant of the deformation gradient tensor $\mathbf{F} = \partial \mathbf{x} / \partial \mathbf{X}$, and $E = e + \mathbf{v} \cdot \mathbf{v} / 2$ is the total energy density, where e is the internal energy density.

3.2.2 Lagrangian reproducing kernel (RK) approximation

The Lagrangian RK approximation of displacement $\mathbf{u}$, denoted as $\mathbf{u}^h$, is constructed using the material coordinate $\mathbf{X}$ as

$$\mathbf{u}^h(\mathbf{X}, t) = \sum_{I \in \text{supp}(\mathbf{X})} \Psi_I(\mathbf{X}) \mathbf{d}_I(t), \tag{3.4}$$

where $\Psi_I(\mathbf{X})$ and $\mathbf{d}_I(t)$ are the RK shape function and the generalized coordinate of

the *I*-th node respectively, the set supp(**X**) is defined as,

$$\text{supp}(\mathbf{X}) = \left\{ I \,\middle|\, \Psi_I(\mathbf{X}) \neq 0 \right\}. \tag{3.5}$$

The shape function is constructed as a correction to a kernel function $\phi_a(\mathbf{X}-\mathbf{X}_I)$ with a compact support *a*,

$$\Psi_I(\mathbf{X}) = C(\mathbf{X};\mathbf{X}-\mathbf{X}_I)\phi_a(\mathbf{X}-\mathbf{X}_I), \tag{3.6}$$

where the kernel function $\phi_a(\mathbf{X}-\mathbf{X}_I)$ is a positive function, which defines the locality and order of the smoothness of the approximation:

$$\begin{cases} \phi_a(\mathbf{X}-\mathbf{X}_I) \geq 0, & |\mathbf{X}-\mathbf{X}_I| \leq a \\ \phi_a(\mathbf{X}-\mathbf{X}_I) = 0, & |\mathbf{X}-\mathbf{X}_I| > a \end{cases}, \tag{3.7}$$

where '$|\ |$' denotes the distance measure. The function $C(\mathbf{X};\mathbf{X}-\mathbf{X}_I)$ is a correction function which is a linear combination of complete *n*-th order monomials as

$$\begin{aligned} C(\mathbf{X};\mathbf{X}-\mathbf{X}_I) &= \sum_{i+j+k=0}^{n} b_{ijk}(\mathbf{X})(X_1-X_{I1})^i(X_2-X_{I2})^j(X_3-X_{I3})^k \\ &= \mathbf{H}^T(\mathbf{X}-\mathbf{X}_I)\mathbf{b}(\mathbf{X}), \end{aligned} \tag{3.8}$$

$$\mathbf{H}^T(\mathbf{X}-\mathbf{X}_I) = \begin{bmatrix} 1 & X_1-X_{I1} & X_2-X_{I2} & X_3-X_{I3} & (X_1-X_{I1})^2 & \cdots & (X_3-X_{I3})^n \end{bmatrix}, \tag{3.9}$$

where $b_{ijk}(\mathbf{X})$ is the coefficient of the basis function, and $\mathbf{H}(\mathbf{X}-\mathbf{X}_I)$ and $\mathbf{b}(\mathbf{X})$ are vectors of the basis functions and the associated coefficients, respectively. The coefficient vector $\mathbf{b}(\mathbf{X})$ is obtained by enforcing the reproducing conditions of monomial bases up to *n*-th order,

$$\sum_{I \in \text{supp}(\mathbf{X})} \Psi_I(\mathbf{X}) X_{I1}^i X_{I2}^j X_{I3}^k = X_1^i X_2^j X_3^k, \quad i+j+k = 0,1,\cdots,n, \tag{3.10}$$

which is equivalent to the following equation

$$\sum_{I\in \mathrm{supp}(\mathbf{X})} \Psi_I(\mathbf{X})\left(X_1 - X_{I1}\right)^i \left(X_2 - X_{I2}\right)^j \left(X_3 - X_{I3}\right)^k = \delta_{i0}\delta_{j0}\delta_{k0},\ \ i+j+k = 0,1,\cdots,n, \quad (3.11)$$

where δ is the Kronecker delta. Expressing the above equation in matrix form, we have

$$\sum_{I\in \mathrm{supp}(\mathbf{X})} \Psi_I(\mathbf{X})\mathbf{H}^T(\mathbf{X}-\mathbf{X}_I) = \mathbf{H}^T(\mathbf{0}). \quad (3.12)$$

Combining equation (3.6), (3.8) and (3.12) yields

$$\mathbf{b}(\mathbf{X}) = \mathbf{M}^{-1}(\mathbf{X})\mathbf{H}(\mathbf{0}), \quad (3.13)$$

where $\mathbf{M}(\mathbf{X})$ is the so-called moment matrix

$$\mathbf{M}(\mathbf{X}) = \sum_{I\in \mathrm{supp}(\mathbf{X})} \mathbf{H}(\mathbf{X}-\mathbf{X}_I)\mathbf{H}^T(\mathbf{X}-\mathbf{X}_I)\phi_a(\mathbf{X}-\mathbf{X}_I). \quad (3.14)$$

By substituting equation (3.13) into (3.8) the correction function $C(\mathbf{X};\mathbf{X}-\mathbf{X}_I)$ is obtained, and consequently the RK shape function is constructed as

$$\Psi_I(\mathbf{X}) = \mathbf{H}^T(\mathbf{0})\mathbf{M}^{-1}(\mathbf{X})\mathbf{H}(\mathbf{X}-\mathbf{X}_I)\phi_a(\mathbf{X}-\mathbf{X}_I). \quad (3.15)$$

The kernel function $\phi_a(\mathbf{X}-\mathbf{X}_I)$ defines the order of smoothness and the locality, and the basis function vector $\mathbf{H}(\mathbf{X}-\mathbf{X}_I)$ controls the order of completeness of the approximation.

3.2.3 Galerkin approximation

For convenience we choose the updated Lagrangian form of the weak statement of the problem, which is more natural in the treatment of shocks via the Reimman problem. The weak form for conservation of linear momentum (i.e. equation (3.2)) with reference as the current configuration is: find $\mathbf{v} \in H_g^1$, such that $\forall \mathbf{w} \in H_0^1$:

$$\int_{\Omega_t} \rho \mathbf{w} \cdot \frac{\mathrm{d}\mathbf{v}}{\mathrm{d}t} \mathrm{d}\Omega + \int_{\Omega_t} \nabla^{\mathbf{x}} \mathbf{w} : \boldsymbol{\sigma} \mathrm{d}\Omega - \int_{\Gamma_t^h} \mathbf{w} \cdot \mathbf{h} \mathrm{d}\Gamma = 0, \tag{3.16}$$

where Γ_t^h denotes the natural boundary in the current configuration, and **h** is the traction vector on Γ_t^h.

Note that in hydrodynamics, the pressure dominates the shock behavior. To treat the pressure portion of the shocks using a Godunov scheme, the Cauchy stress tensor $\boldsymbol{\sigma}$ is decomposed into deviatoric and volumetric parts

$$\boldsymbol{\sigma} = \boldsymbol{\sigma}^{\mathrm{d}} + \boldsymbol{\sigma}^{\mathrm{v}}, \tag{3.17}$$

where $\boldsymbol{\sigma}^{\mathrm{v}} = \frac{1}{3}\left(\sigma_{11} + \sigma_{22} + \sigma_{33}\right)\mathbf{I}$ (**I** is the identity tensor), and $\boldsymbol{\sigma}^{\mathrm{d}} = \boldsymbol{\sigma} - \boldsymbol{\sigma}^{\mathrm{v}}$.

The weak form is then expressed with volumetric and deviatoric decomposition of the stress, and the volumetric part of the internal force is integrated by parts to obtain:

$$\int_{\Omega_t} \rho \mathbf{w} \cdot \frac{\mathrm{d}\mathbf{v}}{\mathrm{d}t} \mathrm{d}\Omega + \int_{\Omega_t} \nabla^{\mathbf{x}} \mathbf{w} : \boldsymbol{\sigma}^{\mathrm{d}} \mathrm{d}\Omega - \int_{\Omega_t} \mathbf{w} \cdot \left(\nabla^{\mathbf{x}} \cdot \boldsymbol{\sigma}^{\mathrm{v}}\right) + \int_{\Gamma_t^h} \mathbf{w} \cdot (\mathbf{n} \cdot \boldsymbol{\sigma}^{\mathrm{v}} - \mathbf{h}) \mathrm{d}\Gamma \mathrm{d}\Omega = 0. \tag{3.18}$$

Note that an additional term on the boundary has appeared in the formulation; the last term in the above represents the weak enforcement of natural boundary conditions inherent in the employment of the weak form. The weak form (3.18) is applicable to both solid and fluid if a suitable constitutive material law or equation of state is provided. For compressible flow, the pressure is given by an equation of state (EOS). For example, the EOS of ideal gas can be described by

$$P = \left(\gamma - 1\right)\rho e. \tag{3.19}$$

here γ is the adiabatic index, assumed to be constant for a given gas. Without loss of generality, in this work we consider the inviscid flow case where

$$\boldsymbol{\sigma} = \boldsymbol{\sigma}^{\mathrm{v}} = -P\mathbf{I}, \tag{3.20}$$

where P is the pressure.

The Galerkin approximation of (3.18) with inviscid flow asks to find $\mathbf{v}^h \in S^h$, such that $\forall \mathbf{w}^h \in V^h$:

$$\int_{\Omega_t} \rho \mathbf{w}^h \cdot \frac{\mathrm{d}\mathbf{v}^h}{\mathrm{d}t} \mathrm{d}\Omega + \int_{\Omega_t} \mathbf{w}^h \cdot \left(\nabla^{\mathrm{x}} P\right) \mathrm{d}\Omega - \int_{\Gamma_t^h} \mathbf{w}^h \cdot (P\mathbf{n} - \mathbf{h}) \mathrm{d}\Gamma = 0. \tag{3.21}$$

where $S^h \subset H_g^1$ and $V^h \subset H_0^1$. Note that kinematically admissible meshfree approximations can be constructed by e.g., the transformation method [36], or boundary singular kernel method [48]. In this work we employed the latter. The energy equation (3.3) and conservation of mass equation (3.1) is not discretized, but instead enforced strongly at each node. We choose to formulate the Galerkin approximation under the framework of nodal integration, when, if treated properly, can provide a stable, accurate, and efficient means to perform domain integration, and is far more efficient than Gaussian integration [37, 49, 46]. With the employment of nodal integration, the numerical integration of the Galerkin equation (3.21) is expressed as

$$\mathbf{M}\mathbf{a} + \mathbf{f}^{\mathrm{int}} - \mathbf{f}^{\mathrm{ext}} - \mathbf{f}^{\mathrm{g}} = 0 \tag{3.22}$$

where $\mathbf{a} = \mathrm{d}\mathbf{v} / \mathrm{d}t$, and

$$\begin{aligned}
\mathbf{M}_I &= \sum_{L=1}^{NP} \rho(\mathbf{x}_L) \mathbf{I} \Psi_I(\mathbf{x}_L) V_L \\
\mathbf{f}_I^{\mathrm{int}} &= \sum_{L=1}^{NP} \Psi_I(\mathbf{x}_L) \overline{\nabla}^{\mathrm{x}} P_L^* V_L \\
\mathbf{f}_I^{\mathrm{ext}} &= \sum_{L=1}^{NPh} \Psi_I(\mathbf{x}_L) \mathbf{h} S_L \\
\mathbf{f}_I^{\mathrm{g}} &= \sum_{L=1}^{NPh} \Psi_I(\mathbf{x}_L) (-P\mathbf{n}) S_L
\end{aligned} \tag{3.23}$$

where NP is the total number of nodes, V_I is the volume for node I in the current configuration, S_L is the L-th weight of the NPh integration points on the natural boundary

in the current configuration, and $\overline{\nabla}^{\mathbf{x}} P_L^* \equiv \overline{\nabla}^{\mathbf{x}} P^*(\mathbf{X}_L)$ is the smoothed pressure gradient at node L which has been substituted for $\nabla^{\mathbf{x}} P(\mathbf{X}_L)$, calculated by embedding shock physics under the strain smoothing framework as will be discussed in section 3. In this dissertation, '$-$' is used to denote smoothed terms. In the discrete equations (3.23), mass lumping has been employed in conjunction with the partition of unity of the shape functions.

Note that in the Lagrangian RK approximation given, if the reference configuration is chosen as current configuration as in equation (3.16), mapping $\mathbf{x}$ to the material configuration via $\mathbf{X} = \boldsymbol{\varphi}^{-1}(\mathbf{x}, t)$ is, in theory necessary to construct the approximation. However since quantities are evaluated at fixed material points in the Lagrangian description, the mapping does not actually need to be performed. Spatial derivatives can be constructed implicitly by chain rule rather than directly as discussed in section 3.

3.3 THE FLOW SOLVER

In this section, we show how the pressure gradient term in equation (3.23) is evaluated, how the energy equation (3.3) is solved, and how the density and pressure are updated.

3.3.1 Local Riemann problem for nodal pairs

In the finite volume method and Riemann-SCNI [35, 34], the pressure gradient is computed by performing a contour integral over the boundaries of a control volume. At each cell boundary, the Godunov flux [50] based on the local Riemann problem solution is computed by satisfying the Rankine-Hugoniot jump equations. In meshfree methods,

efforts have been made to bring in the spirit of Godunov scheme, such as the work in [23, 24, 25, 26, 27, 28, 29]. One common feature of these work is that midpoints between nodes are treated as the 'boundary' and the flux is evaluated there. In this work, we adopt the same approach by defining the Riemann problem at the midpoint of each nodal pair in the current configuration.

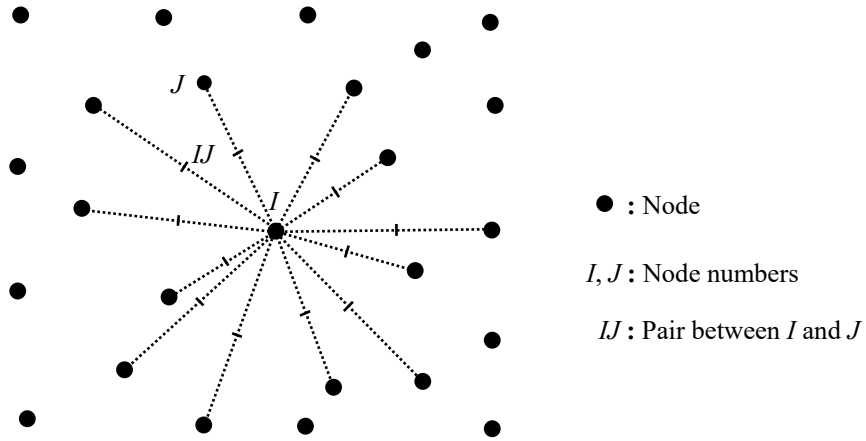

Figure 3.1. The local Riemann problem defined at the middle point of each nodal pair *IJ* in the current configuration (two-dimensional space case for illustration purpose).

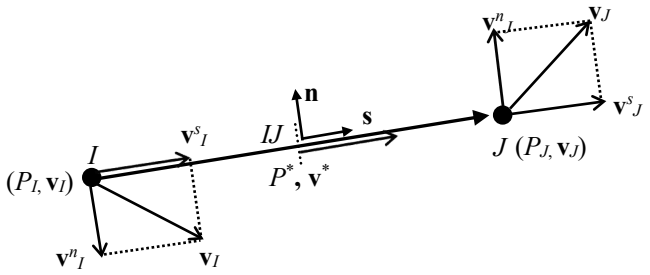

Figure 3.2. One single Riemann problem pair *IJ* and velocity decomposition.

Different from in Riemann-SCNI where the Riemann Problem is defined at the cell boundaries, here the local Riemann Problem is defined at the middle point of each nodal

pair in the current configuration as shown in Figure 3.1. In this work we consider pairing only nodes *J* within the support of a given node *I*, denoting each node in the set with as pair *IJ*. For each pair *IJ*, we define a local Riemann Problem at the middle point between the pair, as shown in Figure 3.2. In this work, the non-iterative Riemann solver by Dukowicz [51] is adopted to solve the problem.

The Riemann problem is defined as: given the left state $\{P_L,\ v_L,\ \rho_L\}$ and the right state $\{P_R,\ v_R,\ \rho_R\}$, solve for the pressure *P** and velocity *v** at the interface. In this work, the subscripts '*L*' and '*R*' denote the left and right state variables, respectively. By using Dukowicz Riemann solver [51], the velocity *v** is obtained by solving the following semi-quadratic equation,

$$\rho_L B_L \left|v^* - v^*_{\min}\right|\left(v^* - v^*_{\min}\right) + \rho_R B_R \left|v^* - v^*_{\max}\right|\left(v^* - v^*_{\max}\right) + P^*_L - P^*_R = 0, \quad (3.24)$$

where

$$\begin{aligned} &v^*_{\min} = v_L - 0.5C_L / B_L, \qquad v^*_{\max} = v_R + 0.5C_R / B_R; \\ &P^*_L = P_L - 0.25\rho_L (C_L)^2 / B_L, \qquad P^*_R = P_R - 0.25\rho_R (C_R)^2 / B_R. \end{aligned} \quad (3.25)$$

Here *C* is the sound speed, and *B* is a parameter directly related to the shock density ratio in the limit of strong shocks. For an ideal gas $B = (\gamma+1)/2$. The details of selecting *B* are given in [51]. After the velocity *v** is solved, the pressure *P** can be easily obtained by the following equation,

$$P^* = \frac{1}{2}\left(P^*_R + P^*_L\right) + \frac{1}{2}\rho_L B_L \left|v^* - v^*_{\min}\right|\left(v^* - v^*_{\min}\right) - \frac{1}{2}\rho_R B_R \left|v^* - v^*_{\max}\right|\left(v^* - v^*_{\max}\right). \quad (3.26)$$

Thus, this Riemann solver is non-iterative and efficient.

For the interacting pair of node *I* and *J*, we employ the Riemann solution *P** and *v** as the corrected midpoint pressure and velocity fields as

$$P^*_{IJ} = P^*, \quad (3.27)$$

$$\mathbf{v}_{IJ}^{*} = \mathrm{v}^{*}\,\mathbf{s} + \frac{\mathbf{v}_I^n + \mathbf{v}_J^n}{2}, \tag{3.28}$$

where **s** is the unit vector connecting nodes *I* and *J*, and $\mathbf{v}_I^n$ and $\mathbf{v}_J^n$ are the transverse velocity components at nodes *I* and *J*, respectively, as shown in Figure 3.2.

3.3.2 Calculation of pressure gradient by Lagrangian strain smoothing

Since the direct nodal derivative can yield unstable solutions due to severe underestimation of short-wavelength modes [37], here we compute smoothed gradients using the Stabilized Nonconforming Nodal Integration (SNNI) [4, 5] to enhance the numerical stability. The basic idea of the SNNI gradient is that instead of directly taking a derivative at the node, the gradient is averaged over a nodal domain and converted to a contour integral [4, 5]. The SNNI gradient of the shape function Ψ_J with respect to $\mathbf{X}_I$, denoted as $\bar{\nabla}^{\mathrm{x}}\Psi_J(\mathbf{X}_I)$, is

$$\bar{\nabla}^{\mathrm{x}}\Psi_J(\mathbf{X}_I) = \frac{1}{A_I}\int_{\Omega_I} \nabla^{\mathrm{x}}\Psi_J(\mathbf{X})\,d\Omega \approx \frac{1}{A_I}\sum_{K\in E_I} \Psi_J(\mathbf{X}_K)\,L_K\mathbf{N}_K, \tag{3.29}$$

where in two-dimensional space case (see Figure 3.3), Ω_I is the smoothing cell associated with node *I*, the set E_I is a set containing all the edges surrounding the smoothing cell Ω_I, A_I is the area of Ω_I, $\mathbf{X}_K$ is the coordinate of the evaluation point on the edge *K*, L_K and $\mathbf{N}_K$ are the edge length and outward normal vector respectively. Although the inverse mapping to calculate Lagrangian shape functions can be avoided since all evaluation points are fixed material points, spatial derivatives are still required for the

updated Lagrangian formulation. To avoid computing spatial derivatives directly, $\bar{\nabla}^{\mathbf{x}}\Psi_J(\mathbf{X}_I,t)$ can be obtained implicitly by the chain rule,

$$\bar{\nabla}^{\mathbf{x}}\Psi_J(\mathbf{X}_I)=\bar{\mathbf{F}}^{-T}(\mathbf{X}_I)\cdot\bar{\nabla}^{\mathbf{X}}\Psi_J(\mathbf{X}_I), \tag{3.30}$$

where $\bar{\mathbf{F}}^{-1}$ is computed by taking the inverse of the smoothed deformation gradient tensor $\bar{\mathbf{F}}$ calculated point-wise as [52]:

$$\bar{\mathbf{F}}(\mathbf{X}_I,t)=\sum_{J\in\mathrm{supp}(\mathbf{X}_I)}\bar{\nabla}^{\mathbf{X}}\Psi_J(\mathbf{X}_I)\otimes\mathbf{x}_J(\mathbf{X}_J,t). \tag{3.31}$$

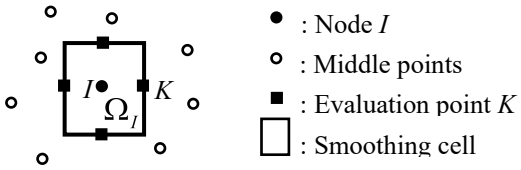

Figure 3.3. SNNI non-conforming cells in the undeformed configuration

The pressure gradient with respect to the current spatial coordinate at each node can be approximated as

$$\bar{\nabla}^{\mathbf{x}}P_I^*=2\sum_{J\in\mathrm{supp}(\mathbf{X}_I)}\bar{\nabla}^{\mathbf{x}}\Psi_J(\mathbf{X}_I)P_{IJ}^*, \tag{3.32}$$

where $\bar{\nabla}^{\mathbf{x}}P_I^*\equiv\bar{\nabla}^{\mathbf{x}}P^*(\mathbf{X}_I)$ and P_{IJ}^* is the pressure associated with the *IJ* pair. In arriving at the above, we have assumed the mapping near node *I* is affine, such that the midpoint remains the midpoint after the local deformation. The factor of two naturally comes from the fact that a set of shape functions constructed at the midpoints can be calculated simply by scaling $\bar{\nabla}^{\mathbf{x}}\Psi_J(\mathbf{X}_I)$.

3.3.3 Solution procedures

In preprocessing, all shape functions and gradient approximation terms are computed and stored. We employ the explicit second-order version of the Newmark-Beta method to integrate the semi-discrete momentum equation (3.22). The Riemann solution enriched pressure gradient in $\mathbf{f}^{\text{int}}$ is calculated for each node at each time step using the technique presented in the last section.

For the Energy equation (3.3), forward time integration is performed with the Euler scheme and the equation is solved strongly at each node. Consistent with the momentum equation, the smoothed gradient, the Riemann solution enriched pressure and velocity are used to calculate the total internal energy density,

$$E^{(n+1)} = E^{(n)} + \Delta t\left[\bar{\nabla}^{\mathbf{x}} \cdot (-P^* \mathbf{v}^*)\right]^{(n)}, \tag{3.33}$$

where superscript n denotes the n-th time step, and $\bar{\nabla}^{\mathbf{x}} \cdot (-P^* \mathbf{v}^*)$ is computed by the following smoothed gradient

$$\bar{\nabla}^{\mathbf{x}} (-P^* \mathbf{v}^*)\Big|_{\mathbf{x}(\mathbf{X}_I, t)} = -2 \sum_{J \in Z_I} \bar{\nabla}^{\mathbf{x}} \Psi_J (\mathbf{X}_I) P_{IJ}^* \mathbf{v}_{IJ}^* . \tag{3.34}$$

where P_{IJ}^* and $\mathbf{v}_{IJ}^*$ is the Riemann solution enriched pressure and velocity associated with the IJ pair for node I.

The internal energy density is then updated as

$$e^{(n+1)} = E^{(n+1)} - \frac{1}{2}\left(\mathbf{v} \cdot \mathbf{v}\right)^{(n+1)}. \tag{3.35}$$

The conservation of mass in the Lagrangian form leads to the following simple update of density,

$$\rho^{(n+1)} = \frac{\rho^{(0)}}{\det(\bar{\mathbf{F}}^{(n+1)})}. \tag{3.36}$$

With the updated internal energy and density at hand, the pressure is then computed at each node by the EOS (assuming idea gas),

$$P^{(n+1)} = \left(\gamma - 1\right)\rho^{(n+1)}e^{(n+1)}. \tag{3.37}$$

The formulation developed above is a combination of using the Riemann problem solution to evaluate the Godunov flux by considering the shock physics and the SNNI gradient smoothing technique and is termed 'Riemann-SNNI' in this work.

3.4 NUMERICAL EXAMPLES

For all the numerical examples, the support size for the RK approximation is set to be 1.75 times the nodal spacing, and linear basis with a cubic spline kernel function is employed.

3.4.1 One-dimensional Sod shock tube problem

We consider the one-dimensional Sod shock tube problem [53]on the domain [0, 1] consisting of two materials with initial states as $\rho_L = 1$, $v_L = 0$, $P_L = 1$ and $\rho_R = 0.125$, $v_R = 0$, $P_R = 0.1$, separated by a contact discontinuity at $x = 0.5$. The adiabatic index for the ideal gas is $\gamma = 1.4$. After the interaction between the two sides, a shock wave propagates towards the right and a rarefaction wave moves left. Three uniform discretizations are employed (250 nodes, 500 nodes and 1000 nodes) to perform the simulation, and the results are compared with the exact solutions in Figure 3.4 at time 0.2. As shown in the figure, the numerical results obtained by Riemann-SNNI agree well with the exact solution in terms of the solution magnitude and shock speed, and the solution converges with mesh

refinement. For all three simulations, the sharp discontinuity is captured by the scheme. The so-called ‘wall-heating’ phenomenon [54] is observed in internal energy, which is expected to occur in Lagrangian hydrodynamic formulations [54].

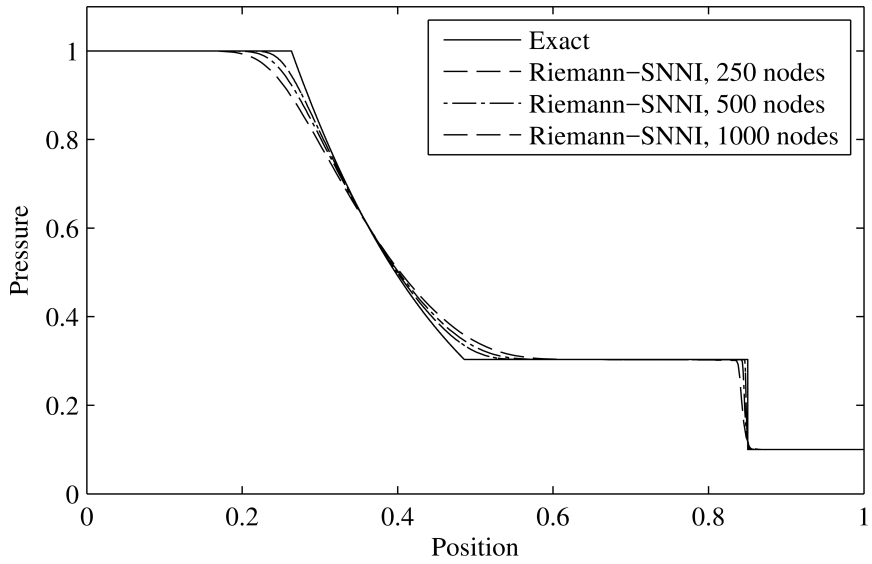

(a)

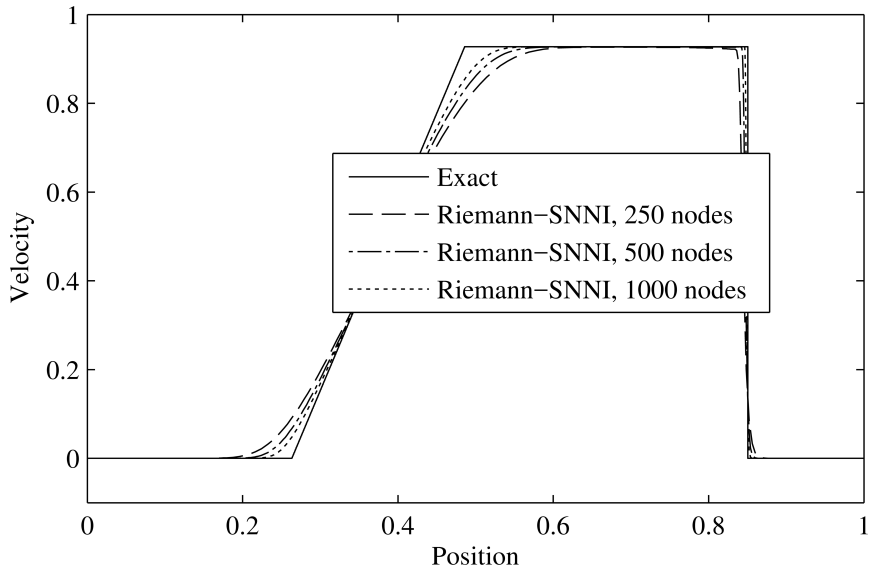

(b)

Figure 3.4. The results of one-dimensional Sod shock tube problem at time $t = 0.2$. (a) pressure; (b) velocity; (c) density; (d) internal energy.

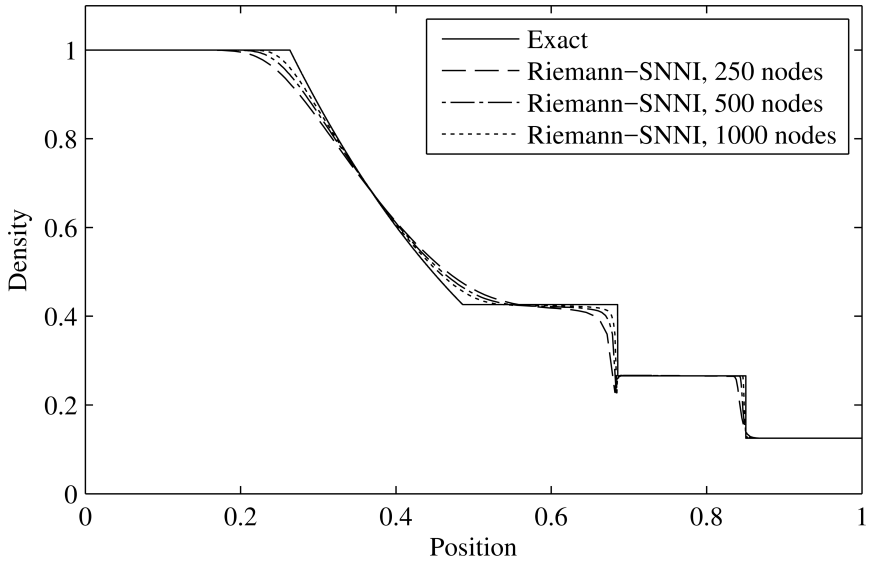

(c)

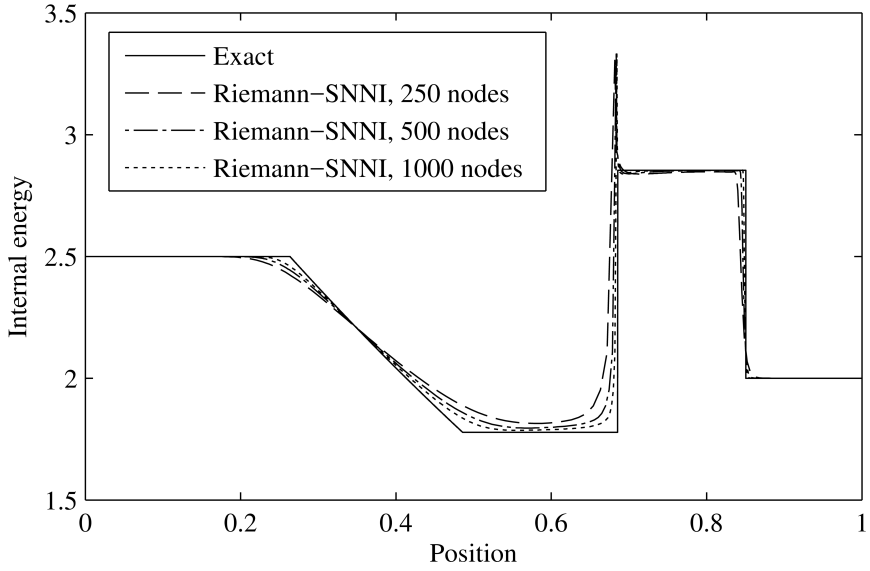

(d)

Figure 3.4. The results of one-dimensional Sod shock tube problem at time $t = 0.2$. (a) pressure; (b) velocity; (c) density; (d) internal energy. (Continued)

3.4.2 One-dimensional Noh implosion problem

For the one-dimensional Noh implosion problem [54], the problem states that a cold gas (with zero internal energy) impacts the wall from the right and generates a shock wave

moving toward the right. The initial velocity is chosen as $v^{(0)} = -1.0$ and initial pressure is chosen as zero. For numerical purposes the initial pressure is set to 10^{-6}. The adiabatic index and density are set to $\gamma = 5/3$ and $\rho^{(0)} = 1.0$ respectively. It is a strong shock problem and tests whether a method is capable to correctly transform the kinetic energy into internal energy. The problem domain is chosen as [0, 0.5] and is discretized by three uniform node distributions: 100 nodes, 200 nodes and 400 nodes.

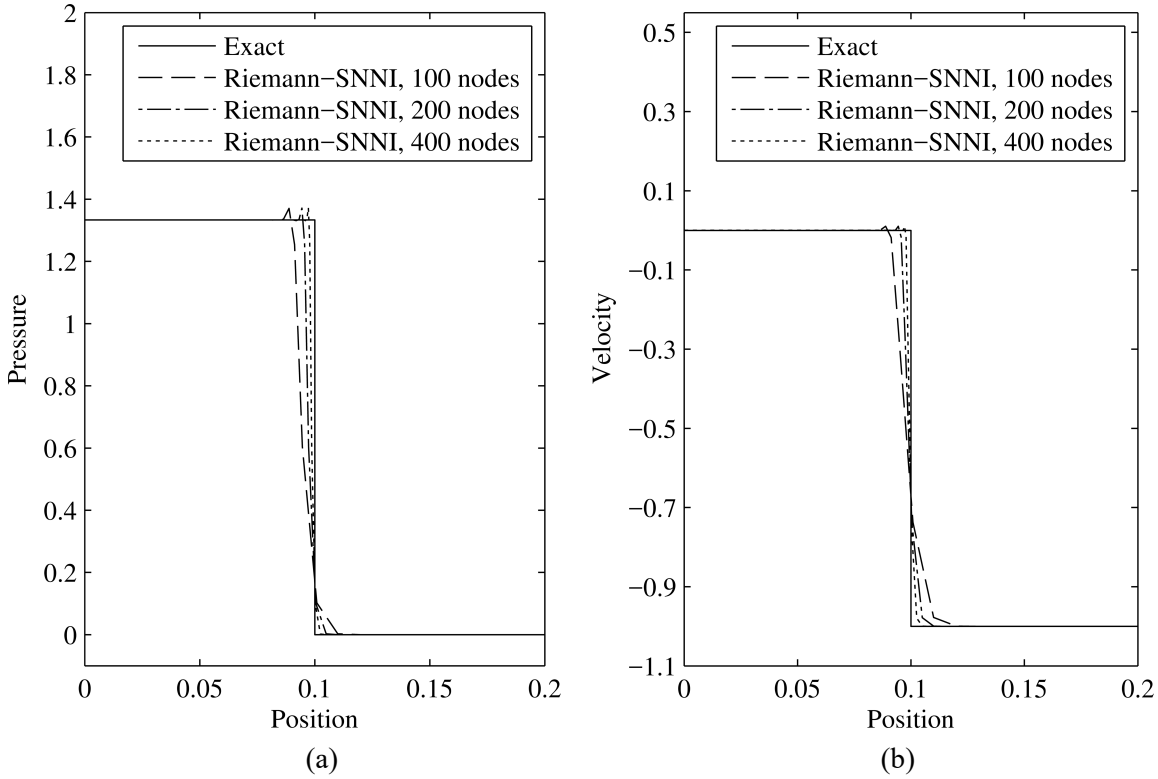

Figure 3.5. The results of one-dimensional Noh implosion problem at time $t = 0.125$: (a) pressure; (b) velocity;(c) density; (d) internal energy.

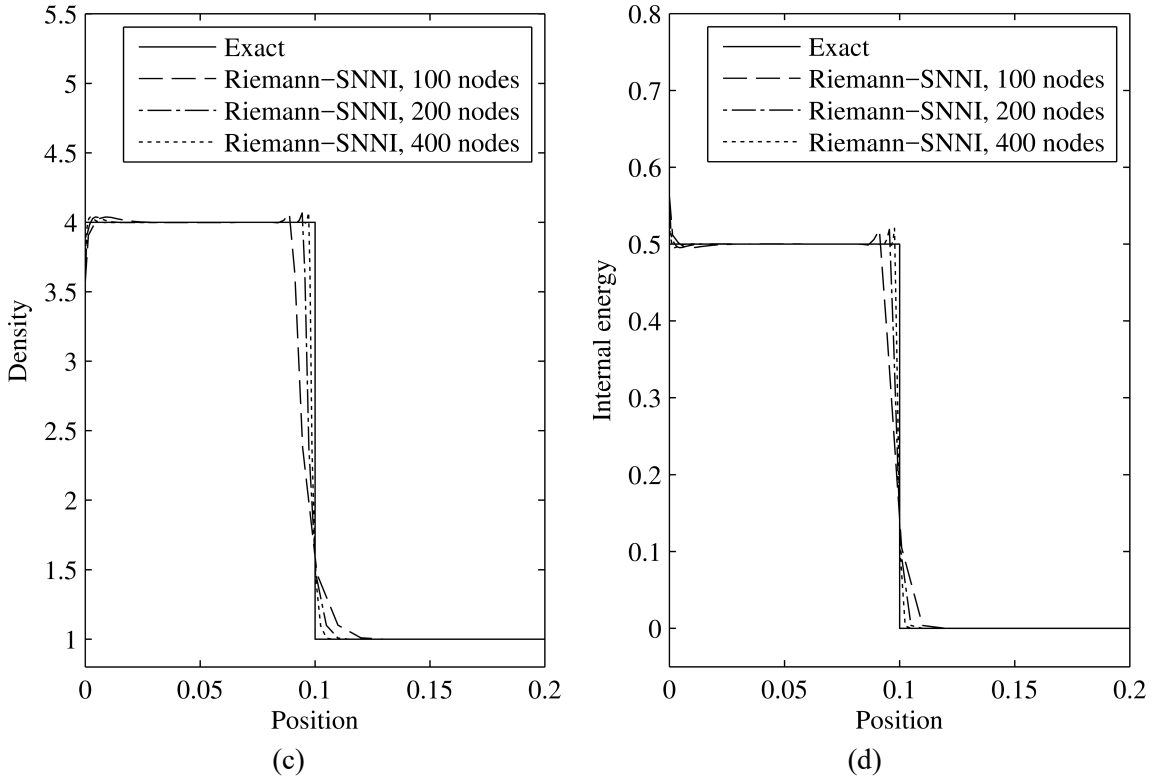

Figure 3.5. The results of one-dimensional Noh implosion problem at time t = 0.125: (a) pressure; (b) velocity;(c) density; (d) internal energy. (Continued)

Based on the results in Figure 3.5, we can see that the solution magnitude and shock wave speed obtained by Riemann-SNNI matches well with the exact solution [54] and the sharp shock front is captured. With mesh refinement, the solution converges as shown in the figure. This example demonstrates that Riemann-SNNI can capture strong shock waves and correctly transform kinetic energy into internal energy.

3.4.3 The Sedov blast wave problem

Two-dimensional Sedov blast wave problem [55] is computed on a square domain with edge length L = 1.2. Here, a sudden release of the energy at the origin generates an expanding shock wave. The initial condition of the problem consists of zero velocity field

and the Dirac delta distribution of the internal energy at the origin. In order to approximate the Dirac delta function, the four nodes nearest to the origin are assigned non-zero energy with a bilinear distribution which attains the maximum at the origin and vanishes between the second and third row of nodes, and the second and third column of nodes. The value of the bilinear function at the origin is set such that the total energy is 0.25. For numerical purposes, the initial pressures for the rest nodes are set to 10^{-6}. The adiabatic index and density are set to $\gamma = 1.4$ and $\rho^{(0)} = 1.0$, respectively. This problem tests whether a method is capable to correctly transform internal energy into kinetic energy. The direction of energy transformation is opposite to the previous Noh implosion problem.

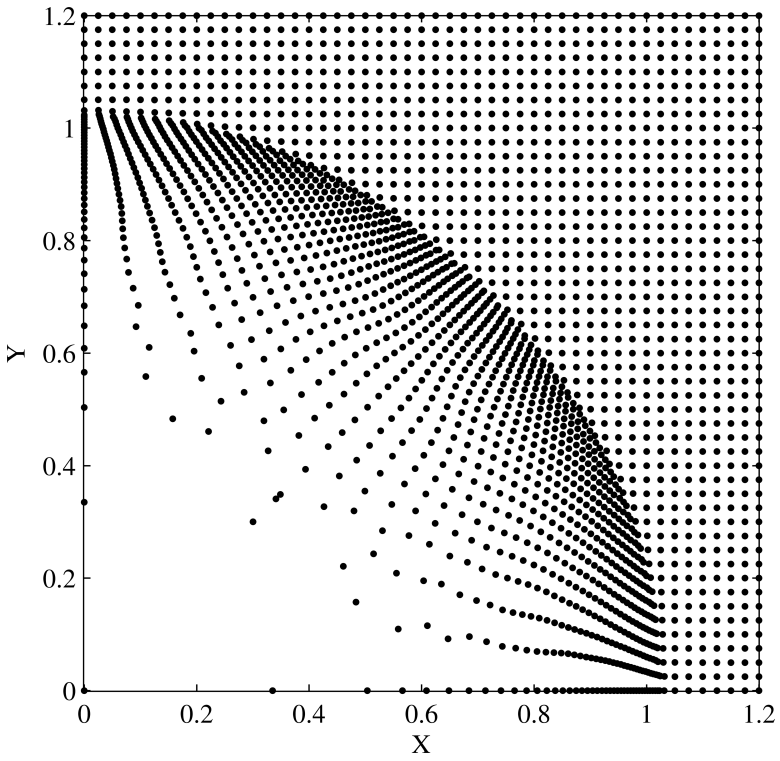

(a)

Figure 3.6. The result of two-dimensional Sedov problem at time $t = 1.0$. (a) the deformed node distribution;(b) the scatter plot of density v.s. radial distance in different directions.

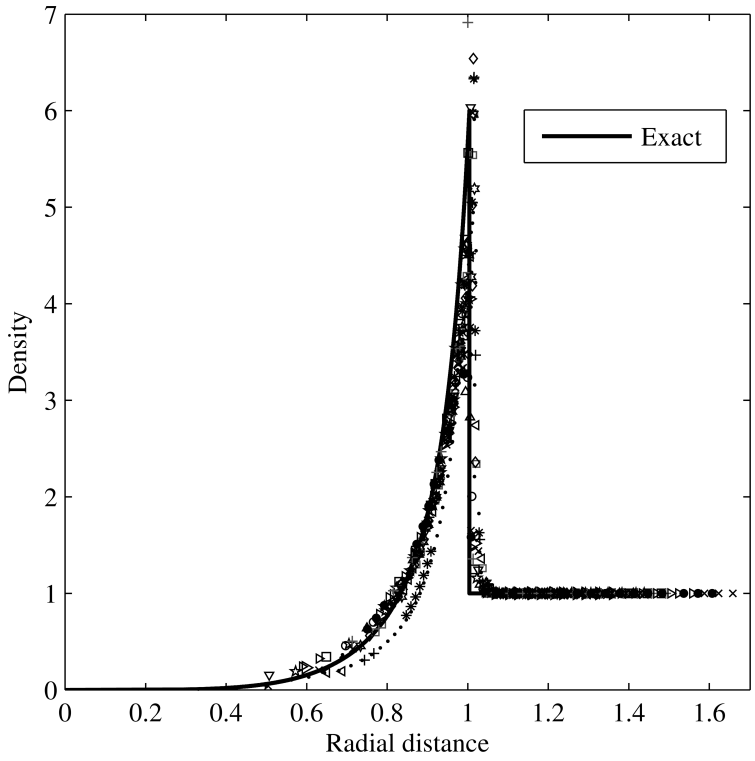

(b)

Figure 3.6. The result of two-dimensional Sedov problem at time $t = 1.0$. (a) the deformed node distribution;(b) the scatter plot of density v.s. radial distance in different directions. (Continued)

Since the problem is symmetric, the top right quarter of the domain is modeled with proper symmetry conditions prescribed on the boundaries. On the right edge and top edge, the pressure is equal to the initial pressure 10^{-6}. A uniform node distribution 48 × 48 is used to perform this simulation. The deformed nodal position and the density distribution obtained by Riemann-SNNI at time $t = 1.0$ are given in Figure 3.6 (a) and (b) respectively. The numerical density result is compared with exact solution in Figure 3.6 (b). The results are consistent with exact solution in terms of the shock speed and the density magnitude. On the other hand, the density distributions at time 1.0 for every 2° between 0° and 45° are plotted (the results at different angles are marked with different markers) and the result

shows good radial symmetry even though the problem is solved in Cartesian coordinates and discretized with nodes aligned with the Cartesian axes.

3.4.4 The Dukowicz problem

The Dukowicz problem is a two-dimensional shock refraction problem designed by Dukowicz and Meltz [56]. Here we use this problem to test whether Riemann-SNNI is capable to deal with multimaterial shock interaction in a multidimensional setting. The computational domain consists of two adjacent regions with equal pressures, but differing densities. They are separated by an interface aligned at 30° to the horizontal direction as shown in Figure 3.7. The initial conditions of the two regions are $\rho_L = 1,\ v_L = 0, P_L = 1$ and $\rho_R = 1.5,\ v_R = 0, P_R = 1$, respectively. The upper and lower boundaries are fixed in the normal directions and the left boundary is a piston, which moves from left to right with a constant speed 1.48. A uniform node distribution 110 × 30 is employed. The simulation is run to a time of 1.25, just before the simulation breaks down due to large distortions, which is expected for a Lagrangian formulation. The exact solution in terms of shock reflection and transmission angles and density distribution is given in Figure 3.8. The deformed node distribution is given in Figure 3.9 (a). Figure 3.9 (b) shows the density contour plot obtained by Riemann-SNNI which is consistent with the exact solution. On the other hand, in the same figure, it also shows the interfaces along with the incident and the transmitted shock waves clearly and they match well with the theoretic interfaces marked by the black straight solid lines. The reflective shock does not show up clearly in the figure, which is expected since the difference in density across it is small. This problem demonstrates Riemann-SNNI can naturally handle multimaterial shock interaction in the multidimensional case.

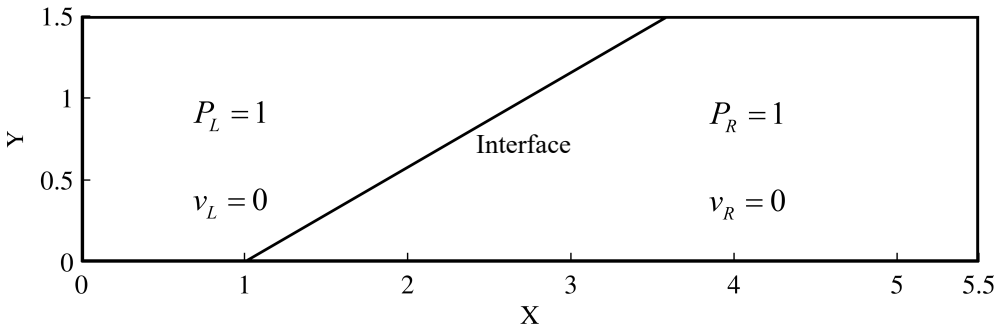

Figure 3.7. The initial conditions of the Dukowicz problem.

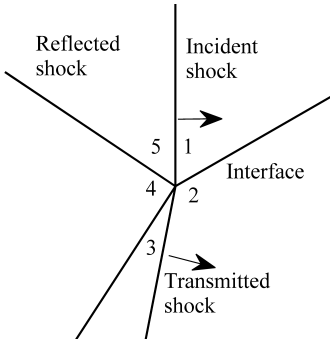

Region	1	2	3	4	5
Angle	60.00	131.02	21.90	90.96	56.12
Density	1.00	1.50	4.29	2.93	2.67

Figure 3.8. The exact solution for the Dukowicz problem.

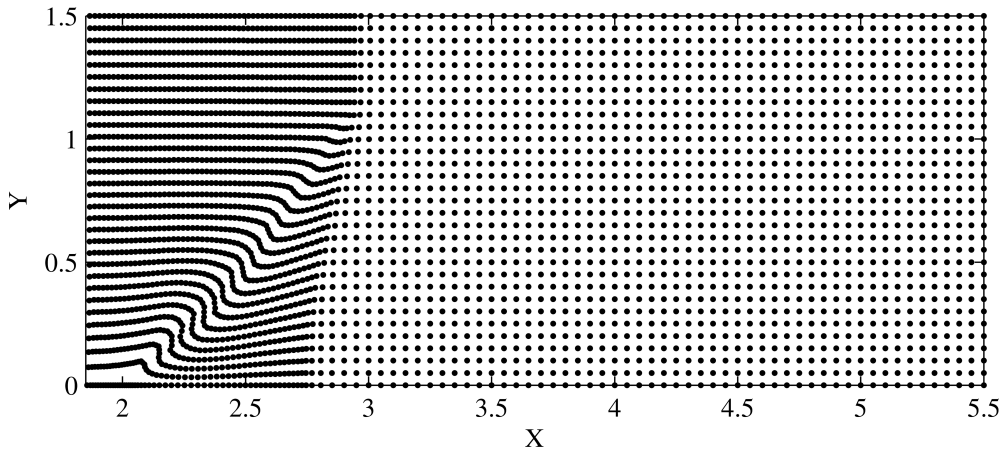

(a)

Figure 3.9. The result of Dukowicz problem by using Riemann-SNNI at time t =1.25. (a) the deformed node distribution; (b) the density contour plot.

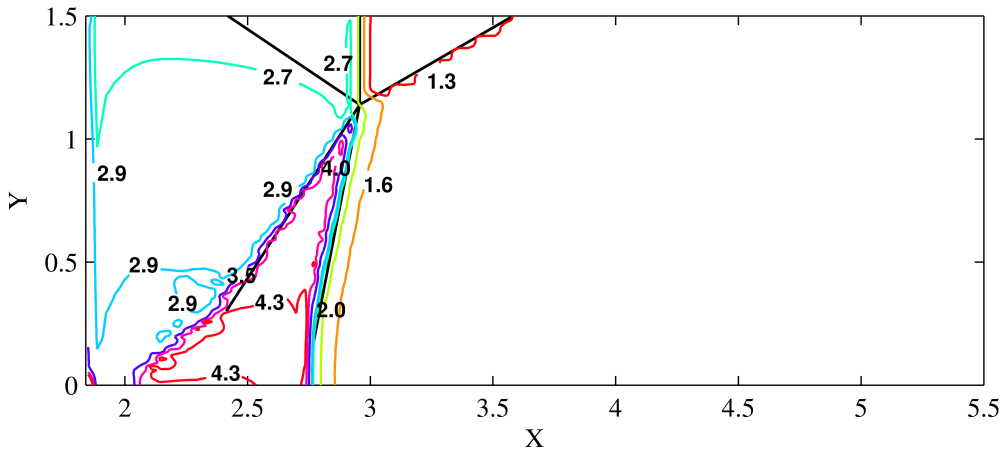

(b)

Figure 3.9. The result of Dukowicz problem by using Riemann-SNNI at time t =1.25. (a) the deformed node distribution; (b) the density contour plot. (Continued)

3.5 Conclusion

In this chapter we introduced a Lagrangian RKPM meshfree formulation with a node-based SNNI Godunov flux computation for modeling shock hydrodynamics in compressible flows. In comparison with the former work Riemann-SCNI in [35, 34], the proposed Riemann-SNNI eliminates the requirement of the conforming gradient smoothing cells by defining a node-based Riemann problem with pressure smoothed by non-conforming cells. Compared with GSPH, Riemann-SNNI inherits the advantages of RKPM over SPH and assures consistency and accuracy. In this framework only the orientation connecting node pairs is updated to form the Riemann problem in contrast to other Lagrangian methods (for example FVPM) where all the geometry information of cells is updated at each time step. This allows the shock physics to be embedded into the solution in a truly meshfree (node-based) setting. A set of numerical examples are given to demonstrate how the proposed method is capable of capturing the strong shock waves with sharp fronts as well as shock interactions.

This formulation works well for problems without material separation as shown in all the benchmark problems. However, it involves an extra contour integral term (the fourth term in equation (3.18)) which requires the definition of a physical boundary even at free surfaces, which could be difficult for problems with fragmentations. This limitation provides the motivation to further improve the formulation, which is to be discussed in next chapter.

ACKNOWLEDGEMENTS

This Chapter 3 is currently being prepared for submission for publication of the material. J.S. Chen, G. Zhou, M. Hillman, 'A Lagrangian Reproducing Kernel Particle Method for Shock Hydrodynamics'. The dissertation author was the primary investigator of this material.

Chapter 4

Meshfree Shock Hydrodynamic Formulation II: A Godunov-type Shock Capturing Algorithm in Galerkin Meshfree Methods for Solid and Fluid Dynamics

4.1 INTRODUCTION

A new formulation is proposed in this chapter to introduce the Godunov scheme into Galerkin meshfree methods to address shock physics. Compared with the formulation in Chapter 3, this formulation does not require conforming smoothing cells and utilizes the regular weak form (no extra contour integral term), and therefore is capable to model shock-induced fragmentations. The formulation is applicable to both solid and fluid dynamics. The performance of this method is examed by solving a set of benchmark problems, where the computational results are attained with good quality. As a general framework, it can be applied to other Galerkin meshfree and Galerkin mesh-based methods.

This chapter is organized as follows. In section 2, we provide the details of Galerkin approximation of the conservation laws. In section 3, both the Lagrangian and semi-Lagrangian discrete formulations are presented. The flow solver and the time integration procedure are discussed in section 4 and 5 respectively. The numerical results are presented in section 6 to demonstrate the effectiveness of this method, and followed by conclusions in section 7.

4.2 GALERKIN APPROXIMATION

The same as in the formulation in Chapter 3, we choose the updated Lagrangian form of the weak statement of the problem, which is more natural in the treatment of shocks via the Reimman problem. The weak form for conservation of linear momentum equation (3.2) with reference to the current configuration is: find $\mathbf{u} \in H_g^1$, such that $\forall \mathbf{w} \in H_0^1$:

$$\int_{\Omega_t} \rho \mathbf{w} \cdot \frac{\mathrm{d}^2 \mathbf{u}}{\mathrm{d}t^2} \mathrm{d}\Omega + \int_{\Omega_t} \nabla^{\mathrm{x}} \mathbf{w} : \boldsymbol{\sigma} \, \mathrm{d}\Omega - \int_{\Gamma_t^h} \mathbf{w} \cdot \mathbf{h} \mathrm{d}\Gamma = 0, \tag{4.1}$$

where Γ_t^h denotes the natural boundary, and $\mathbf{h}$ is the traction vector on Γ_t^h. Let the Cauchy stress tensor be decomposed into deviatoric and volumetric parts,

$$\boldsymbol{\sigma} = \boldsymbol{\sigma}^{\mathrm{d}} + \boldsymbol{\sigma}^{\mathrm{v}}, \tag{4.2}$$

where $\boldsymbol{\sigma}^{\mathrm{v}} = -P\mathbf{I}$; the identity tensor and P is the hydrostatic pressure. Using (4.2), equation (4.1) is then expressed as

$$\int_{\Omega_t} \rho \mathbf{w} \cdot \frac{\mathrm{d}^2 \mathbf{u}}{\mathrm{d}t^2} \mathrm{d}\Omega + \int_{\Omega_t} \nabla^{\mathrm{x}} \mathbf{w} : \boldsymbol{\sigma}^{\mathrm{d}} \, \mathrm{d}\Omega + \int_{\Omega_t} \nabla^{\mathrm{x}} \mathbf{w} : \boldsymbol{\sigma}^{\mathrm{v}} \, \mathrm{d}\Omega - \int_{\Gamma_t^h} \mathbf{w} \cdot \mathbf{h} \mathrm{d}\Gamma = 0. \tag{4.3}$$

Let $\mathbf{u}^h$ and $\mathbf{w}^h$ be the Lagrangian reproducing kernel (RK) approximation (details are given in section 3) of $\mathbf{u}$ and $\mathbf{w}$, the Galerkin method for (4.3) is to find $\mathbf{u}^h \in S^h$, such that $\forall \mathbf{w}^h \in V^h$:

$$\int_{\Omega_t} \rho \mathbf{w}^h \cdot \frac{\mathrm{d}^2 \mathbf{u}^h}{\mathrm{d}t^2} \mathrm{d}\Omega + \int_{\Omega_t} \nabla^{\mathrm{x}} \mathbf{w}^h : \boldsymbol{\sigma}^{\mathrm{d}}(\mathbf{u}^h) \mathrm{d}\Omega + \int_{\Omega_t} \nabla^{\mathrm{x}} \mathbf{w}^h : \boldsymbol{\sigma}^{\mathrm{v}}(\mathbf{u}^h) \mathrm{d}\Omega - \int_{\Gamma_t^h} \mathbf{w}^h \cdot \mathbf{h} \mathrm{d}\Gamma = 0, \tag{4.4}$$

with $S^h \subset H_g^1$ and $V^h \subset H_0^1$. Note that kinematically admissible RK approximations can be constructed by e.g., the transformation method [36], or boundary singular kernel method [48]. In this work we employed the latter. The energy equation (3.3) and conservation of mass equation (3.1) are not discretized, but instead enforced strongly at each node.

The second and third terms in equation (4.4) contribute to the deviatoric and volumetric internal force terms, and are denoted by $\boldsymbol{f}^{\mathrm{d}}$ and $\boldsymbol{f}^{\mathrm{v}}$ respectively. By introducing $\mathbf{w}^h = \sum_{I=1}^{NP} \Psi_I \mathbf{c}_I$ where Ψ_I is the RK shape function and $\mathbf{c}_I$ is arbitrary coefficient, their components associated with node I in the i-th direction are:

$$
\begin{aligned}
f_{Ii}^{\mathrm{d}} &= \int_{\Omega_t} \Psi_{I,j} \sigma_{ij}^{\mathrm{d}} d\Omega, \\
f_{Ii}^{\mathrm{v}} &= \int_{\Omega_t} \Psi_{I,j} \sigma_{ij}^{\mathrm{v}} d\Omega.
\end{aligned}
\tag{4.5}
$$

To introduce shock physics into (4.4), a Riemann solution enriched flux gradient was introduced in Riemann-SCNI [34, 35]. There, Rankine-Hugoniot jump condition and entropy condition was met by solving the Riemann problem on Voronoi cell interfaces, and gradient smoothing via contour integral is performed to evaluate the Riemann problem solution enriched smoothed pressure gradient. However, for applications such as shock-induced fragmentation problems where semi-Lagrangian meshfree methods must be employed, continually reconstructing Voronoi cells is extremely cumbersome and computationally expensive. To avoid this difficulty, a general framework of node-based flux gradient evaluation is proposed which is applicable to direct gradients and smoothed gradients using both conforming and nonconforming cells, and is well-suited for Lagrangian and semi-Lagrangian meshfree simulations.

First, we rewrite equation (4.5) as

$$
\begin{aligned}
f_{Ii}^{\mathrm{v}} &= \int_{\Omega_t} \Psi_{I,j} \sigma_{ij}^{\mathrm{v}} d\Omega \\
&= \int_{\Omega_t} \left(\sum_{J=1}^{NP} \Psi_J \right) \Psi_{I,j} \sigma_{ij}^{\mathrm{v}} d\Omega \\
&= \int_{\Omega_t} \left(\left(\sum_{J=1}^{NP} \Psi_J \right) \Psi_{I,j} - \Psi_I \left(\sum_{J=1}^{NP} \Psi_{J,j} \right) \right) \sigma_{ij}^{\mathrm{v}} d\Omega \\
&= \sum_{J=1}^{NP} \int_{\Omega_t} \left(\Psi_J \Psi_{I,j} - \Psi_I \Psi_{J,j} \right) \sigma_{ij}^{\mathrm{v}} d\Omega.
\end{aligned}
\tag{4.6}
$$

In the above derivation, the 0-*th* order completeness of RK shape functions as been employed:

$$
\sum_{J=1}^{NP} \Psi_J = 1, \qquad \sum_{J=1}^{NP} \Psi_{J,j} = 0. \tag{4.7}
$$

We now make an assumption that σ_{ij}^{ν} is constant in the intersection of the supports of nodes *I* and *J*, denoted as $\sigma_{ij}^{\nu-IJ}$, and equation (4.6) reduces to

$$\begin{aligned} f_{Ii}^{\nu} &= \sum_{J=1}^{NP} \int_{\Omega_t} \left(\Psi_J \Psi_{I,j} - \Psi_I \Psi_{J,j} \right) \sigma_{ij}^{\nu} d\Omega \\ &= \sum_{J=1}^{NP} \int_{\Omega_t} \left(\Psi_J \Psi_{I,j} - \Psi_I \Psi_{J,j} \right) d\Omega \, \sigma_{ij}^{\nu-IJ} \\ &= \sum_{J=1}^{NP} \beta_j^{IJ} \, \sigma_{ij}^{\nu-IJ}, \end{aligned} \tag{4.8}$$

with

$$\beta_j^{IJ} = \int_{\Omega_x} \left(\Psi_J \Psi_{I,j} - \Psi_I \Psi_{J,j} \right) d\Omega. \tag{4.9}$$

Similar procedures can be found in finite volume method where β_j^{IJ} is obtained from a cell geometry [57], and therefore β_j^{IJ} can be interpreted as equivalent geometric coefficients corresponding to the normal direction multiplied by the surface area of a virtual interface between node *I* and *J* as shown in Figure 4.1.

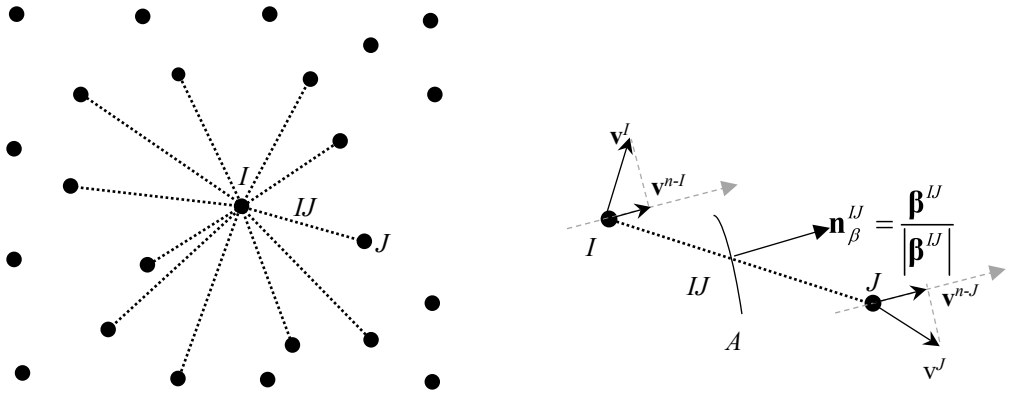

Figure 4.1 The local Riemann problem of nodal pair *I-J* .

Note that in strong shock problems, the pressure is the dominant component of Cauchy stress tensor. The Godunov scheme is then employed to introduce shock physics into the volumetric internal force term $\boldsymbol{f}_I^v$ in equation (4.8) as follows.

In order to capture the shock discontinuity, Riemann problem is solved between node *I* and *J* (denoted by *IJ*) based on $\boldsymbol{\beta}^{IJ}$ (see Figure 4.1) and then $\sigma_{ij}^{\mathrm{v}-IJ}$ in equation (4.8) is calculated using the Riemann problem solution for the pressure P^{IJ*} ('*' denotes the Riemann problem solution). That is,

$$f_{Ii}^{\mathrm{v}*} = \sum_{J=1}^{NP} \beta_j^{IJ}\, \sigma_{ij}^{\mathrm{v}-IJ*}, \tag{4.10}$$

where

$$\sigma_{ij}^{\mathrm{v}-IJ*} = -P^{IJ*}\delta_{ij}. \tag{4.11}$$

Consistent with Godunov scheme, the energy equation (3.3) now becomes, at each node

$$\rho^I \frac{\mathrm{d}E^I}{\mathrm{d}t} = -\nabla^{\mathbf{x}} \cdot \left(\mathbf{v}^{IJ*} \cdot \boldsymbol{\sigma}^{\mathrm{v}-IJ*}\right), \tag{4.12}$$

where $\mathbf{v}^{IJ*}$ is the velocity solution of the Riemann problem and $\nabla^{\mathbf{x}} \cdot \left(\mathbf{v}^{IJ*} \cdot \boldsymbol{\sigma}^{\mathrm{v}-IJ*}\right)$ is given by the trace of the following gradient

$$\nabla^{\mathbf{x}} \left(\mathbf{v}^{IJ*} \cdot \boldsymbol{\sigma}^{\mathrm{v}-IJ*}\right) = \sum_{J=1}^{NP} \boldsymbol{\beta}^{IJ}\, P^{IJ*} \mathbf{v}^{\mathbf{n}-IJ*}, \tag{4.13}$$

On the other hand, it is easy to show from equation (4.9) that

$$\beta_j^{IJ} = -\beta_j^{JI}. \tag{4.14}$$

And with the Riemann problem solved between *I*-*J* pair, during the evaluations of volumetric internal force and energy rate change by equation (4.10) and equation (4.12) respectively, the pressure flux and energy flux for *I*-*J* pair cancel out with that of *J*-*I* pair

and thus the flux is conserved. Namely, this anti-symmetric property of $\boldsymbol{\beta}^{IJ}$ ensures the conservation of linear momentum and energy for the volumetric contribution to the weak form [24].

In this work, the Dukowicz solver [51] is adopted for its robustness and efficiency (see Chapter 3, equation $(3.24)-(3.26)$).

Note that this framework can be applied to both solids and fluids. Without loss of generality, we consider inviscid compressible flow for fluids and therefore $\boldsymbol{f}_I^{\mathrm{d}}$ vanishes. A pressure-density relationship given by equation of state (EOS) for the ideal gas is utilized:

$$P = (\gamma - 1)\rho e, \tag{4.15}$$

where γ is the adiabatic index (assumed to be constant for a given gas).

4.3 LAGRAGIAN AND SEMI-LAGRANGIAN DISCRETE FORMULATIONS

4.3.1 Lagrangian RKPM with conforming strain smoothing

For problems where the deformation gradient is non-singular and also well-conditioned (e.g. in the absence of extreme material distortion or fragmentation), we consider the Lagrangian RKPM formulation [36]. All the approximations are computed in the undeformed configuration, stored and mapped to the current configuration, and thus this formulation is efficient.

4.3.1.1 Stabilized conforming nodal integration

In Lagrangian framework, the reproducing kernel approximation $\mathbf{u}^h(\mathbf{X},t)$ of a function $\mathbf{u}(\mathbf{X},t)$ using a set of *NP* nodes in the underformed configuration is constructed as

$$\mathbf{u}^h(\mathbf{X},t)=\sum_{I=1}^{NP}\Psi_I^{\mathbf{X}}(\mathbf{X})\mathbf{d}_I(t), \tag{4.16}$$

where $\Psi_I^{\mathbf{X}}(\mathbf{X})$ and $\mathbf{d}_I(t)$ are the Lagrangian RK shape function and the generalized coordinate of the *I-th* node, respectively. The shape function $\Psi_I^{\mathbf{X}}(\mathbf{X})$ derived in last chapter is given by

$$\Psi_I^{\mathbf{X}}(\mathbf{X})=\mathbf{H}^T(\mathbf{0})\mathbf{M}^{-1}(\mathbf{X})\mathbf{H}(\mathbf{X}-\mathbf{X}_I)\phi_a(\mathbf{X}-\mathbf{X}_I). \tag{4.17}$$

In this chapter, $\Psi_I^{\mathbf{X}}$ and $\Psi_I^{\mathbf{x}}$ are used to distinguish the shape functions associated of node *I* defined in the undeformed and current configurations.

Under Lagrangian framework, we consider stabilized conforming nodal integration (SCNI) [37], which utilizes the conforming gradient smoothing cells constructed via Voronoi diagrams, as shown in Figure 1(a). The key idea of SCNI is to replace the direct nodal gradient by a smoothed gradient $\bar{\nabla}$ ('$-$' denotes a smoothed term). This avoids instability in the solution due to employing direct gradients evaluated at nodes, which severely under-estimates the energy of short-wavelength modes. With the employment of conforming cells, SCNI satisfies the linear integration constraint and can achieve optimal convergence for approximations with linear completeness [37].

In SCNI under Lagrangian framework, the gradients are smoothed over each nodal representative domain Ω_L by

$$\bar{\nabla}^{\mathrm{x}}\Psi_I^{\mathrm{x}}(\mathbf{X}_L) = \frac{1}{W_L^{\mathrm{x}}}\int_{\Omega_L^{\mathrm{x}}} \nabla^{\mathrm{x}}\Psi_I^{\mathrm{x}}(\mathbf{X})\mathrm{d}\Omega = \frac{1}{W_L^{\mathrm{x}}}\int_{\Gamma_L^{\mathrm{x}}} \Psi_I^{\mathrm{x}}(\mathbf{X})\mathbf{N}(\mathbf{X})\mathrm{d}\Gamma, \qquad (4.18)$$

where $\Psi_I^{\mathrm{x}}(\mathbf{X})$ is the RKPM shape function computed in the undeformed configuration, Γ_L^{x} is the boundary of the conforming nodal cell Ω_L^{x} in the undeformed configuration associated with node L, $\mathbf{N}$ is the normal of that cell, and $W_L^{\mathrm{x}} = \int_{\Omega_L^{\mathrm{x}}} d\Omega$.

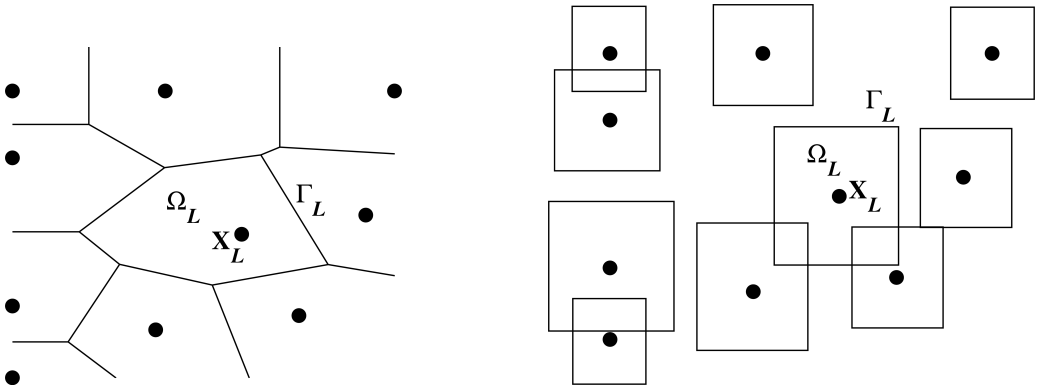

(a) (b)

Figure 4.2. (a) Conforming SCNI, and (b) non-conforming SNNI smoothing cells.

Note that in the Lagrangian RK approximation, if the reference configuration is chosen as current configuration, an inverse mapping is necessary to construct the approximation $\Psi_I^{\mathrm{x}}(\mathbf{X}) = \Psi_I^{\mathrm{x}}(\boldsymbol{\varphi}^{-1}(\mathbf{x},t))$. However, since all quantities are evaluated at fixed material points, the inverse mapping $\mathbf{X} = \boldsymbol{\varphi}^{-1}(\mathbf{x},t)$ does not have to be calculated. Spatial derivatives can be constructed implicitly rather than directly as follows. After $\bar{\nabla}^{\mathrm{x}}\Psi_I^{\mathrm{x}}(\mathbf{X}_L)$ is computed, $\bar{\nabla}^{\mathrm{x}}\Psi_I^{\mathrm{x}}(\mathbf{X}_L)$ can be obtained by the chain rule as needed for path-dependent materials,

$$\bar{\nabla}^{\mathrm{x}}\Psi_I^{\mathrm{X}}(\mathbf{X}_L)=\bar{\mathbf{F}}^{-\mathrm{T}}(\mathbf{X}_L)\bullet\bar{\nabla}^{\mathrm{X}}\Psi_I^{\mathrm{X}}(\mathbf{X}_L), \tag{4.19}$$

$$\bar{\mathbf{F}}(\mathbf{X}_L)=\sum_{I=1}^{NP}\bar{\nabla}^{\mathrm{X}}\Psi_I^{\mathrm{X}}(\mathbf{X}_L)\otimes\mathbf{x}_I, \tag{4.20}$$

where $\bar{\mathbf{F}}^{-\mathrm{T}}(\mathbf{X}_L)$ is the smoothed deformation gradient computed point-wise (see [37] for details).

With Lagrangian RK approximation and all the domain integral terms in Galerkin equation (4.4) integrated using SCNI, the following discrete equation is obtained

$$\begin{aligned}\mathbf{M}\mathbf{a}&=\mathbf{f}^{\mathrm{ext}}-\mathbf{f}^{\mathrm{int}*},\\ \mathbf{f}^{\mathrm{int}*}&=\mathbf{f}^{\mathrm{d}}+\mathbf{f}^{\mathrm{v}*},\end{aligned} \tag{4.21}$$

where $\mathbf{a}=\mathrm{d}\mathbf{v}/\mathrm{d}t$, and

$$\begin{aligned}\mathbf{M}_I&=\sum_{L=1}^{NP}\rho(\mathbf{x}_L)\mathbf{I}\Psi_I^{\mathrm{X}}(\mathbf{x}_L)V_L,\\ \mathbf{f}_I^{\mathrm{d}}&=\sum_{L=1}^{NP}\boldsymbol{\sigma}^{\mathrm{d}}(\mathbf{x}_L)\cdot\bar{\nabla}^{\mathrm{x}}\Psi_I^{\mathrm{X}}(\mathbf{x}_L)V_L,\\ \mathbf{f}_I^{\mathrm{v}*}&=-\sum_{J=1}^{NP}\bar{\boldsymbol{\beta}}^{IJ}P^{IJ*},\\ \mathbf{f}_I^{\mathrm{ext}}&=\sum_{L=1}^{NPh}\Psi_I^{\mathrm{X}}(\mathbf{x}_L)\mathbf{h}S_L,\end{aligned} \tag{4.22}$$

with

$$\bar{\boldsymbol{\beta}}^{IJ}=\sum_{L=1}^{NP}\left(\Psi_J^{\mathrm{X}}(\mathbf{x}_L)\bar{\nabla}^{\mathrm{x}}\Psi_I^{\mathrm{X}}(\mathbf{x}_L)-\Psi_I^{\mathrm{X}}(\mathbf{x}_L)\bar{\nabla}^{\mathrm{x}}\Psi_J^{\mathrm{X}}(\mathbf{x}_L)\right)V_L, \tag{4.23}$$

where V_I is the volume for node I in the current configuration, S_L is the L-th weight of the NPh integration points on the natural boundary in the current configuration. In the above discrete equations (4.22), mass lumping has been employed in conjunction with the partition of unity of the shape functions. Note that in equations (4.22), the variable

$g(\mathbf{x}_L) = g(\mathbf{x}(\mathbf{X}_L, t)) = g(\mathbf{X}_L)$ (g represents $\rho, \Psi_I^{\mathrm{X}}, \boldsymbol{\sigma}^{\mathrm{d}}, \bar{\nabla}^{\mathrm{x}} \Psi_I^{\mathrm{X}}$) since it is a Lagrangian formulation with a nodal integration scheme.

4.3.2 semi-Lagrangian RKPM with non-conforming strain smoothing for extreme deformation

For problems with severe material distortion where the deformation gradient can become ill-conditioned or singular, and a purely Lagrangian description can no longer suffice. Thus, we consider the semi-Lagrangian formulation to overcome this issue.

4.3.2.1 semi-Lagrangian reproducing kernel approximation

In the semi-Lagrangian RK formulation [43], the nodal point $\mathbf{x}_I$ associated with the shape function $\Psi_I^{\mathrm{x}}(\mathbf{x})$ which is defined in the current configuration follows the motion of material point, that is, $\mathbf{x}_I = \mathbf{x}(\mathbf{X}_I, t)$, whereas the kernel function can be defined independent of the material deformation as shown in Figure 4.3.

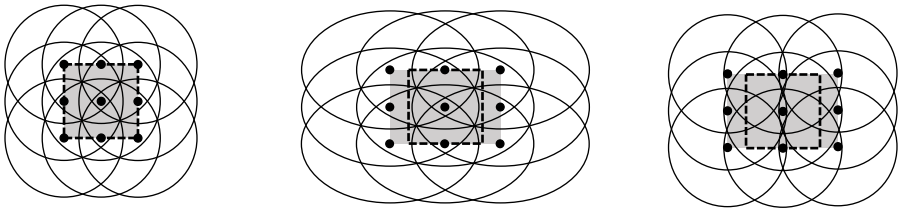

(a) (b) (c)

Figure 4.3. Comparison of Lagrangian and semi-Lagrangian reproducing kernel(RK) shape functions: (a) undeformed configuration, (b) Lagrangian RK in the deformed configuration, and (c) semi-Lagrangian RK in the deformed configuration.

The semi-Lagrangian RK shape function is constructed as

$$\Psi_I^{\mathbf{x}}(\mathbf{x}) = C(\mathbf{x}; \mathbf{x} - \mathbf{x}(\mathbf{X}_I, t))\phi_a(\mathbf{x} - \mathbf{x}(\mathbf{X}_I, t)). \tag{4.24}$$

Note that the kernel function which defines the locality and smoothness is not purely Lagrangian meaning that its support may covers different node set during the material motion. Similar to equation (3.10), the associated coefficients vector **b**(**x**) can be obtained by imposing the following reproducing conditions:

$$\sum_{I=1}^{NP} \Psi_I^{\mathbf{x}}(\mathbf{x}) x_{I1}^i x_{I2}^j x_{I3}^k = x_1^i x_2^j x_3^k, \quad i + j + k = 0, 1, \cdots, n. \tag{4.25}$$

Substituting **b**(**x**) into equation (4.24) yields the semi-Lagrangian RK shape function,

$$\Psi_I^{\mathbf{x}}(\mathbf{x}) = \mathbf{H}^T(\mathbf{0})\mathbf{M}^{-1}(\mathbf{x})\mathbf{H}(\mathbf{x} - \mathbf{x}(\mathbf{X}_I, t))\phi_a(\mathbf{x} - \mathbf{x}(\mathbf{X}_I, t)), \tag{4.26}$$

where

$$\mathbf{M}(\mathbf{x}) = \sum_{I=1}^{NP} \mathbf{H}(\mathbf{x} - \mathbf{x}(\mathbf{X}_I, t))\mathbf{H}^T(\mathbf{x} - \mathbf{x}(\mathbf{X}_I, t))\phi_a(\mathbf{x} - \mathbf{x}(\mathbf{X}_I, t)). \tag{4.27}$$

Note that different from the Lagrangian shape function, here the **x** coordinate in Ψ_I and **M** is a function of time. Consequently, if the primary variable in equation (4.4) is velocity v_i which is approximated by semi-Lagrangian RK shape functions:

$$v_i^h(\mathbf{x}, t) = \sum_{I=1}^{NP} \Psi_I^{\mathbf{x}}(\mathbf{x}) v_{Ii}(t), \tag{4.28}$$

then the corresponding acceleration **a** is given by

$$a_i = \frac{\mathrm{d}v_i^h(\mathbf{x}, t)}{\mathrm{d}t} = \sum_{I=1}^{NP} \left(\Psi_I^{\mathbf{x}}(\mathbf{x}) \frac{\mathrm{d}v_{Ii}(t)}{\mathrm{d}t} + \overset{*}{\Psi}_I^{\mathbf{x}}(\mathbf{x}) v_{Ii}(t) \right), \tag{4.29}$$

where $\overset{*}{\Psi}_I^{\mathbf{x}}(\mathbf{x})$ is the correction due to the time-dependent change of the semi-Lagrangian kernel $\mathrm{d}\phi_a(\mathbf{x} - \mathbf{x}_I)/\mathrm{d}t$

$$\begin{aligned}
&\overset{*}{\Psi}{}^{\mathbf{x}}_I(\mathbf{x}) = C(\mathbf{x};\mathbf{x}-\mathbf{x}(\mathbf{X}_I,t))\frac{\mathrm{d}}{\mathrm{d}t}\phi_a(\mathbf{x}-\mathbf{x}(\mathbf{X}_I,t)),\\
&\frac{\mathrm{d}}{\mathrm{d}t}\phi_a(\mathbf{x}-\mathbf{x}(\mathbf{X}_I,t)) = \frac{\mathrm{d}}{\mathrm{d}t}\phi_a\left(\frac{|\mathbf{x}-\mathbf{x}(\mathbf{X}_I,t)|}{a}\right) = \phi_a{}'\,\frac{\mathbf{q}\cdot(\mathbf{v}-\mathbf{v}_I)}{a},
\end{aligned} \tag{4.30}$$

where $\mathbf{q} = \left(\mathbf{x}-\mathbf{x}(\mathbf{X}_I,t)\right)/\left|\mathbf{x}-\mathbf{x}(\mathbf{X}_I,t)\right|$. Here the correction function C in the above equation is used to enforce the reproducing condition of the time derivative of the semi-Lagrangian kernel $\mathrm{d}\phi_a(\mathbf{x}-\mathbf{x}_I)/\mathrm{d}t$ and thus, the time rate change of C is not considered.

4.3.2.2 Stabilized non-conforming nodal integration

Under semi-Lagrangian framework, the SCNI becomes computationally demanding and impractical because the Voronoi cell reconstruction in the deformed configuration at each time step is required and thus time-consuming. In this case, we adopt the stabilized non-conforming nodal integration (SNNI) [4, 5] which utilizes the non-conforming gradient smoothing cells with simple geometry such as spheres or bricks, as shown in Figure 1(b). The simplified SNNI technique may not optimally converge due to the relaxation of the conforming condition, but this deficiency can be corrected by employing variationally consistent integration [49].

In SNNI under semi-Lagrangian framework, the smoothed gradients constructed directly in the current configuration [4, 5]:

$$\bar{\nabla}^{\mathbf{x}}\Psi^{\mathbf{x}}_I(\mathbf{x}_L) = \frac{1}{W^{\mathbf{x}}_L}\int_{\Omega^{\mathbf{x}}_L}\nabla^{\mathbf{x}}\Psi^{\mathbf{x}}_I(\mathbf{x})\mathrm{d}\Omega = \frac{1}{W^{\mathbf{x}}_L}\int_{\Gamma^{\mathbf{x}}_L}\Psi^{\mathbf{x}}_I(\mathbf{x})\mathbf{n}(\mathbf{x})\mathrm{d}\Gamma, \tag{4.31}$$

where $\Psi^{\mathbf{x}}_I(\mathbf{x})$ is the RKPM shape function constructed in the current configuration, $\Gamma^{\mathbf{x}}_L$ is the boundary of the non-conforming nodal cell associated with node L in the current

configuration $\Omega_L^{\mathbf{x}}$, $\mathbf{n}$ is the normal of that cell, and $W_L^{\mathbf{x}} = \int_{\Omega_L^{\mathbf{x}}} d\Omega$. The smoothing cells also remain centered around the nodes and translate with their movement without deformation.

Substituting equation (4.29) into equation (4.4) and integrating all the domain integral terms by using SNNI lead to the following discrete equation

$$\begin{aligned} &\mathbf{Ma} + \mathbf{Nv} = \mathbf{f}^{\text{ext}} - \mathbf{f}^{\text{int*}}, \\ &\mathbf{f}^{\text{int*}} = \mathbf{f}^{\text{d}} + \mathbf{f}^{\text{v*}}, \end{aligned} \tag{4.32}$$

where

$$\begin{aligned} \mathbf{M}_I &= \sum_{L=1}^{NP} \rho(\mathbf{x}_L)\mathbf{I}\Psi_I^{\mathbf{x}}(\mathbf{x}_L)V_L, \\ \mathbf{N}_{IJ} &= \sum_{L=1}^{NP} \rho(\mathbf{x}_L)\mathbf{I}\Psi_I^{\mathbf{x}}(\mathbf{x}_L)\overset{*}{\Psi}_J^{\mathbf{x}}(\mathbf{x}_L)V_L, \\ \mathbf{f}_I^{\text{d}} &= \sum_{L=1}^{NP} \boldsymbol{\sigma}^{\text{d}}(\mathbf{x}_L)\cdot\overline{\nabla}^{\mathbf{x}}\Psi_I^{\mathbf{x}}(\mathbf{x}_L)V_L, \\ \mathbf{f}_I^{\text{v*}} &= -\sum_{J=1}^{NP} \overline{\boldsymbol{\beta}}^{IJ} P^{IJ*}, \\ \mathbf{f}_I^{\text{ext}} &= \sum_{L=1}^{NPh} \Psi_I^{\mathbf{x}}(\mathbf{x}_L)\mathbf{h}S_L, \end{aligned} \tag{4.33}$$

with

$$\overline{\boldsymbol{\beta}}^{IJ} = \sum_{L=1}^{NP} \left(\Psi_J^{\mathbf{x}}(\mathbf{x}_L)\overline{\nabla}^{\mathbf{x}}\Psi_I^{\mathbf{x}}(\mathbf{x}_L) - \Psi_I^{\mathbf{x}}(\mathbf{x}_L)\overline{\nabla}^{\mathbf{x}}\Psi_J^{\mathbf{x}}(\mathbf{x}_L) \right) V_L, \tag{4.34}$$

where V_I is the volume for node I in the current configuration, S_L is the L-th weight of the NPh integration points on the natural boundary in the current configuration. The key differences between equation (4.33) and equation (4.22) are that the former one has the convective effect, $\mathbf{Nv}$ and its shape function is defined in the current configuration.

Note that if a nodal integration scheme is used to integrated equation (4.32)-(4.34) such as SNNI, the diagonal terms of $\mathbf{N}$ vanish, and the off-diagonal terms of $\mathbf{N}$ have

relatively negligible influence over (4.32) [5, 4]. Therefore, the convective effect, **Nv** in equation (4.32) is omitted for computational efficiency.

4.4 FLOW SOLVER

In order to compute $\boldsymbol{f}_I^{v^*}$ and energy evolution, defining and solving Riemann problems to obtain **v*** and P^* are discussed in this section.

With $\overline{\boldsymbol{\beta}}^{IJ}$ at hand, Riemann problem can be defined between node *I* and *J* which is denoted by *IJ*. As shown in Figure 4.1, it can be interpreted as that there is a virtual surface '*A*' between node *I* and *J* with the surface normal direction $\mathbf{n}_\beta^{IJ}$ given by normalizing $\overline{\boldsymbol{\beta}}^{IJ}$,

$$\mathbf{n}_\beta^{IJ} = \frac{\overline{\boldsymbol{\beta}}^{IJ}}{\left|\overline{\boldsymbol{\beta}}^{IJ}\right|}, \tag{4.35}$$

where $\left|\overline{\boldsymbol{\beta}}^{IJ}\right|$ is the length of vector $\overline{\boldsymbol{\beta}}^{IJ}$. Here, Riemann problem is considered one-dimensional and the velocity vector is projected along the $\mathbf{n}_\beta^{IJ}$ direction while pressure is scalar and there is no need to do so. For the *I*-*J* pair, the projected velocity of $\mathbf{v}^I$ and $\mathbf{v}^J$ are $\mathbf{v}^{n\text{-}I}$ and $\mathbf{v}^{n\text{-}J}$, respectively.

$$\begin{aligned} \mathbf{v}^{n-I} &= \mathbf{v}^I \cdot \mathbf{n}_\beta^{IJ}, \\ \mathbf{v}^{n-J} &= \mathbf{v}^J \cdot \mathbf{n}_\beta^{IJ}. \end{aligned} \tag{4.36}$$

Then the Riemann problem is defined as left state $\{ P^I, \mathbf{v}^{n\text{-}I}, \rho^I \}$ and right state $\{ P^J, \mathbf{v}^{n\text{-}J}, \rho^J \}$ and after using Riemann solver (here it is Dukowicz solver [51]) the solution is

obtained as $\{P^{IJ*}, \mathbf{v}^{n\text{-}IJ*}\}$. Then $\boldsymbol{f}_I^{v*}$ is evaluated by either equation (4.22) or equation (4.33).

Energy equation (4.12) is satisfied strongly and solved locally at each node using the forward Euler scheme,

$$E^{I(n+1)} = E^{I(n)} + \Delta t\left[\nabla^{\mathbf{x}} \cdot (-P^{IJ*}\mathbf{v}^{n-IJ*})\right]^{(n)}, \tag{4.37}$$

where superscript (n) denotes the n-th time step, and $\nabla^{\mathbf{x}} \cdot (-P^{IJ*}\mathbf{v}^{n-IJ*})$ is given by the trace of the following gradient

$$\nabla^{\mathbf{x}}(-P^{IJ*}\mathbf{v}^{n-IJ*})\Big|_{\mathbf{x}(\mathbf{X}_I,t)} = -\sum_{J=1}^{NP} \overline{\boldsymbol{\beta}}^{IJ} P^{IJ*}\mathbf{v}^{n-IJ*}. \tag{4.38}$$

Here, as shown in the above equation (4.38), the gradient for computing energy is also based on the Riemann solution enriched pressure and velocity, which is consistent with the computation of the volumetric internal force terms in equation (4.22) and (4.33). The internal energy is updated directly at each node by

$$e^{I(n+1)} = E^{I(n+1)} - \frac{1}{2}\left(\mathbf{v}^I \cdot \mathbf{v}^I\right)^{(n+1)}. \tag{4.39}$$

The conservation of mass equation leads to the density update. For Lagrangian SCNI formulation, it has the following simple form

$$\rho^{I(n+1)} = \frac{\rho^{I(0)}}{\det(\overline{\mathbf{F}}\left(\mathbf{X}_I\right)^{(n+1)})}, \tag{4.40}$$

while for semi-Lagrangian formulation, $\overline{\mathbf{F}}$ is not defined and the density is updated by solving the conservation of mass equation in an equivalent form of equation (3.1),

$$\frac{\mathrm{d}\rho}{\mathrm{d}t} = -\rho\left(\nabla^{\mathbf{x}} \cdot \mathbf{v}\right). \tag{4.41}$$

Therefore if the forward Euler scheme is applied to the above equation, the nodal density is updated as

$$\rho^{I(n+1)} = \rho^{I(n)}\left(1-\nabla^{\mathbf{x}}\cdot\mathbf{v}^{I(n)}\right). \tag{4.42}$$

With the updated internal energy and density at hand, the pressure at each node is then computed by the EOS (assuming ideal gas),

$$P^{I(n+1)} = \left(\gamma-1\right)\rho^{I(n+1)}e^{I(n+1)}. \tag{4.43}$$

4.5 TIME INTEGRATION PROCEDURES

The Newmark-beta time integration is employed for temporal discretization of equation (4.4) with $\beta = 0$, and $\gamma = 1/2$ yielding the explicit central difference scheme. The central difference time integration procedures are given as follows in predictor-corrector format:

(1) Initialization:

(a) Form lumped mass **M**, and initial external force $\boldsymbol{f}^{\text{ext}(0)}$.

(b) Compute the initial nodal acceleration by

$\mathbf{M}\boldsymbol{a}^{(0)} = \boldsymbol{f}^{\text{ext}(0)}$.

(2) At (n+1)th time step

(a) Predictor phase (predicted variable is denoted with '^')

$\hat{\mathbf{u}}^{(n+1)} = \mathbf{u}^{(n)} + \Delta t\,\mathbf{v}^{(n)} + \dfrac{\Delta t^2}{2}\boldsymbol{a}^{(n)}$,

$\hat{\mathbf{v}}^{(n+1)} = \mathbf{v}^{(n)} + \dfrac{1}{2}\Delta t\,\boldsymbol{a}^{(n)}$.

(b) Compute smoothed spatial gradient $\overline{\nabla}^{\mathbf{x}}\Psi^{(n+1)} = \overline{\nabla}^{\mathbf{x}}\Psi^{(n+1)}(\hat{\mathbf{u}}^{(n+1)})$ (If Lagrangian, according to equation (4.19)).

(c) Compute $\overline{\boldsymbol{\beta}}^{(n+1)}$ according to equation (4.23) (Lagrangian) or (4.34) (semi-Lagrangian).

(d) Compute predictors $\boldsymbol{\sigma}^{\mathrm{d}(n+1)}(\hat{\mathbf{u}}^{(n+1)})$ (if solid) and $P^{(n+1)}(\hat{\mathbf{u}}^{(n+1)})$.

(e) Compute $\boldsymbol{f}^{\mathrm{ext}(n+1)}$, $\boldsymbol{f}^{\mathrm{d}(n+1)}$

(f) Compute $\boldsymbol{f}^{\mathrm{v}*(n+1)}$ by solving Riemann problems from predictors.

(g) Compute energy (if fluid) $E^{(n+1)} = E^{(n+1)}(\hat{\mathbf{v}}^{(n+1)}, \overline{\boldsymbol{\beta}}^{(n+1)})$ and $e^{(n+1)}(\hat{\mathbf{v}}^{(n+1)}, \overline{\boldsymbol{\beta}}^{(n+1)})$ according to equation (4.37) and (4.39) respectively.

(h) Solve $\mathbf{M}\boldsymbol{a}^{(n+1)} = \boldsymbol{f}^{\mathrm{ext}(n+1)} - \boldsymbol{f}^{\mathrm{d}(n+1)} - \boldsymbol{f}^{\mathrm{v}*(n+1)}$ for $\boldsymbol{a}^{(n+1)}$.

(3) Corrector phase:

$$\mathbf{v}^{(n+1)} = \mathbf{v}^{(n)} + \frac{1}{2}\Delta t\left(\boldsymbol{a}^{(n)} + \boldsymbol{a}^{(n+1)}\right),$$

$$\mathbf{u}^{(n+1)} = \hat{\mathbf{u}}^{(n+1)}.$$

(4) If $t < t_{final}$ let $n \to n+1$ and go to (a) in step 2.

4.6 NUMERICAL EXAMPLES

A set of benchmark problems including both solid and fluid dynamics are examined in this section. For all the numerical examples, the normalized RK support size is set to be 1.75 times of the nodal spacing and linear basis and cubic spline kernel function are employed. For the sake of simplicity, 'LAG-SCNI' denotes the case using Lagrangian SCNI without the proposed shock algorithm; 'LAG-SCNI-SHOCK' denotes Lagrangian SCNI with the shock algorithm; 'SEMI-LAG-SNNI-SHOCK' denotes semi-Lagrangian SNNI and the shock algorithm. The implementation of the algorithm is in a three-dimensional code. The first two examples are examined to show the ability to correctly represent shock physics in solids and the last two are designed to test whether the formulation is able to correctly represent strong shocks physics in compressible fluids. In all but the last example, the discretization required for reasonable accuracy is course

enough as to not require additional stabilization of nodal integration [58], which will be considered in future work.

4.6.1 One-dimensional elasto-plastic bar impact

In this problem, an elasto-plastic bar with initial velocity of 273 m/s impacts another bar of the same material initially at rest, as shown in Figure 4.4. The bars are made of 6061 T-6 aluminum and described by a perfect plasticity model with Young's modulus E = 77.11GPa, Possion's ratio υ = 0.334, density ρ = 2703 kg/m^3 and yield strength Y_0 = 270 MPa. In this case, only weak shock waves are produced in the bar. The problem is modeled as one-dimensional; the two lateral directions are fixed (as rollers) as shown in Figure 4.4. This impact velocity 273 m/sec is designed such that it is sufficient to cause the yield strength to be exceeded so that an elastic wave is formed and followed by a plastic wave. There exists an analytical solution for this problem, see chapter 10 in [59]. The lengths for both bars are 50 mm and discretized with 800 nodes in the axial direction. The axial stress and velocity distribution at time t = 6 μsec are given in Figure 4.5 for three cases, LAG-SCNI-SHOCK, SEMI-LAG-SNNI-SHOCK and LAG-SCNI. From the figure, one can observe that LAG-SCNI captures the correct shock speed and jump, but with severe oscillations due to the Gibbs phenomenon. On the other hand, the proposed methods LAG-SCNI-SHOCK and SEMI-LAG-SNNI-SHOCK capture the correct shock speed and jump and do not suffer from the Gibbs phenomenon.

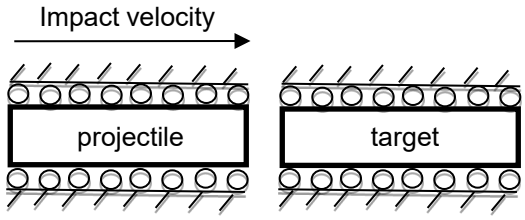

Figure 4.4. Schematic diagram for one-dimensional elasto-plastic bar impact

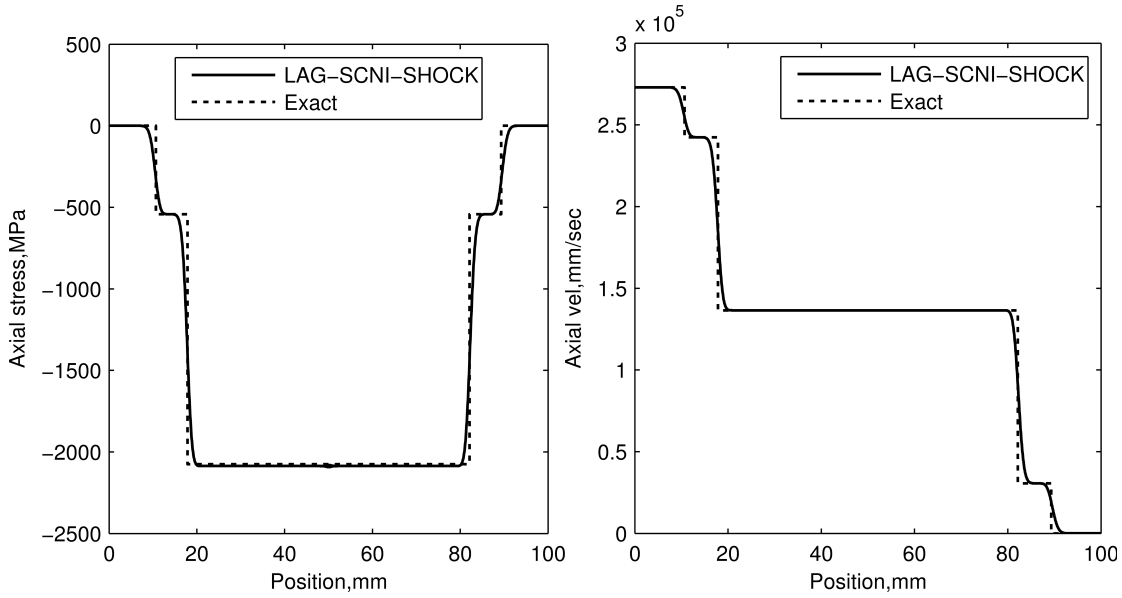

(a)

Figure 4.5. One-dimensional elasto-plastic bar impact, axial stress and velocity distribution $t = 6$ μsec (a) LAG-SCNI-SHOCK, (b) SEMI-LAG-SNNI-SHOCK and (c) LAG-SCNI.

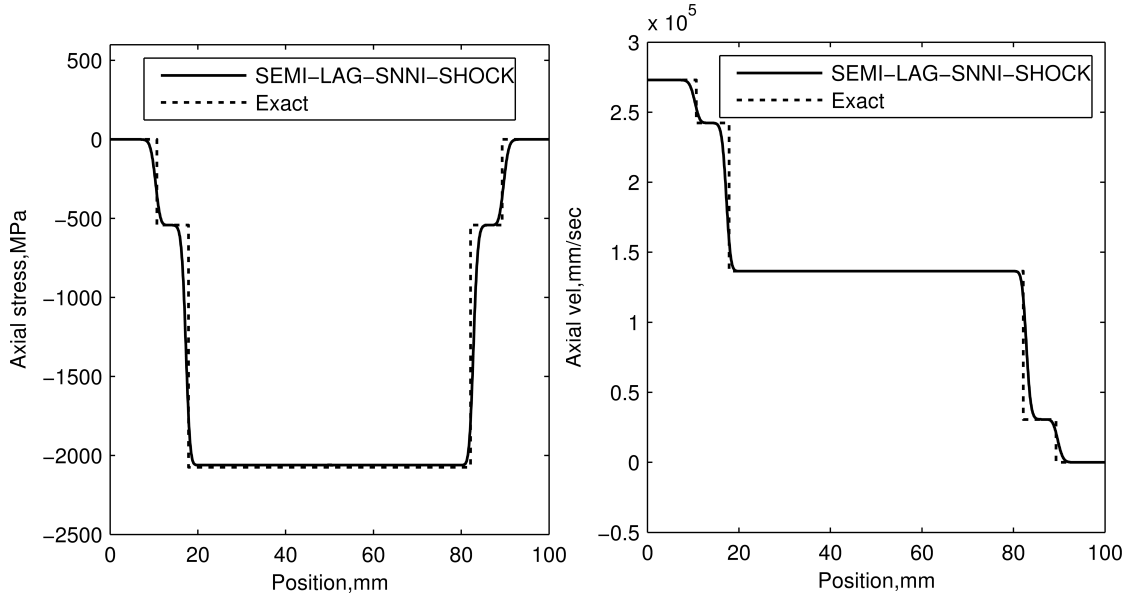

(b)

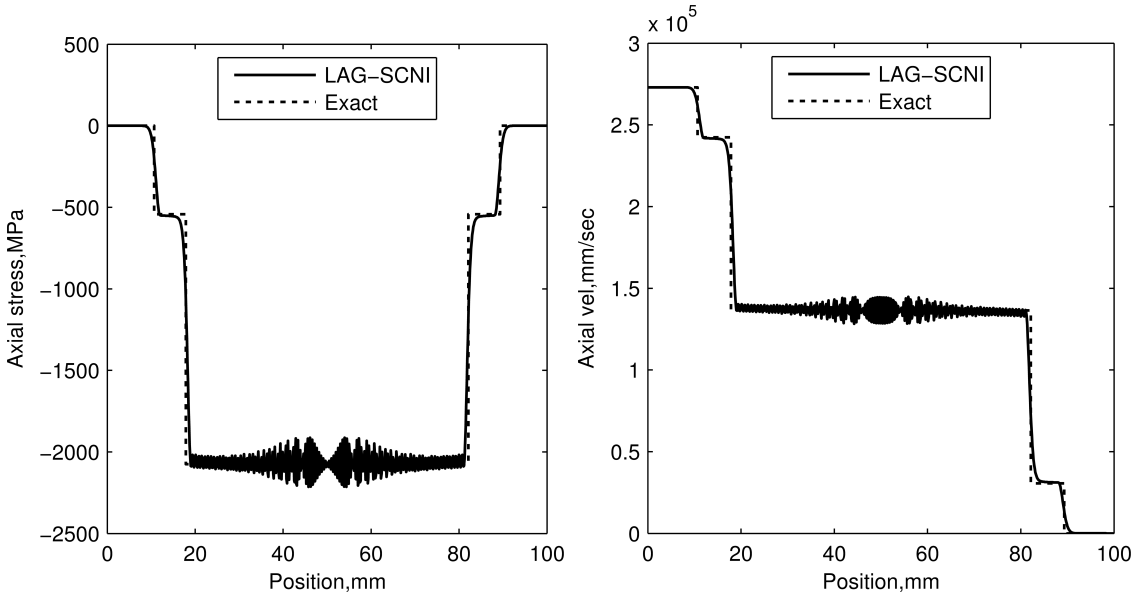

(c)

Figure 4.5. One-dimensional elasto-plastic bar impact, axial stress and velocity distribution t = 6 μsec (a) LAG-SCNI-SHOCK, (b) SEMI-LAG-SNNI-SHOCK and (c) LAG-SCNI. (Continued)

4.6.2 Two-dimensional plate impact with rarefaction waves

In this problem, a two-dimensional plane-strain high velocity plate impact problem is considered where the edges are unconstrained and allow lateral deformation. Peak pressure behind the shock wave is measured in the experiment by Marsh [60]. The unconstrained edges result in multi-dimensional wave propagation as the traction free boundary condition generates a rarefaction wave propagating inside from the edges. Consequently, this problem assesses the formulation accuracy for multi-dimensional wave propagation and rarefaction formation. The model was constructed as two plates impacting at a velocity of 1,000 m/sec. It can be noted that this velocity is typical of a high velocity ballistic impact. Each plate is 8 mm wide by 2 mm thick and was discretized with 161 nodes across the width and 41 nodes through the thickness. The impact surface is along the 8 mm edge. The material is 6061 T-6 aluminum, modeled with the same material properties and constitutive model as the previous problem. The pressure contours at time $t = 0.25$ μsec is given in Figure 4.6. As expected, a compression wave propagates along the impact direction while the rarefaction wave grows from the lateral edges and relieves the pressure in the initially compressed region. In the experiment, the peak pressure is measured as 8 GPa [60]. The numerical peak pressures obtained from the three cases are (a) LAG-SCNI, 8.820 GPa with 10.25% difference (b) LAG-SCNI-SHOCK, 7.612 GPa with 4.85% difference and (c) SEMI-LAG-SNNI-SHOCK, 7.611 GPa with 4.86% difference. All the three give acceptable solution in terms of peak pressure, however the two methods with the shock algorithm provide better accuracy. In addition, the oscillations are almost non-existent when using the proposed shock algorithm.

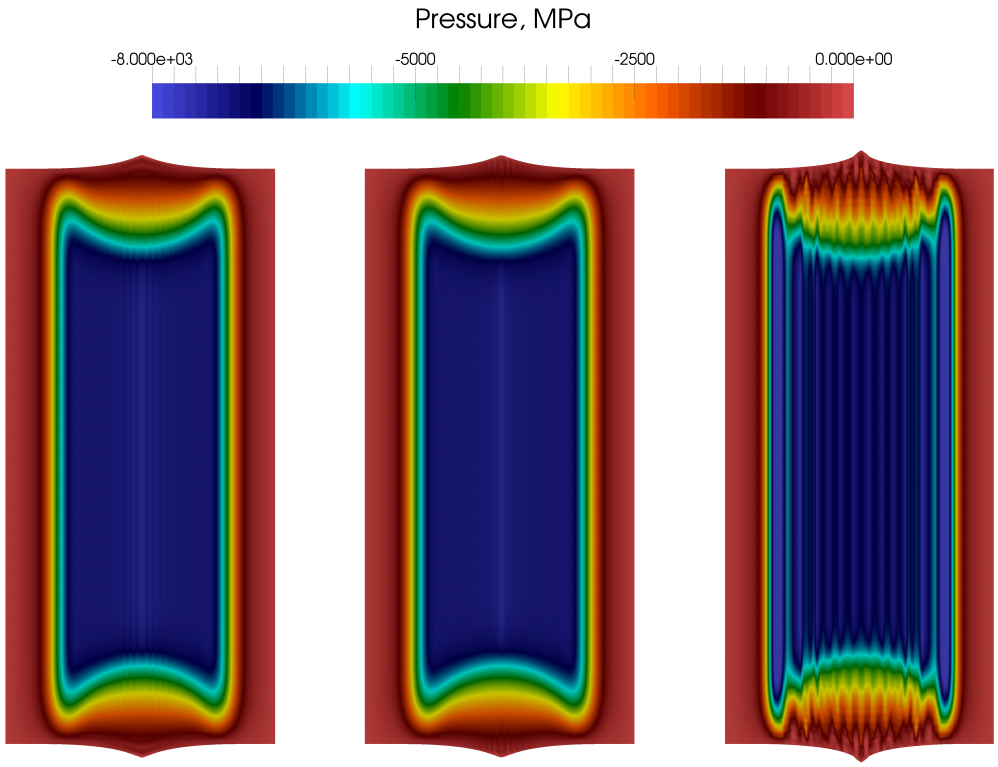

(a) (b) (c)

Figure 4.6. Two-dimensional plate impact with rarefaction waves, pressure contours at time t 0.25 μsec (a) LAG-SCNI-SHOCK, (b) SEMI-LAG-SNNI-SHOCK and (c) LAG-SCNI.

4.6.3 Two-dimensional Noh implosion problem

In two-dimensional Noh implosion problem [54] , the cold gas (with zero internal energy) moves toward a center from all the directions with a unit velocity. This process generates a strong shock wave propagating toward outside. This problem tests the ability to capture the physics of strong shock waves, and whether a method is capable of correctly transforming the kinetic energy into internal energy in strong shock problems. The gas is described by EOS of ideal gas with the adiabatic index $\gamma = 5/3$ and initial density $\rho^{(0)} = 1.0$. Only one quarter of the whole domain is modeled. The domain size is 1.0 × 1.0 and a uniform node distribution 40 × 40 is used to perform this simulation. The initial velocity is

a unit velocity pointing to the origin, i.e. $\mathbf{v}^{(0)} = -\mathbf{r} / |\mathbf{r}|$ ($\mathbf{r}$ is the position vector). The initial pressure is zero, but for numerical purposes it is set to 10^{-6}. Since the code is three-dimensional and in order to model this two-dimensional problem, two layers of nodes are used in the out of plane direction, fixed in that direction to form a plane strain problem. Only the top quarter of the domain is modeled, with the left and bottom edge prescribed with the appropriate symmetry condition. On the right edge and top edge, the boundary pressure is equal to the initial pressure.

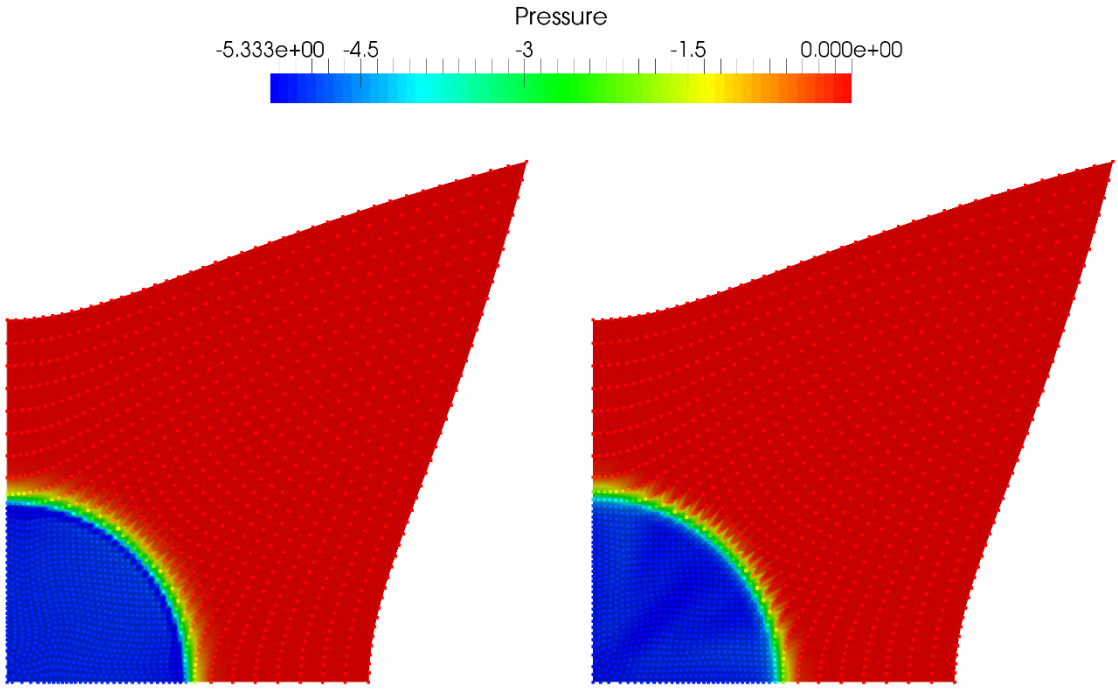

(a) (b)

Figure 4.7. Two-dimensional Noh implosion problem, pressure contours at time $t = 0.6$, (a) LAG-SCNI SHOCK, and (b) SEMI- LAG-SNNI-SHOCK. (dots represent the nodes in the current configuration)

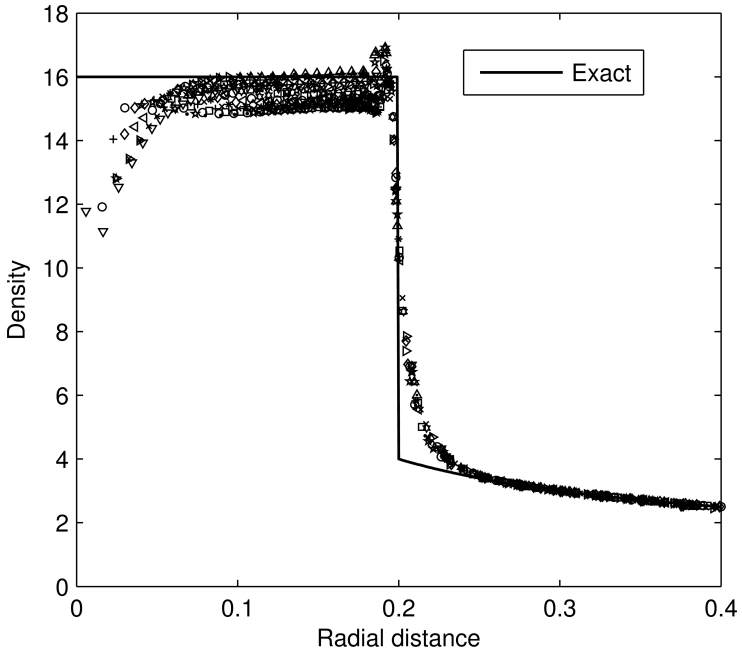

(a)

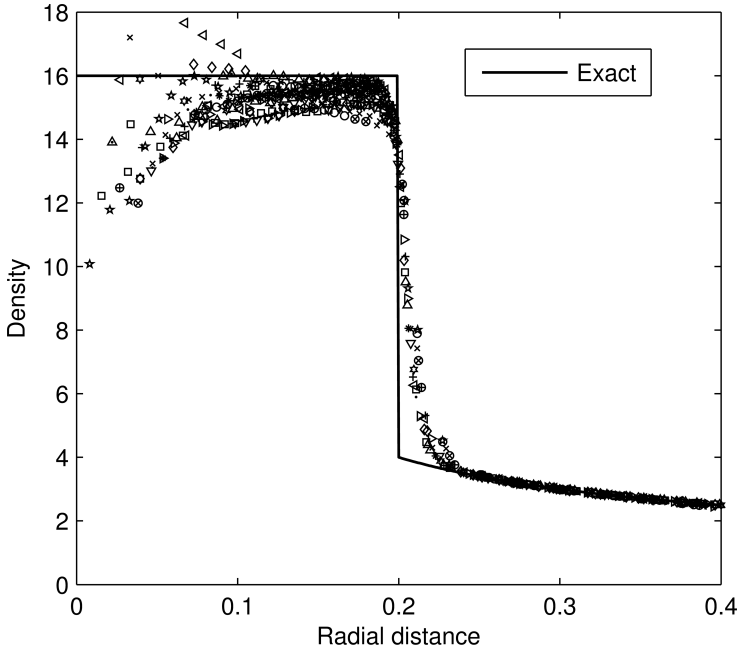

(b)

Figure 4.8. Two-dimensional Noh implosion problem, the scatter plot of density v.s. radial distance at time $t = 0.6$, (a) LAG-SCNI-SHOCK, and (b) SEMI- LAG-SNNI-SHOCK.

The Noh implosion problem is computed until time $t = 0.6$ using both formulations, LAG-SCNI-SHOCK and SEMI-LAG-SNNI-SHOCK. Note that for this class of strong

shock problems, the numerical solution by using the formulation, LAG-SCNI (without shock algorithm) diverges due to severe oscillation and therefore only the results by using shock algorithms are shown. First, the contours of pressure are given in Figure 4.7. In the figure, we can see LAG-SCNI-SHOCK and SEMI-LAG-SNNI-SHOCK give quite stable results. The scatter plot for density is also shown in Figure 4.8. In the plots, the density distribution for every 2° between 0° and 45° are plotted with different angles marked by different markers. According to the analytical solution [54], at time t = 0.6, the shock wave travels a radial distance 0.2 from the origin with a peak post-shock density $\rho^{(t=0.6)}=16$. In Figure 4.8, the results are compared with the analytical solution. It shows that for both formulations, LAG-SCNI-SHOCK and SEMI-LAG-SNNI-SHOCK, the shock wave arrives at $|\mathbf{r}|$ = 0.2 which shows the method accurately captures the shock speed, and on the other hand the peak post-shock density shows very good agreement to the analytical value 16 which shows the method captures the shock jump. The drop in density near the origin is due to the known 'wall-heating' error [54] in the Lagrangian hydrodynamics formulation, which is expected. This can be remedied by adding artificial heat [54] which is not considered in this study.

4.6.4 Two-dimensional Sedov blast wave problem

In the Sedov blast wave problem [55], a sudden release of the energy at the origin generates an expanding shock wave. The initial condition of the problem consists of zero velocity field and the Dirac delta distribution of the internal energy at the origin. This problem examines whether a method is capable to correctly transform internal energy into kinetic energy, which is opposite to the previous Noh implosion problem in 4.3 in terms of the energy transformation. The gas is described by EOS of ideal gas with the adiabatic

index $\gamma = 1.4$ and initial density $\rho^{(0)} = 1.0$. A two-dimensional version of the problem is considered with plane strain condition imposed as previously discussed. Only the top right quarter of the problem is modeled; the left edge and bottom edge the boundary conditions are prescribed the symmetry condition. The size of the domain is chosen as 1.2×1.2 and is discretized by uniform node distribution of 48×48 nodes. In order to approximate the Dirac delta function, the four nodes nearest to the origin are assigned non-zero energy with a bilinear distribution which attains the maximum at the origin and vanishes between the second and third row of nodes, and the second and third column of nodes. The value of the bilinear function at the origin is set such that the total energy is 0.25. For numerical purposes, the initial pressures for the rest nodes are set to 10^{-6}. For the free boundaries, the boundary pressure is also prescribed this value.

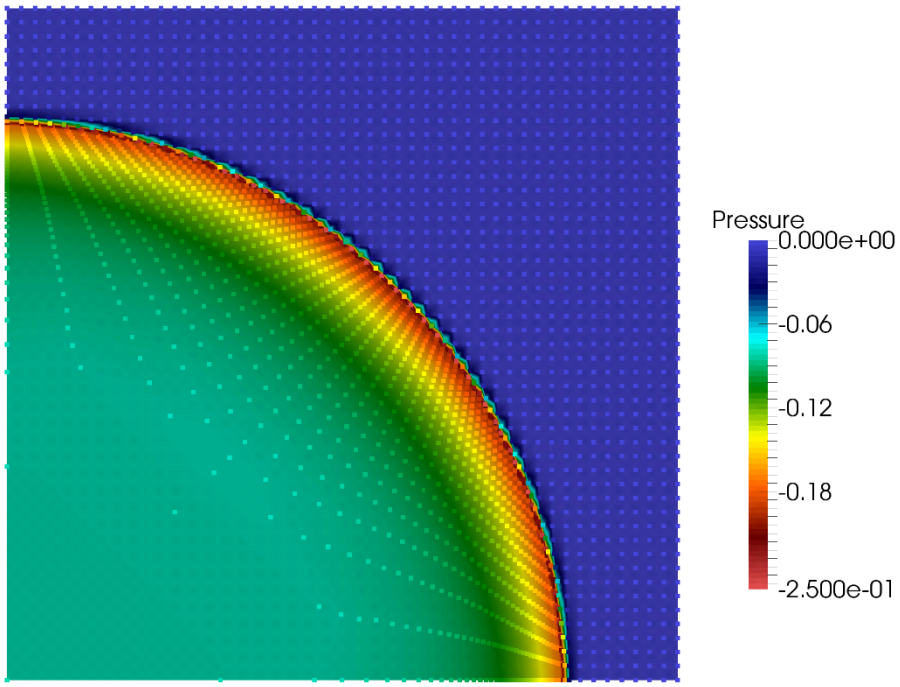

Figure 4.9. Two-dimensional Sedov blast wave problem, pressure contour at time $t = 1.0$. (dots represent the nodes in the current configuration)

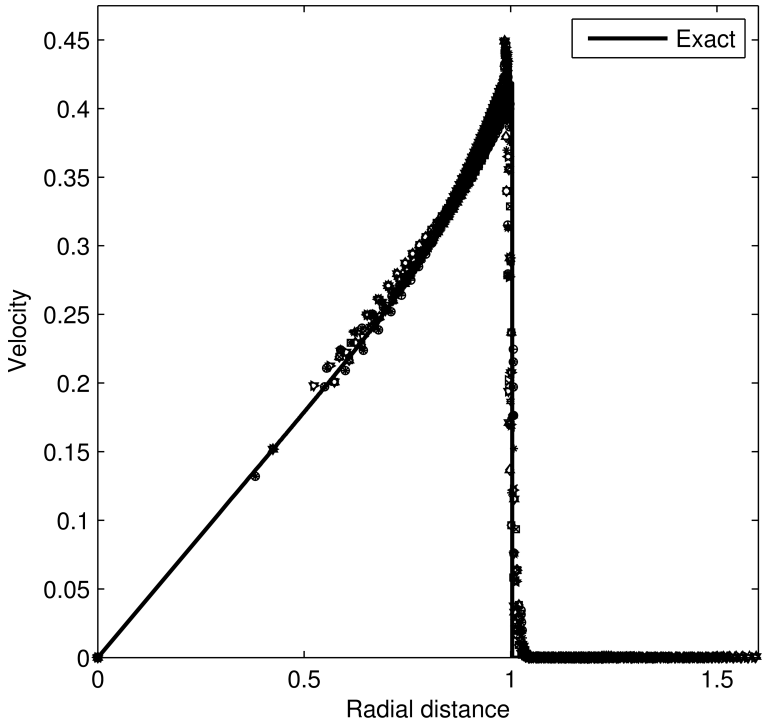

Figure 4.10. Two-dimensional Sedov blast wave problem at time $t = 1.0$, the scatter plot of velocity v.s. radial distance.

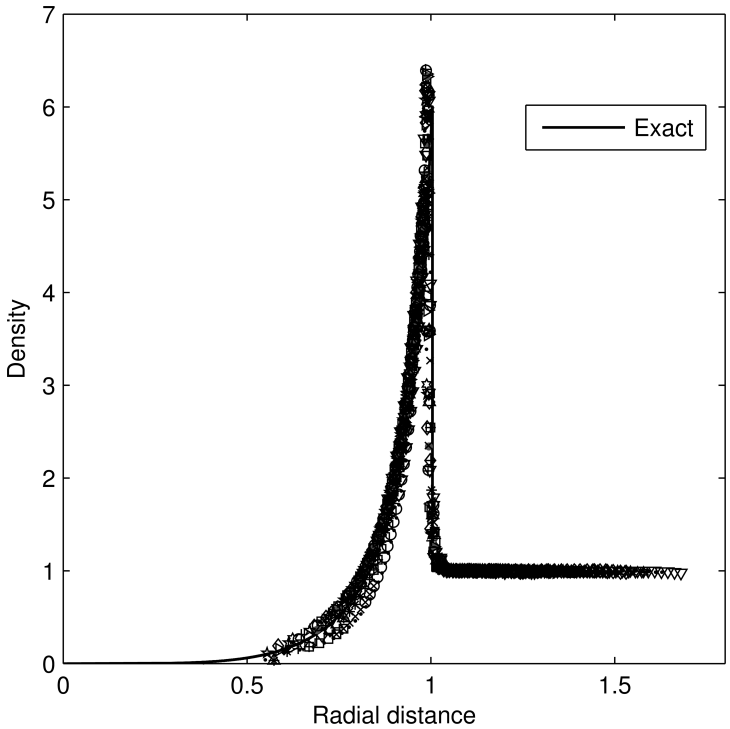

Figure 4.11. Two-dimensional Sedov blast wave problem at time $t = 1.0$, the scatter plot of density v.s. radial distance.

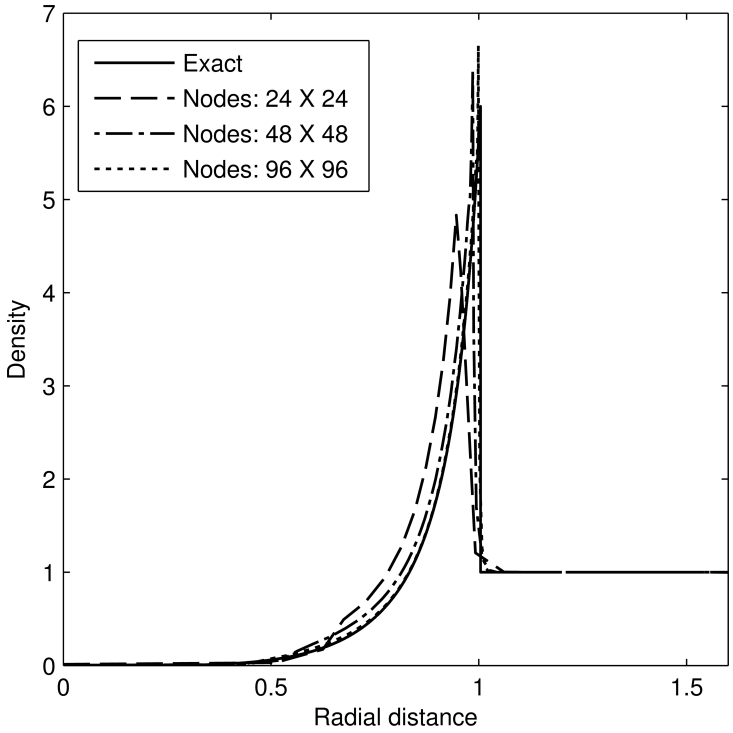

Figure 4.12. Two-dimensional Sedov blast wave problem at time t = 1.0, density distribution along 45° radial direction using varying discretizations.

In this Sedov blast problem, LAG-SCNI-SHOCK is used only. LAG-SCNI (without shock algorithm) again diverges due to the strong shock effect. Since the problem is discretized finer than the previous examples, SEMI-LAG-SNNI-SHOCK shows instability in the form of node-to-node oscillation, which is expected in finer discretizations when no stabilization for nodal integration is employed. Therefore, only the results obtained by using LAG-SCNI-SHOCK are present here to show the effectiveness of this framework, setting aside this issue. The simulation is run until time t = 1.0. First, the contour of pressure is given in Figure 4.9. In the figure, we can see LAG-SCNI-SHOCK gives a stable result with a sharp shock front. The scatter plot for radial velocity and density are also shown in Figure 4.10 and Figure 4.11 respectively. In the plots, the variable distribution for every 2° between 0° and 45° are plotted at different angles marked by different markers. According to the analytical solution [55], at time t = 1.0, the shock wave

travels a radial distance 1.0 from the origin with a peak post-shock radial velocity 0.415 and density 6.0. The figures show that in the simulation using LAG-SCNI-SHOCK, the shock wave arrives at $|\mathbf{r}| = 1.0$ which shows the method accurately captures the shock speed. The velocity and density distributions behind shock front also show good agreement with the exact solutions. The result shows good radial symmetry even though a radial mesh is not used. Lastly, a convergence study based on the discretization sequence of 24 × 24 nodes, 48 × 48 nodes, and 96 × 96 nodes. The density distributions in these three cases at the 45° radial direction are given in the Figure 4.12. From the figure, it is clear the solution converges with mesh refinement.

4.7 CONCLUSION

In this chapter, a new algorithm is developed to introduce shock physics into semi-Lagrangian Galerkin meshfree methods. In this approach, the Godunov scheme is embedded in the volumetric internal force via a purely node-based flux gradient evaluation. The coefficients for converting the results of the Riemann problems between nodes to the enriched pressure and velocity are obtained by a domain integral as opposed to cells, which makes it possible to dispense with cells altogether. The anti-symmetric property of the coefficients in the proposed method ensures the conservation of linear momentum and energy for the volumetric contribution. This approach can also be applied to other Galerkin meshfree methods, as well as mesh-based Galerkin methods such as FEMs and IGA.

The method proposed is broad and is applicable to different types of nodal integration. It was shown to be an effective technique for the nodal integrations tested, for problems involving both weak and strong shocks, in both solids and fluids. This included SCNI under a Lagrangian RKPM formulation and notably SNNI under a semi-Lagrangian

RKPM formulation. This work paves the way for modeling shock-induced fragmentation problems, which are to be discussed in next two chapters.

ACKNOWLEDGEMENTS

This Chapter 4 is currently being prepared for submission for publication of the material. J.S. Chen, G. Zhou, M. Hillman, 'A Godunov-type Shock Capturing Algorithm in Galerkin Meshfree Methods for Solid and Fluid Dynamics'. The dissertation author was the primary investigator of this material.

Chapter 5

A Semi-Lagrangian Reproducing Kernel Particle Method Framework for Modeling Transient Dynamic Failure of Concrete Structures Subjected to Blast Loadings

5.1 INTRODUCTION

Concrete is one of the most common construction material for civil and defense infrastructures. Blast loadings and their effects on these concrete structures have received considerable attention in recent years due to the many accidental or intentional events that have damaged important structures. It is a multi-physical process: a strong shock wave is first generated in the explosive gas after the ignition of the high explosive; then it propagates through air and, finally hits the structure and imparts the shock wave into solid via FSI, causing the concrete material spalling and fragmentations. The objective of this dissertation is to develop a framework capable to effectively capture those key phenomena, which is presented in this chapter.

The new formulation discussed in chapter 4 is adopted here to model the strong shock waves in both fluid and solid fields. These two media are all discretized by Lagrangian particles, and thus the interface is naturally described without extra tracking efforts when fragmentations occur. The fluid-structure interaction is addressed by the level set enhanced natural kernel contact algorithm (LSENKC) [44].

This chapter is organized as follows. In section 2, the details of high explosive physics and modeling under meshfree framework are discussed. In section 3, an approach is proposed to obtain an equivalent shock Hugoniot for the Riemann solver from a general concrete material model with the damage considered. The fluid-structure interaction by the LSENKC algorithm is described in section 4. In section 5, a reinforced concrete (RC) column subjected to blast loading is modeled to show the effectiveness of this framework, and followed by conclusions in section 6.

5.2 HIGH EXPLOSIVE MODELING

In the blast, the shock wave initiates from the high explosive (HE) and in this section the basic physics and modeling technique are discussed.

5.2.1 High explosive physics and modeling

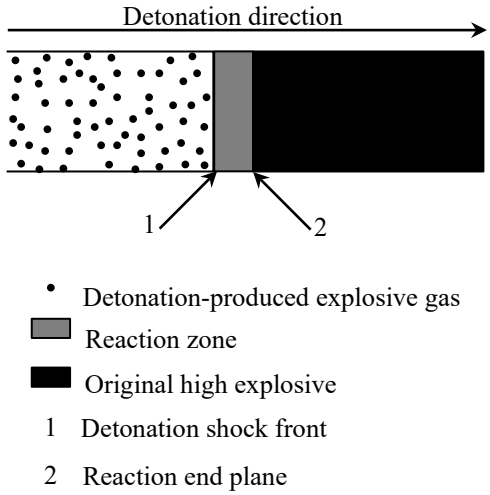

Figure 5.1. High explosive detonation.

The HE explosion process involves in a violent chemical reaction which converts the original high energy explosive charge into gas at very high temperature and pressure. A typical HE explosion consists of the detonation process which is the propagation of the reactive wave phenomenon that advances through the explosive with constant detonation velocity. As shown in Figure 5.1, it has three zones, i.e. original high explosive, reaction zone and the detonation-produced explosive gas. In a steady state detonation process, the reaction rate is essentially infinite and the chemical equilibrium is attained. As shown in Figure 5.1 a shock front moves with a detonation velocity D and compresses the HE from

an original status point (P_0, V_0) to another specific status point (P_1, V_1) along the Hugoniot curve of HE, and proceeds the chemical reaction in a very thin reaction zone. Chapman and Jouguet's hypothesis states that for a plane detonation wave to propagate steadily, the Rayleigh line must be tangential to the Hugoniot curve of the gaseous detonation products (see Figure 5.2) at the C-J point.

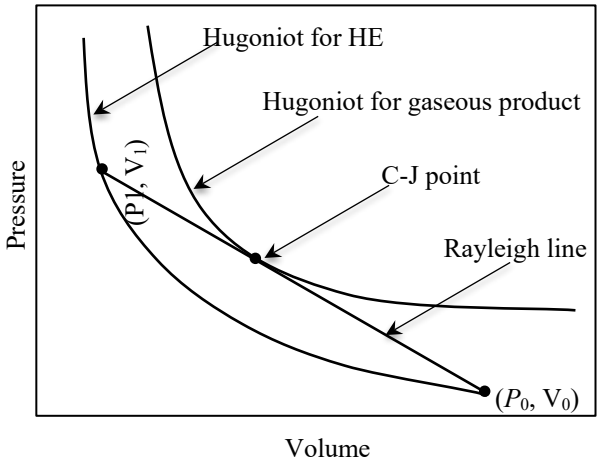

Figure 5.2. Schematic Hugoniots and Rayleigh line.

In this study, TNT is used as the high explosive and the material properties are, initial density $\rho^{(0)}$ = 1630 Kg/m^3, detonation velocity D = 6930 m/sec, CJ pressure $P_{C\text{-}J}$ = 2.1×10^{10} Pa. A possible choice of the equation of state of explosive gaseous product is to simply use the ideal gas that takes the form of

$$P = (\gamma - 1)\rho \mathrm{e} \tag{5.1}$$

where γ is generally taken as 3 for most of the high explosives [61]. Here, the equation of state in equation (5.1) is used for TNT with γ=3.

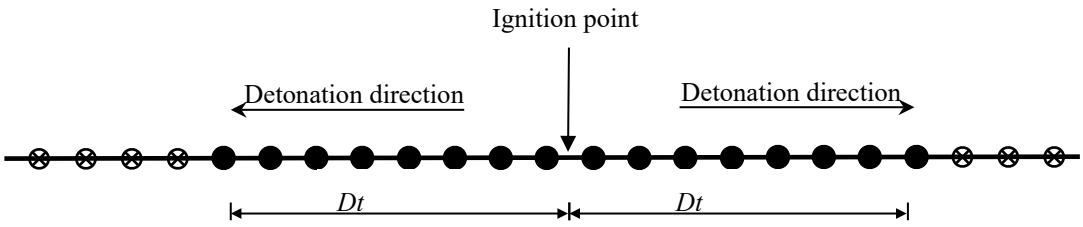

Figure 5.3. 1D high explosive, discretized by meshfree nodes.

The chemical reaction is not modeled explicitly in this work. Instead, an empirical formula is adopted by considering the high explosive physics discussed above. Based on the Chapman and Jouguet's hypothesis, in the stable state the detonation velocity should be a constant D and the state of the gaseous product should be at C-J point as shown in Figure 5.2. Therefore, D determines which node is trigged as gas. At the moment the node is being trigged, the C-J pressure is prescribed to the node. And after the detonation wave moves away, the node is then governed by the compressible hydrodynamics, namely all the conservation laws given in chapter 3. A 1D case as shown in Figure 5.3 is used to illustrate the algorithm. In the figure, it shows a 1D high explosive detonation which is initiated at point O and then propagates toward left and right with a constant detonation velocity D. The distances the two waves travel in both directions are Dt. At $t = 0$, all the meshfree nodes are not activated (i.e. with $P = 0$ and v = 0), and they are marked by empty dot in Figure 5.3. After time t, the nodes within the distance Dt from initiation point O are trigged (i.e with non-zero pressure) and they are marked by solid dot in the figure.

5.2.2 One-dimensional TNT slab explosion with detonation and dispersion

The approach to model the HE discussed above is validated by solving a one-dimensional TNT slab explosion with detonation and dispersion. In this problem, a one-

dimensional TNT slab explodes in the vacuum with detonation initiated from the left end ($x = 0$) as shown in Figure 5.4. After the ignition, the gas product disperses outwards with rarefaction wave advancing through the gas behind the detonation wave. The EOS of ideal gas is used with $\gamma = 3$ [61], and the C–J pressure can be approximated as,

$$P_{C-J} = \frac{1}{1+\gamma}\rho_0 D^2 = 1.957\times10^{10}\,Pa. \tag{5.2}$$

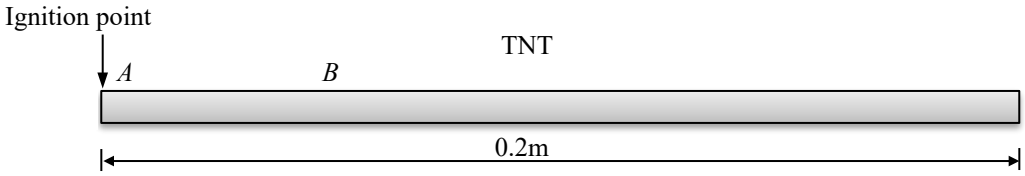

Figure 5.4. Detonation in a 1D high explosive, TNT.

In Figure 5.4, *A* denotes the ignition point and *B* denotes an RK node in the domain. The question is when should the node *B* be trigged by the detonation wave? The so-called burning function is defined for this purpose. Here a simple approach is used under meshfree framework,

$$P_B = P_{C-J} \quad if \;\; abs\left(\left|AB\right| - Dt\right) \le \beta a, \tag{5.3}$$

where *Dt* is the distance that the detonation wave has propagated, $\left|AB\right|$ is the distance between the ignition point *A* and the node *B*, *a* is the support size of node *B*, β defines the width reaction zone and in this study β =0.5, and $P_{C\text{-}J}$ is a given material parameter for TNT. After the node is trigged, the node becomes a gas product (fluid) node and it is then governed by compressible hydrodynamics. Note that this approach is applicable to multidimensional spaces case by replacing the distance measure accordingly. The pressure transient behind the detonation wave is given in a close form [62],

$$P = \frac{16}{27}\frac{\rho_0}{D}\left(\frac{x}{2t}+\frac{D}{4}\right)^3 . \tag{5.4}$$

The problem is solved using the formulation given in Chapter 4 with 1000 nodes and the numerical solutions at t = 10 μsec and t = 20 μsec are given in Figure 5.5. As shown, they agree very well with the analytical solutions and the shock front is modeled sharply without non-physical oscillations. This example shows the implementation of hydrodynamic code is correct and also the way to deal with the ignition and propagation of the detonation wave in TNT is also appropriate.

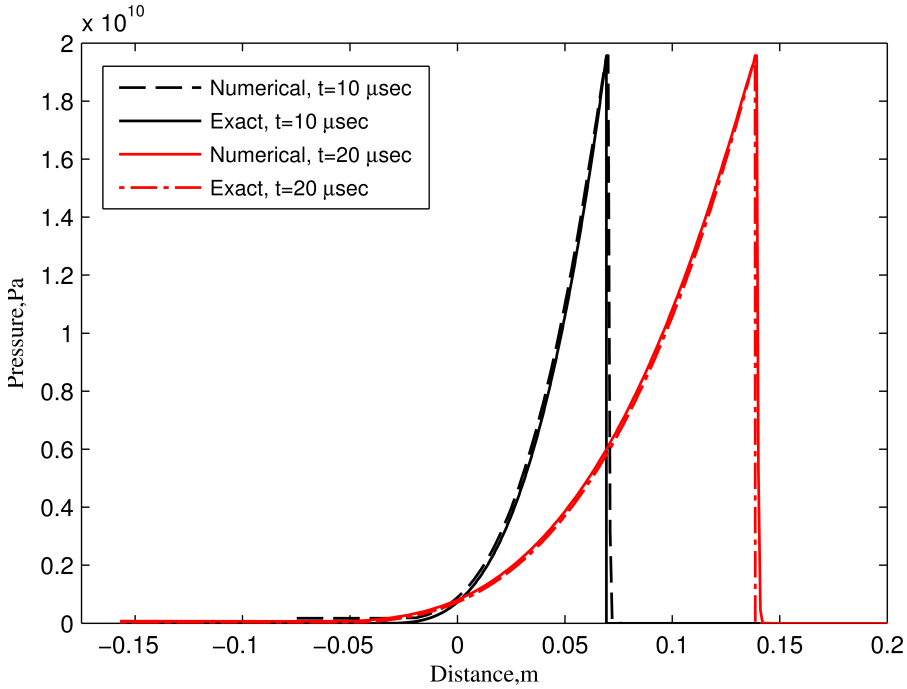

Figure 5.5. The detonation wave and the pressure distributions at t = 10 μsec and t = 20 μsec.

5.3 EQUIVALENT SHOCK HUGONIOT FOR CONCRETE

In this study, the concrete structure is modeled using the Advanced Fundamental Concrete (AFC) model [63] coupled with a microcrack informed damage model [64]. The AFC model is a 3-invariant plasticity model which incorporates damage evolution, strain rate effects, and a nonlinear pressure-volume relationship (equation of state) as shown in Figure 5.6. And the tensile damage evolution law is physically obtained from a microcell analysis [64] which considers the evolution of defects such as microvoids and microcracks.

In this framework, in order to capture shock discontinuity by introducing Riemann problem solution, a Hugoniot of the following form is required in the Riemann solver [51],

$$U_S = C_B(\mathrm{sgn}[[\dot{u}]]) + A[[\dot{u}]], \tag{5.5}$$

where U_S is the shock speed, $[[\dot{u}]]$ is the particle velocity difference across the discontinuity front and 'sgn' represents the sign of a real number, C_B and A are two material constants which is usually obtained by performing costly flyer plate experiments. This Hugoniot can be used to deduce an EOS [59], which also means it is equivalent to an EOS. Therefore if an EOS of a specific concrete is known beforehand, the Hugoniot of the form in equation (5.5) can be derived accordingly. In terms of AFC concrete model, the two coefficients C_B and A can be consistently derived as

$$\begin{aligned} C_B &= \sqrt{\frac{K}{\rho}}\ , \\ A &= 1.0E-10 \approx 0. \end{aligned} \tag{5.6}$$

where K and ρ are the bulk modulus and the density in AFC respectively and therefore C_B is actually the sound speed of the concrete. In this way, it avoids the costly experiment by making use of the known EOS. The EOS in AFC model [63] is

$$P = \begin{cases} K_e \mu & for\ \mu \le \mu_{crush} \text{(elastic region)} \\ K_1 \bar{\mu} + K_2 \bar{\mu}^2 + K_3 \bar{\mu}^3 & for\ \mu_{crush} \le \mu \le \mu_{lock} \text{(crush-up region)}, \\ K_{lock}(\mu - \mu_0) & for\ \mu_{lock} \le \mu \text{(lock-up region)} \end{cases} \quad (5.7)$$

where $\bar{\mu} = \mu - \mu_{crush}$, K_e, K_1, K_2, K_3, K_{lock}, μ_{crush}, μ_{lock}, and μ_0 are given material constants, as shown in Figure 5.6 (μ is the volumetric strain which is assumed positive in compression, K is the bulk modulus, P is the pressure, D_T is the tensile damage and $T_{\max}$ the maximum tension limit). K can be obtained at different volumetric strain level by taking first-order derivatives of the EOS. That is

$$K = \begin{cases} K_e & for\ \mu \le \mu_{crush} \text{(elastic region)} \\ K_1 + 2K_2 \bar{\mu} + 3K_3 \bar{\mu}^2 & for\ \mu_{crush} \le \mu \le \mu_{lock} \text{(crush-up region)}. \\ K_{lock} & for\ \mu_{lock} \le \mu \text{(lock-up region)} \end{cases} \quad (5.8)$$

And C_B is obtained by substituting K into equation (5.6).

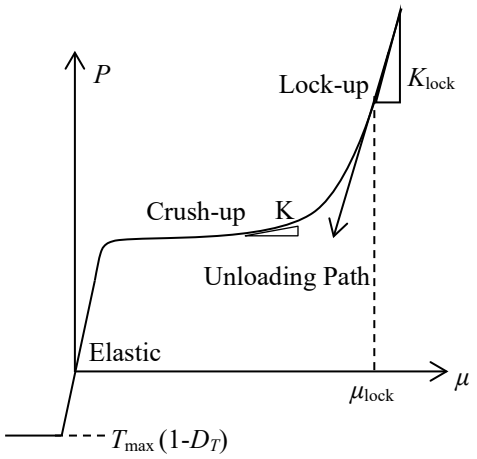

Figure 5.6. The equation of state in AFC.

Material damage affects the wave propagation speed. In AFC, for the volumetric response, there is only tensile damage applied and no volumetric compression damage. Therefore, considering tensile damage, the C_B is adjusted as

$$C_B = \sqrt{\frac{(1-D_T)K_e}{\rho}}, \qquad \text{if } \mu < 0 \text{ (in tension).} \tag{5.9}$$

This approach is validated by performing a numerical test, 1D concrete bar impact with velocity 100 m/sec. The numerical result with the derived shock Hugoniot is consistent with that obtained by using the original AFC model and free of spurious numerical oscillation as shown in Figure 5.7 ('SNNI-AFC' represents SNNI with original AFC; 'Riemann-SNNI-AFC' represents SNNI with shock algorithm and the Hugoniot derived from the original AFC).

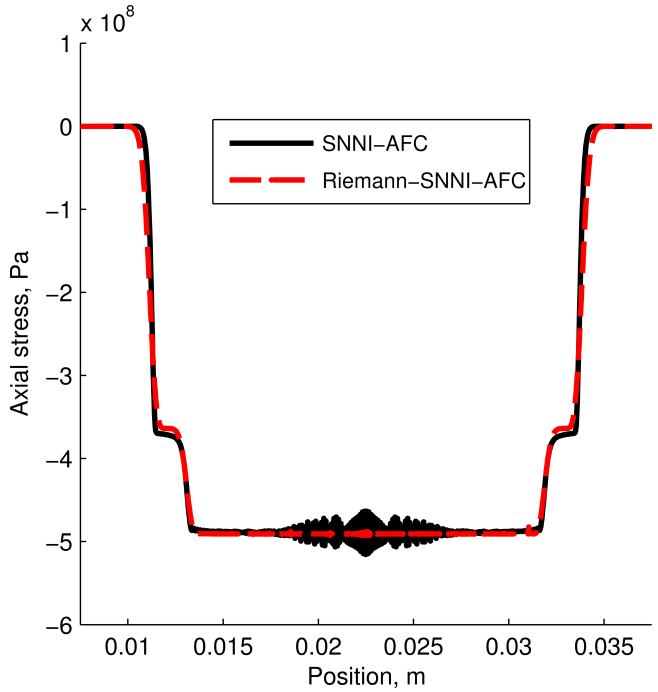

Figure 5.7. 1D concrete bar impact with velocity 100 m/sec, axial stress distribution.

In this section, one approach is proposed to couple the Riemann solver with AFC concrete model with micro-crack informed damage considered and as a general approach it can be extended to other concrete material models.

5.4 FLUID-STRUCTURE INTERACTION MODEL

5.4.1 FSI modeling via a contact algorithm

In Figure 5.8, it shows the interface Γ_C of fluid domain Ω_F and solid domain Ω_S. At the interface, the following kinematic and dynamic interface conditions, which imply the continuity of the normal component of velocity and normal stress, must hold:

$$\begin{aligned} v_{iS} n_{iS} &= -v_{iF} n_{iF}, \\ \sigma_{ijS} n_{iS} n_{jS} &= P_F. \end{aligned} \tag{5.10}$$

where the subscripts 'S' and 'F' denote the solid and the fluid, respectively, and P_F represents the pressure in the fluid. There is no constraint in the tangential direction where the two media can slip freely due to the viscid flow assumption (no shear stress in fluid). In this work, both fluid and solid fields are described by Lagrangian particles, the condition in equation (5.10) is essentially the non-penetration and frictionless condition which can be fulfilled by the contact algorithm.

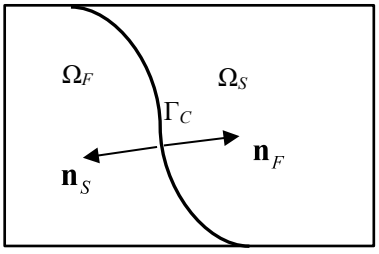

Figure 5.8. Interface of fluid and solid.

In the conventional contact algorithms, all possible contact surfaces (master surfaces) and contact nodes (slave nodes) are to be defined *a priori*. However, for problems which involve fragmentations such as concrete structure under blast loadings, contact surfaces are unknown and are part of the solution. Thus, the level set enhanced natural kernel contact (LSENKC) algorithm [44] is adopted.

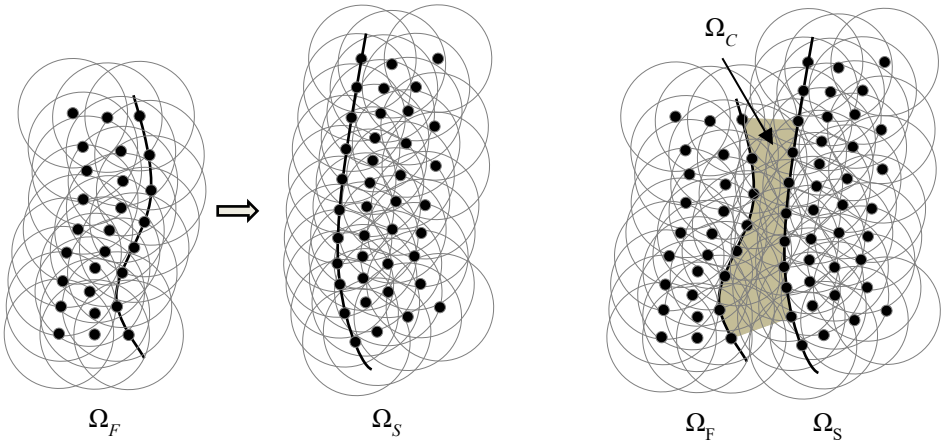

Figure 5.9. Natural kernel contact algorithm by kernel interaction between contacting fluid domain Ω_F and solid domain Ω_S: (a) fluid is impacting toward solid and (b) kernel overlapping and interacting in the contact zone Ω_C marked as shaded area.

The idea of the LSENKC algorithm emanates from the inherent property of the semi-Lagrangian RK shape functions. In the case of FSI, Figure 5.9 shows when the fluid domain Ω_F is approaching the solid domain Ω_S and the kernel supports associated with these two domains overlap in the contacting zone Ω_C, and it naturally serves as the non-penetration condition which is to be discussed in what follows.

It has been shown in [44] that contact conditions can be equivalently met by introducing an artificial elasto-perfectly-plastic material in the contacting zone Ω_C with the stress $\boldsymbol{\sigma}_C$ in this zone satisfying

$$\boldsymbol{\sigma}_C \cdot \mathbf{n}_S = t_N \mathbf{n}_S + \mathbf{t}_T, \tag{5.11}$$

where t_N and $\boldsymbol{t}_T$ are the normal and tangential contact forces respectively and here $\mathbf{n}_S$ is chosen as the contact normal direction. $\boldsymbol{\sigma}_C$ is determined by satisfying the following the yield function and the associated Karush-Kuhn-Tucker conditions based on a local coordinate system where *1*-direction is aligned with the contact surface normal $\mathbf{n}_S$.

$$\begin{aligned} & f(\boldsymbol{\tau}) = \|\boldsymbol{\tau}\| + \upsilon \hat{\sigma}_{11} \le 0, \\ & \dot{\mathbf{e}} = \gamma \frac{\partial f}{\partial \boldsymbol{\tau}}, \\ & \gamma \ge 0, \\ & \gamma f = 0, \end{aligned} \tag{5.12}$$

where υ is the friction coefficient (in this FSI slip-free case, $\upsilon = 0$) and γ is the consistency parameter, $\boldsymbol{\tau} = \begin{bmatrix} \hat{\sigma}_{12} & \hat{\sigma}_{13} \end{bmatrix}, \hat{\sigma}_{11} \le 0$ is the normal contact stress, $\dot{\mathbf{e}}$ is the tangential strain rate, $\hat{\boldsymbol{\sigma}} = \mathbf{L}\boldsymbol{\sigma}\mathbf{L}^T$ is the rotated Cauchy stress tensor onto the local coordinate system with *2*- and *3*- directions aligned with two mutually orthogonal unit vectors, **p** and **q,** which are laid on the contact surface and are orthogonal to $\mathbf{n}_S$, and $\mathbf{L} = [\mathbf{n}_S, \mathbf{p}, \mathbf{q}]^T$. Since $\upsilon = 0$, $\boldsymbol{\tau} = \begin{bmatrix} \hat{\sigma}_{12} & \hat{\sigma}_{13} \end{bmatrix} = \begin{bmatrix} 0 & 0 \end{bmatrix}$ according to equation (5.12). And then

$$\boldsymbol{\sigma}_C = \mathbf{L}^T \hat{\boldsymbol{\sigma}}_C \mathbf{L}, \tag{5.13}$$

where $\hat{\boldsymbol{\sigma}}_C = \begin{bmatrix} \hat{\sigma}_{11} & 0 & 0 \\ 0 & 0 & 0 \\ 0 & 0 & 0 \end{bmatrix}$.

When the fluid and the solid domains approach each other and the semi-Lagrangian RK shape function forms the partition of unit [4], as shown in Figure 5.10 (a), the interaction between the RK nodes from different domains induces non-zero internal forces

(see Figure 5.10 (b)). With the nodal integration scheme SNNI and consideration of the slip-free condition, the summation of the interactive forces associated with point *I* is

$$\mathbf{f}^I = \sum_{J \in N_I^C} \boldsymbol{\sigma}_C(\mathbf{x}_J) \cdot \bar{\nabla}^{\mathbf{x}} \Psi_I^{\mathbf{x}}(\mathbf{x}_J) V_J, \tag{5.14}$$

where $N_I^C = \left\{ J \middle| J \in \Omega_S \cup \Omega_F, \mathbf{r}_{IJ} \cdot \boldsymbol{\sigma} \cdot \mathbf{r}_{IJ} < 0, \mathbf{r}_{IJ} = (\mathbf{x}_I - \mathbf{x}_J) / \left\| \mathbf{x}_I - \mathbf{x}_J \right\| \right\}$ is the set that contains the neighbor points of point *I*, while contact stress between those points and point *I* is in compression. In this approach, the pair-wise interaction due to overlapping kernel functions naturally prevent the interpenetration between solid and fluid domains and consequently the conditions in equation (5.10) are met implicitly.

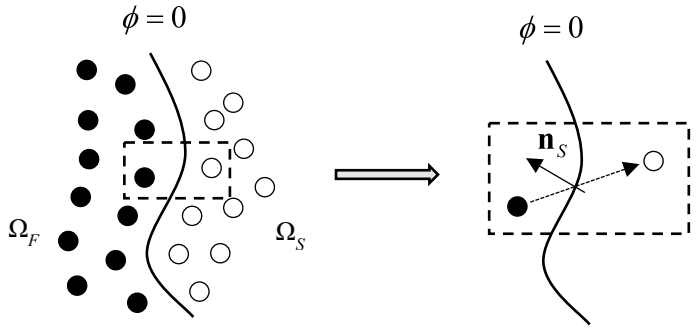

Figure 5.10. Determination of the zero level set and the contact surface normal for contact force calculation.

On the other hand, the definition of the interface surface and its normal direction are yet to be defined. In LSENKC [44], the level set function is constructed for this purpose by using the semi-Lagrangian-RK shape function:

$$\phi(\mathbf{x}) = \sum_{I \in \Omega_F \bigcup \Omega_S} \Psi_I^{\mathbf{x}}(\mathbf{x}) C_I, \tag{5.15}$$

where C_I is the level set nodal value associated with the RK shape function $\Psi_I^{\mathbf{x}}(\mathbf{x})$. Let the level set nodal value be defined as

$$C_I = \begin{cases} c & \text{if } I \in \Omega_F \\ -c & \text{if } I \in \Omega_S \end{cases}. \tag{5.16}$$

The interface surface position is defined by the set $\{\mathbf{x} | \phi(\mathbf{x}) = 0\}$ (see Figure 5.10) and surface outward normal can then be estimated using the level set function by

$$\mathbf{n}_S = -\frac{\nabla\phi}{\|\nabla\phi\|} \quad \text{on } \phi(\mathbf{x}) = 0. \tag{5.17}$$

The details about identifying the surface $\phi(\mathbf{x}) = 0$ are given in [44].

5.4.2 1D piston problem

A simple acoustic oscillator problem [40] is chosen as the first validation problem where there is an analytical solution available in the frequency domain. This problem is inspired by the well-known piston problem [65], which consists of a rigid-wall tube filled with a compressible fluid and closed by a moving piston at its right-hand side. In [40], the piston is replaced by a deformable solid bar of a finite length L_S (see Figure 5.11), since the interest here is the interaction of fluid and deformable solid bar. The initial equilibrium state of this coupled system is defined by a zero pressure and velocity inside the acoustic fluid and the solid bar. Given a perturbation, the system oscillates around a static equilibrium position. The derivation of the analytical frequency is given in [40].

The following geometric and material characteristics are used: L_F = 1.0 m, L_S = 0.2 m, S = 0.01 m^2 (cross section area), ρ_F = 1000.0 kg/m^3, ρ_S = 2000.0 kg/m^3, E = 200.0 GPa, υ = 0.0 (Possion's ratio), C_F = 1450.0 m/sec (speed of sound in fluid). In order to perturb the system, we apply to the solid a constant longitudinal tension force F = 12,500.0 N which is evenly distributed on all the solid particles lying on the fluid–structure interface. 1000 and 200 meshfree nodes are used to discretize the fluid and solid domain in the axial

direction respectively. According to the analytical solution, the exact period is 2.76 msec and the obtained numerical period is 2.72 msec, as shown in Figure 5.12. The accuracy of the numerical solution is very good (error of 1.7%).

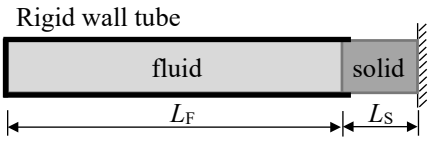

Figure 5.11. Piston problem.

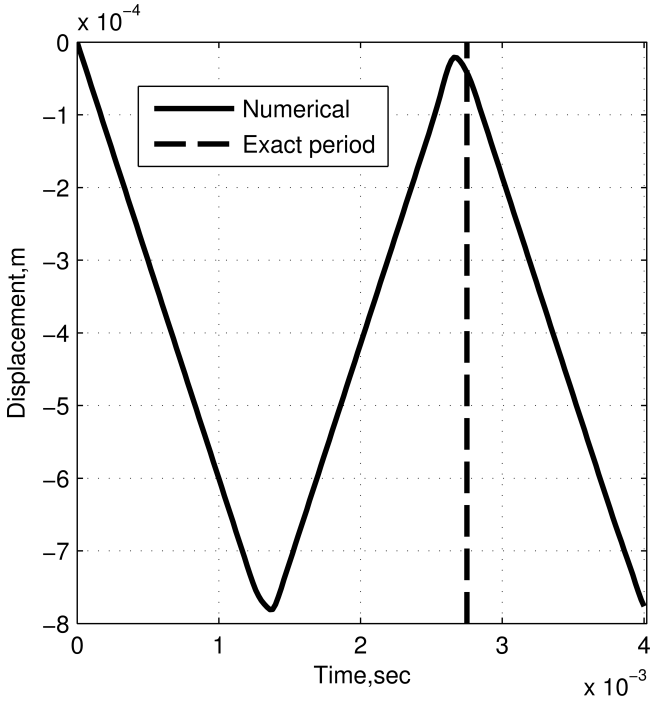

Figure 5.12. FSI computation: displacement history.

5.5 MODELING OF A REINFORCED CONCRETE COLUMN UNDER BLAST LOADING

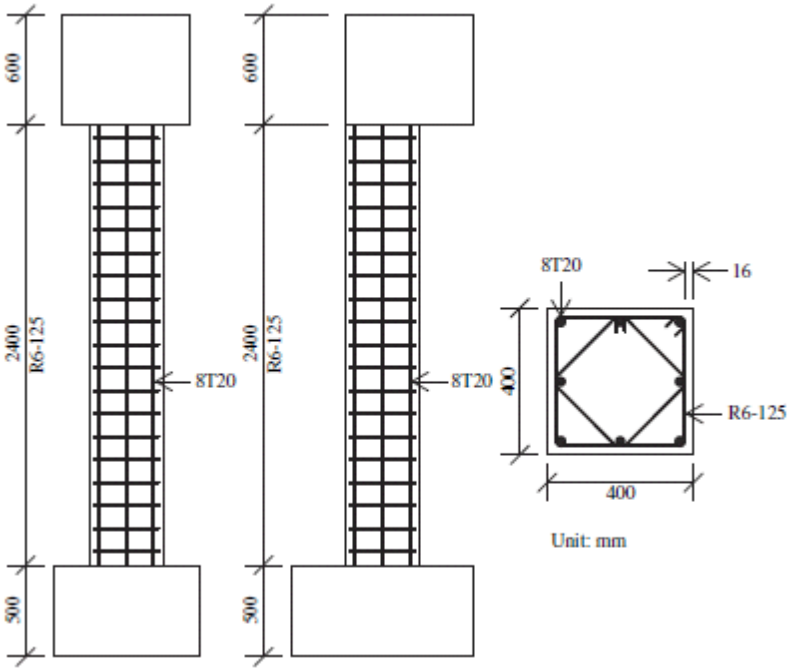

(a)

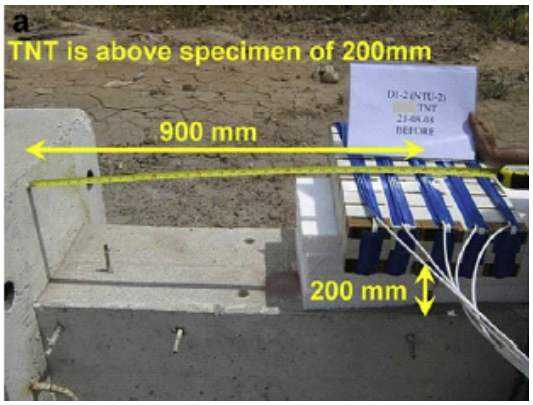

(b)

Figure 5.13. (a) Geometry and section details of RC column specimen, (b) test setup configuration (adapted from [66]).

In order to show the effectiveness of this framework, a reinforced concrete column under blast loading [66], on which there was experiment performed, is modeled in this section. The column specimen is included with a top head and a foundation. Figure 5.13 (a) shows the geometry and section details of the test specimen and the setup configuration

is given in Figure 5.13 (b). The TNT mass is 25 kg and the stand-off distance is 200mm. The characteristic of TNT is the same as given in section 2. According to [67], when the stand-off distance is less than 1.6 radius of TNT, the shock wave in the explosive gas is dominant and the effect of air is very small and therefore negligible. In this case, the equivalent radius of 25 kg TNT is 226 mm and obviously the air can be neglected since the real stand-off distance is only 200 mm. Therefore, for the sake of simplicity and saving computational cost, air is not modeled in this simulation. As shown in Figure 5.13 (a), T20 high tensile strength steel bars with a nominal yield strength of 420 MPa were used as longitudinal reinforcement and R6 mild steel bars with a nominal yield strength of 280 MPa were used a transverse reinforcement. And Young's modulus and Possion's ratio are 210 GPa and 0.3 respectively. The steel bars are modeled by the standard $J2$ plasticity. Ready-mix concrete, with a characteristic compressive strength of 30 MPa at 28 days, 13 mm aggregate size and slump of 125 mm was used to cast the column specimen [66]. This strength value was adopted in the AFC concrete model [63] for the response simulation of the test specimen. In this work, both the steel rebar and concrete are modelled as meshfree nodes and 257207 nodes are used in total to model half of the specimen due to symmetry.

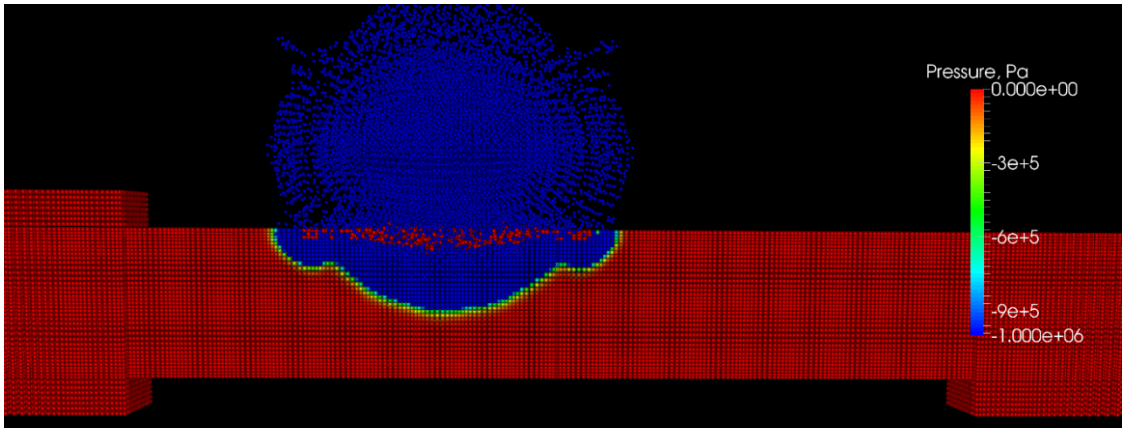

(a)Time: 0.08 msec

Figure 5.14. Pressure contours at different time, (a) time: 0.08 msec, (b) time: 0.12 msec, (c) time: 0.16 msec.

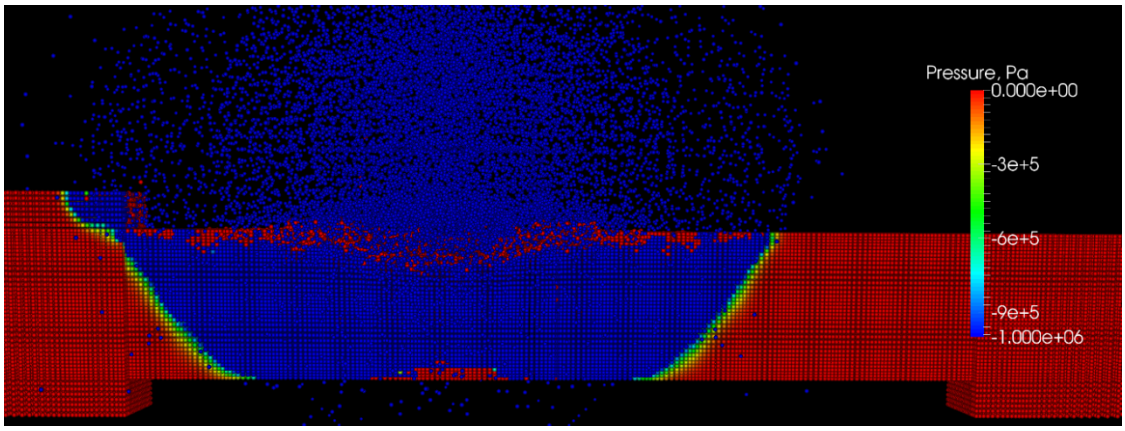

(b)Time: 0.12 msec

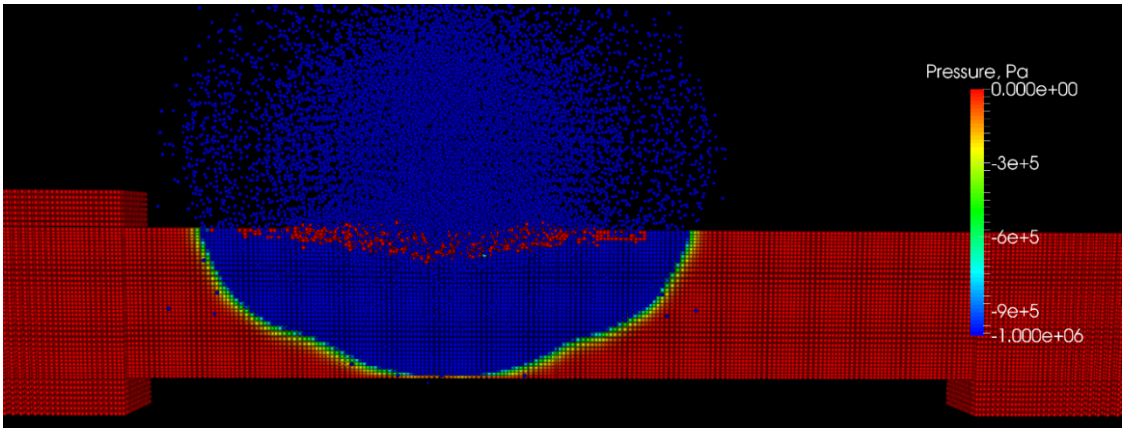

(c)Time: 0.16 msec

Figure 5.14. Pressure contours at different time, (a) time: 0.08 msec, (b) time: 0.12 msec, (c) time: 0.16 msec.(Continued)

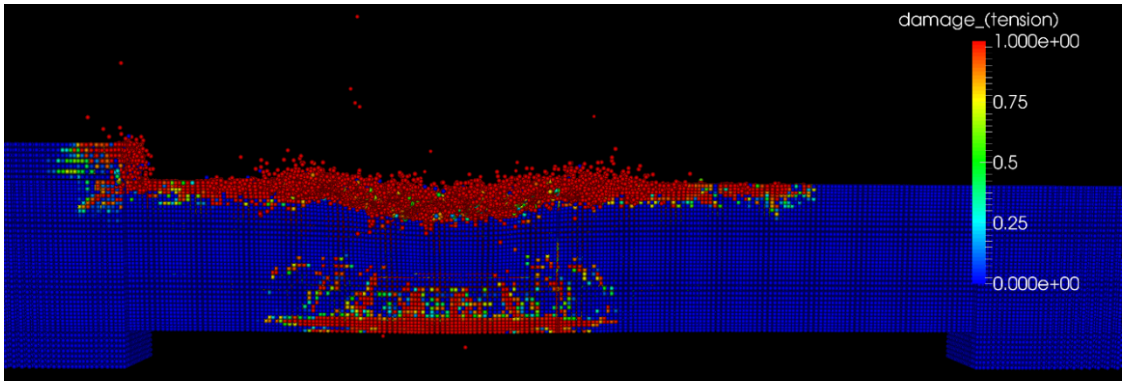

Figure 5.15. Tensile damage contour at time: 0.20 msec.

Some of the snapshots for pressure contours are listed in Figure 5.14: (a) shows the shock wave is clearly imparted from the explosive gas into the concrete column through the proposed FSI algorithm; (b) shows the shock wave reaches the free surface and afterwards it is reflected and turns into a tensile wave at the bottom as shown in (c). The tensile damage at time 0.2 msec is shown in Figure 5.15. At the bottom of the figure, we can see there is a tensile damage band indicating that spalling is occurring as a result of the reflected tensile wave. On the other hand, there are several tensile bands along the transverse direction which may be caused by the local bending effect. In the experiment setup, there were some sensors placed on the column meant to record the pressure and displacement histories, but unfortunately they were all destroyed by the powerful impact of the explosive gas. In the end, only the damaged profiles are compared in Figure 5.16, where we can see the damaged zone length, 1200 mm predicted by the numerical simulation agrees well with the experimental result.

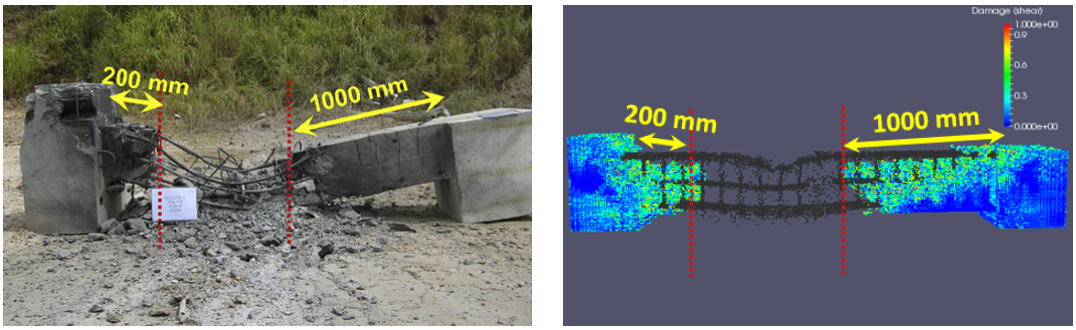

(a) (b)

Figure 5.16. RC column specimen (a) explosive test (adapted from [66]), (b) numerical result.

5.6 CONCLUSION

A semi-Lagrangian RKPM framework is proposed to model transient dynamic failure of concrete structures subjected to blast loadings in this chapter. The strong shocks in both fluid and solid are modeled by embedding Godunov flux into the semi-Lagrangian RKPM formulation. This formulation was shown effective for modeling shock-induced fragmentations. The fragmentations from concrete structure make the fluid-solid interaction challenging to be modelled due to the surface cracking and countless new surface generation. In this framework, fluid-structure interaction involving material fragmentations is effectively addressed by the level set enhanced natural kernel contact algorithm.

In this framework an approach is proposed to derive a consistent shock Hugoniot (required by Riemann solver) from the AFC concrete material model with microcrack-informed damage considered. This approach has been validated by solving the benchmark problem and it is applicable to other concrete material models.

A reinforced concrete column subjected to the blast loading is modeled to demonstrate the effectiveness of the proposed framework. The numerical results show that the key failure mechanisms are well captured and they are in good agreement with the experimental data.

ACKNOWLEDGENTS

This Chapter 5 is currently being prepared for submission for publication of the material. J.S. Chen, G. Zhou, ‘A Semi-Lagrangian Reproducing Kernel Particle Method

Framework for Modeling Transient Dynamic Failure of Concrete Structures Subjected to Blast Loadings'. The dissertation author was the primary investigator of this material.

Chapter 6

Numerical Modeling of Explosive Welding Using Semi-Lagrangian Reproducing Kernel Particle Method

6.1 INTRODUCTION

Explosive welding (see Figure 1.2 and Figure 6.1) is well known as an effective technique to directly join a wide variety of both similar and dissimilar combinations of metals that cannot be joined by any other welding or bonding methods due to their dramatically different melting points. Furthermore, this approach is capable to bond these metals over large surface area because the explosive can be distributed over any welding zone in an economical fashion. In explosive welding, the flyer plate is propelled by the high pressure from high explosive detonation and gains sufficient energy to form the welding. The flyer plate can also be accelerated by firing a gun and impact the base plate to form the same welding, which is the so-called impact welding [68].

During the high velocity oblique collision of metal plates, a jet can form in front of the collision point provided the collision angle β and collision velocity v_p are in an appropriate combination (see Figure 6.1(b)). Based on the experimental evidence it is generally accepted that the formation of a jet is detrimental for a successful welding [68]. The jet chemically clean the mating surfaces by sweeping away the non-metalic films (such as oxide films) and other contaminants, and therefore enable for the new exposed atoms of two materials to approach close enough to form a bond [68]. On the other hand, given certain processing parameters, a distinct wavy morphology can be observed at the interface of the two bonded materials (see Figure 6.2). The specific mechanism for this wavy patterning is not clearly understood yet. Some researches claim that localized melting and solidification at the interface occurs [69] is the key reason, while others believe it is due to the high interfacial shear-rate deformation [70] or a shear plastic flow instability between the two impacting materials [71]. There is no agreement on whether the wavy interface is necessary to achieve a strong bond. In [72, 73], the authors believe that the formation of

wavy morphology indicates a successful welding and is necessary for obtaining the optimum weld strength and mechanical interlocking, while others claim a high-quality weld can be achieved even if the interface is straight [74]. In this study, a wavy interface is not treated as an indicator for a successful welding and instead a jet formation is considered as a crucial sign of a high-quality weld.

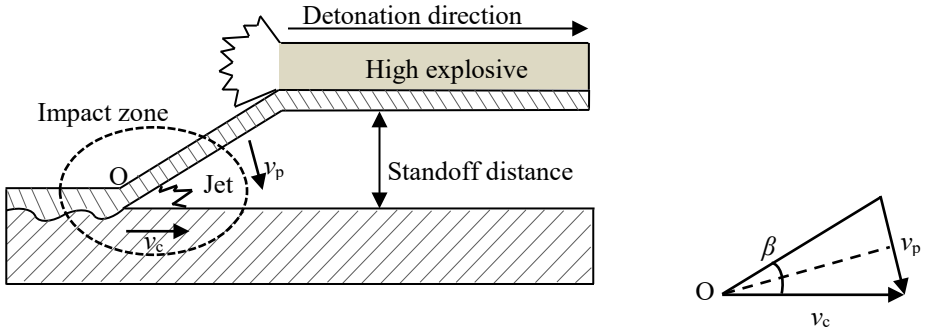

(a) (b)

Figure 6.1. (a) Explosive welding process; (b) geometrical analysis.

There are some simulation results reported in other publications. Grigonon *et al* [75] modeled the explosive welding of aluminum to aluminum using RAVEN, a 2D explicit Eulerian finite difference code. The jetting is shown in the simulation, but the resolution is relatively low which is expected for an Eulerian formulation. In Eulerian description, the interface is smeared out and a tracking technique is required. Nassiri *et al* [76] performed an arbitrary Lagrangian-Eulerian (ALE) finite element simulation on an impact welding process and however the jetting is not produced. Fragmentations (jetting) are very difficult to model for conventional Lagrangian or ALE mesh-based methods such as FEMs, finite difference methods and isogeometric analysis (IGA). Among meshfree methods, Wang *et al* [77] modeled the explosive welding by using material point method (MPM) and however it fails to reproduce the jetting. The smoothed-particle hydrodynamics (SPH) has been

applied for modelling the impact welding process [78] and the jetting is well captured. However, tensile instability, undesired numerical fracture [79, 80], inaccurate gradient estimate for stress calculation [39] and lack of linear consistency, and the existence of zero-energy modes [39] are the common difficulties in SPH methods that require additional treatments and modifications.

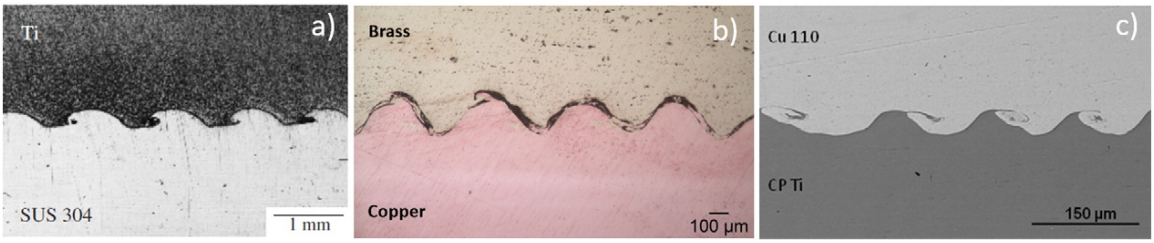

Figure 6.2. Wavy morphology at the weld interface, (a) Ti-Stainless steel [81]; (b) Brass-Copper [76]; (c) Cu-CP Ti [82].

Key physics in explosive welding to be captured in numerical modeling includes, the strong shock waves in fluid (explosive gas and air) and solid (metal plates), fluid-structure interaction (FSI), contact between the flyer plate and base plate, and the material fragmentation (jetting), which is essentially the same as in the reinforced concrete column subjected to blast loading problem discussed in Chapter 5. And thus the developed framework is adopted in this chapter to model the explosive/impact welding process.

This chapter is organized as follows. In section 2, an impact welding is first simulated and analyzed to show the wavy interface and jetting can be well captured by using semi-Lagrangian RKPM. In section 3, an explosive welding is modeled and discussed to show the effectiveness of this framework, and followed by conclusions in section 4.

6.2 IMPACT WELDING MODELING

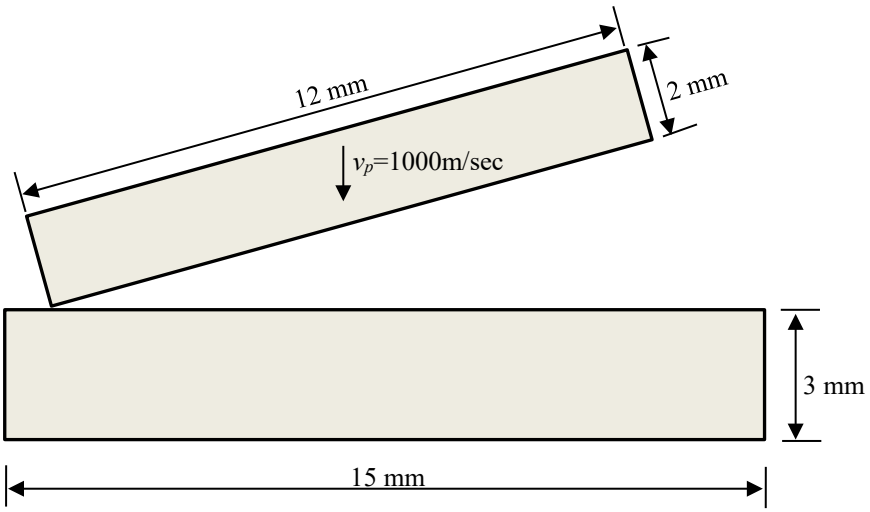

Figure 6.3. Schematic of impact welding.

Numerically, impact welding only involves two impacting solid metal plates and the key physics to be modelled consists of shock wave propagation in solid, contact at the collision interface and material fragmentations (jetting). Compared with the explosive welding, the compressible fluid (air and explosive gas) and FSI are not required here. In order to show this framework is capable to reproduce the wavy interface and jetting, an impact welding example is first simulated in this section. Furthermore, the collision angle β remains constant in this case, which makes the following analysis more focused. Wavy interfacial morphology and jetting only occur under certain combination of impact velocity v_p and collision angle β (see Figure 6.1 (b)). However, so far there does not exist a generic and specific description of the combination. In this study, we believe two conditions must be fulfilled. First, the impact velocity must be high enough to provide sufficient energy to drive the material at the interface yield and then fluid-like behaviors, wavy interface and jetting are possible to occur. However, the impact velocity should be limited such that the

collision velocity v_c (see Figure 6.1(b)) is less than the sound speed of the solid material, which is the second condition. As known, the wavelets generated by impacting at colliding point O involves *P* wave and *S* wave (S wave runs faster than *P* wave). These wavelets must travel faster than the speed of the closure of the colliding surfaces, i.e. collision velocity v_c, in order to spall the material to form jetting ahead of the colliding point O. Therefore, the second condition (i.e. $v_c < C_S$, C_S is the lower sound speed of the two mating materials) should hold. Based on the geometric relationship shown in Figure 6.1(b), the collision velocity can be derived,

$$v_c = \frac{v_p}{2\sin(\beta/2)}. \tag{6.1}$$

Considering the two conditions, given the collision angle β, v_p can be chosen as high as possible within the range $v_c = v_p/(2\sin(\beta/2)) < C_S$. For example, if we choose both the flyer and base plates to be 6061 T0 aluminum alloy with the sound speed C_S, 5356 m/sec, for a given collision angle β = 20º, v_p should be set less than $2\sin(\beta/2)C_S = 1860$ m/sec. In this study, within the valid region ($v_c = v_p/(2\sin(\beta/2)) < C_S$), the case v_p = 1000 m/sec in the vertical direction is selected to be modeled and the problem setup is shown in Figure 6.3. 178158 nodes are used to discretize the model. The contact between the two impacting plates are addressed by the level set enhanced natural kernel contact (LSENKC) algorithm [44]. A modified Johnson-Cook constitutive model [83] and failure criterion [84] (the details are given in Appendix A at the end of this chapter) are used for the 6061 T0 aluminum alloy and the parameters are listed in Table 6.1. The following is the discussion and analysis on the simulation results.

Table 6.1. Material constants for the 6061 T0 aluminum alloy (modified Johnson-Cook model).

Young's modulus E	69 GPa
Poisson's ratio υ	0.33
Density ρ	2700 kg/m^3
Specific heat capacity C_p	900 J/kgK
Reference temperature T_r	293K
Initial temperature T_0	293K
Melting temperature T_m	926K
Temperature softening coefficient m	1.0
Taylor–Quinney constant χ	0.9
Yield stress A	60MPa
Strain hardening B	500MPa
Strain hardening exponent n	0.3
Strain rate hardening C	0.02
Reference strain rate ε_0	5.0×10^{-4} s^{-1}
Fracture strain coefficients D_1	0.18
D_2	1.936
D_3	-2.964
D_4	-0.014
D_5	1.014

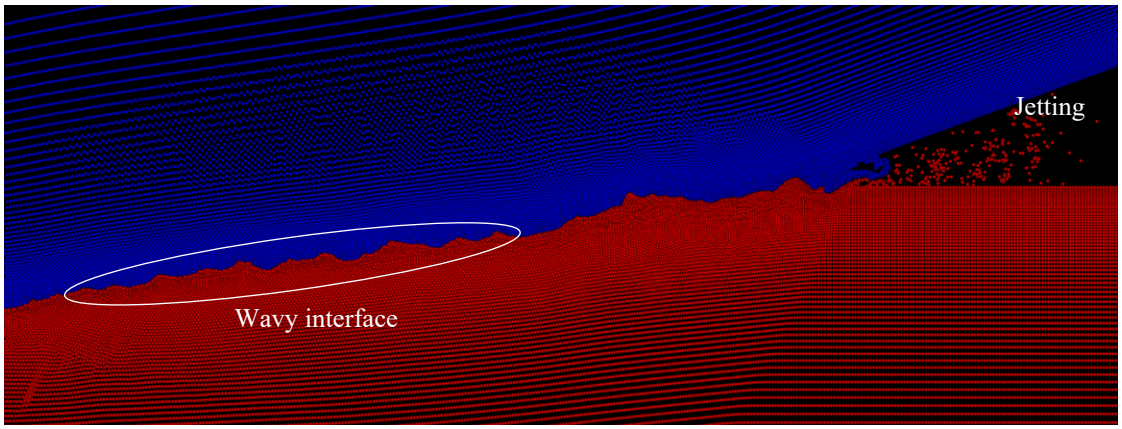

Figure 6.4. Wavy interface and jet formation at time 2.2 μsec.

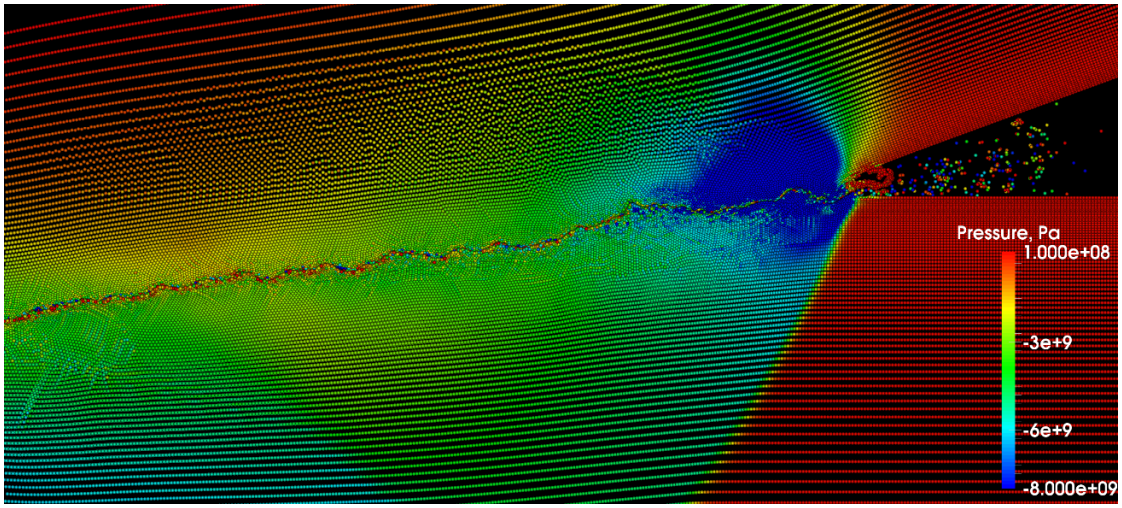

Figure 6.5. Pressure distribution at time 2.2 μsec.

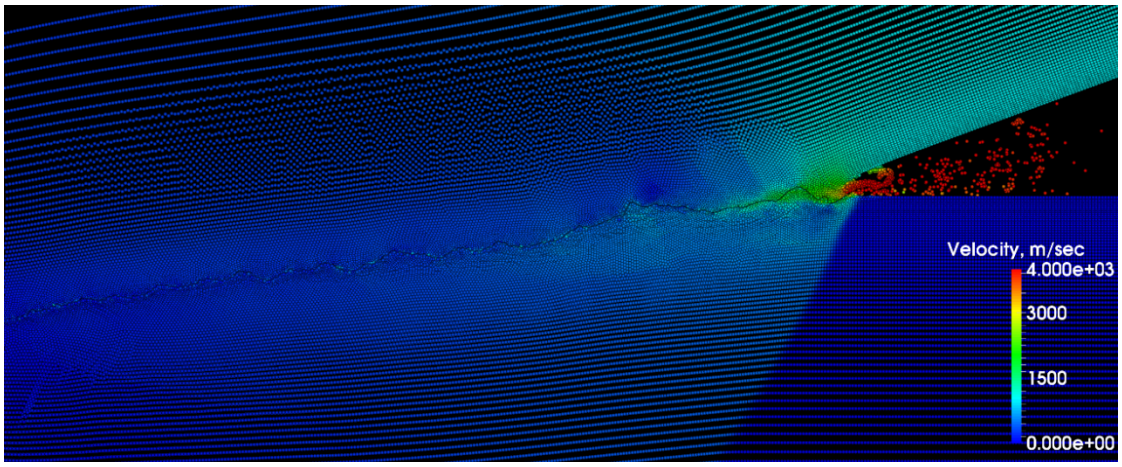

Figure 6.6. Velocity distribution at time 2.2 μsec.

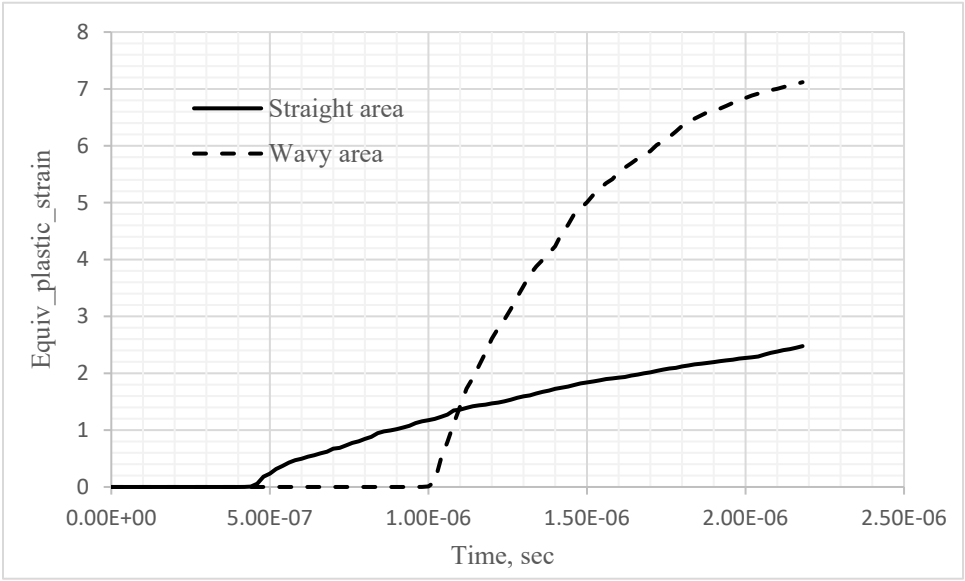

Figure 6.7. Equivalent plastic strain evolution at straight and wavy areas.

6.2.1 Temperature

At the interface, the peak temperature is about 700 K which is far lower than the melting point 900 K. This result confirms that impact welding is a solid state welding process.

6.2.2 Jet formation

Jetting is believed as a prerequisite for a successful welding. In this simulation, jetting starts at time 0.6 μsec and the one at time 2.2 μsec is shown in Figure 6.4. As shown, the phenomenon of jetting is reproduced very well by using the semi-Lagrangian RKPM formulation. Near the collision point, the pressure gradient is very high (see Figure 6.5), which drives the material to have large plastic deformation. As a result the zone also has the highest velocity (see Figure 6.6) and the jetting is also formed in the zone. Simply speaking, the high pressure gradient due to the impact at the collision point is the driving force of jetting. The jet velocity obtained from the simulation is about 4480 m/sec. It is 16% lower than the standard equation [85] $v_j = [v_p/\sin(\beta)](1+\cos(\beta)) = 5237$ m/sec, which is derived based on the jet formation in fluid mechanics. Therefore this equation are only used in the literature (such as [78, 68]) as a rough estimation since pure fluid assumption is not realistic for solid plate impacting problem and its correctness has not been proved. And in [78, 68], the error 10-15%, 15-20% are reported respectively. The jet velocity herein actually agrees reasonably with the estimation and is in good agreement with results in [78, 68].

6.2.3 Straight and wavy interface

The transition from a straight to a wavy interface is observed in this simulation as shown in Figure 6.4. There are some hypotheses on the mechanism of the wavy interface and it is still an open research area. However, based on the numerical experience in [78, 68] and also in this simulation, the plastic strain must be high enough in order to form the

wavy interface. The equivalent plastic strain at the straight region is less than at the wavy interface (see Figure 6.7), which is consistent with the conclusion in [78, 68]. One reasonable explanation is that the higher the plastic deformation level, the more the material behaves like fluid where wavy interface can form as a result of physical instability.

6.3 EXPLOSIVE WELDING MODELING

In section 2, it shows this framework is capable to model the key phenomena, jetting and wavy interface in impact welding. In this section, an explosive welding case is simulated and the compressible fluid (air and explosive gas) and FSI are included compared with impact welding case.

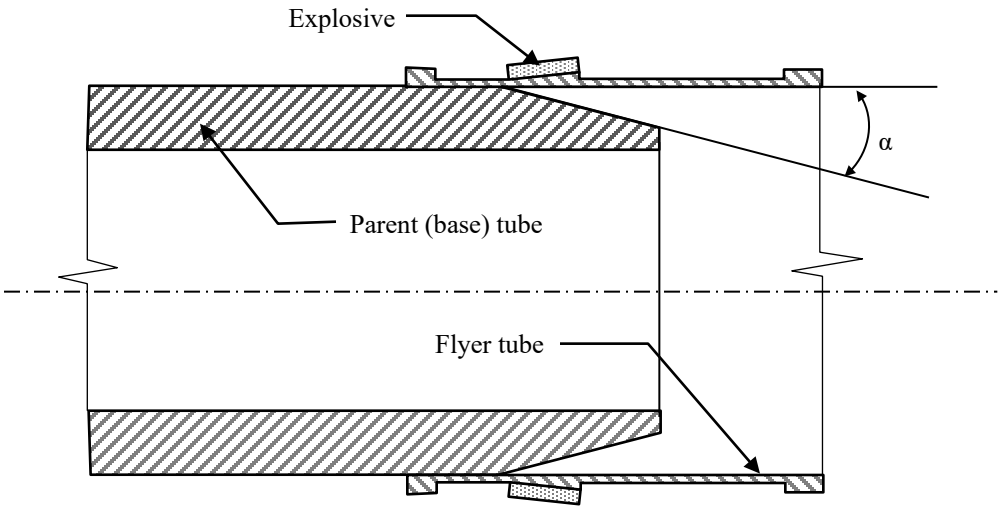

Figure 6.8. Configuration used in explosive welding of capsule.

In Figure 6.8, it shows the proposed capsule used in Mars Sample Return Mission [75]. After the initiation of the explosive, the flyer tube is accelerated and impacts the parent tube, which enables the hermetic seal of the capsule. The explosive is initiated from

a point and the resulted detonation follows a circular pattern with two fronts. In this case, the axial collapse, instead of the radial one is responsible for the welding [75]. The problem can be reduced to a 2D problem [75]. A PETN-based plastic explosive was used with a linear density of 4.25 g/m. The initial angle between the two tubes is denoted as α. In [75], it models multiple cases with the initial angles varying from 4º to 14º. Since the parametric study is not the main point of this work, for validation purpose, only the case with angle 9.46º where the jetting is formed, is recomputed in this section and compared with the original simulation result in [75] which is obtained by using RAVEN code, a 2D explicit Eulerian finite difference code.

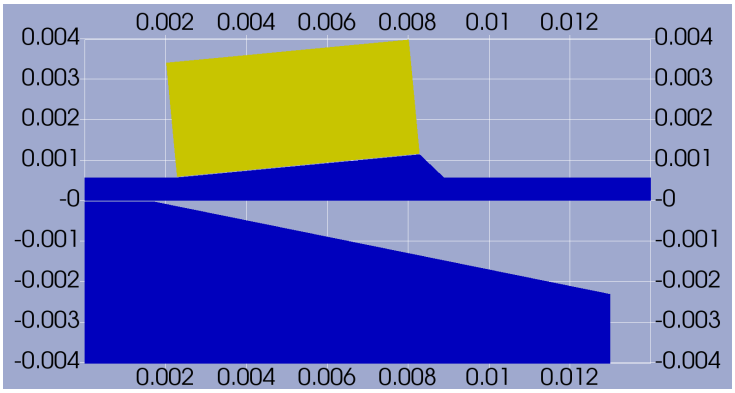

Figure 6.9. 2D section used for the computation (dimensions in meter); yellow: explosive; blue: flyer and base plates; gray: air.

The representative 2D configuration is shown in Figure 6.9. According to [67], for contact detonation case (i.e. the standoff distance is zero), the shock wave in the explosive gas is dominant and the effect of air is small enough to be neglected. For the sake of simplicity and saving computational cost, the air is not modeled in this simulation. PETN-based plastic explosive is modeled by the following equation of state $P = (\gamma - 1)\rho \mathrm{e}$ where γ is taken as 3 for the high explosives gas [61]. Here the chemical reaction of the explosive is not modeled. Instead, an empirical burn function is used as described in section 5.2.

Again, the modified Johnson-Cook constitutive model [83] and failure criterion [84] are used for the 6061 T0 aluminum alloy and the parameters are specified in Table 6.1. The contact between the two impacting plates and FSI are addressed by the level set enhanced natural kernel contact (LSENKC) algorithm [44]. 324364 nodes are used to discretize the explosive, flyer and base plates.

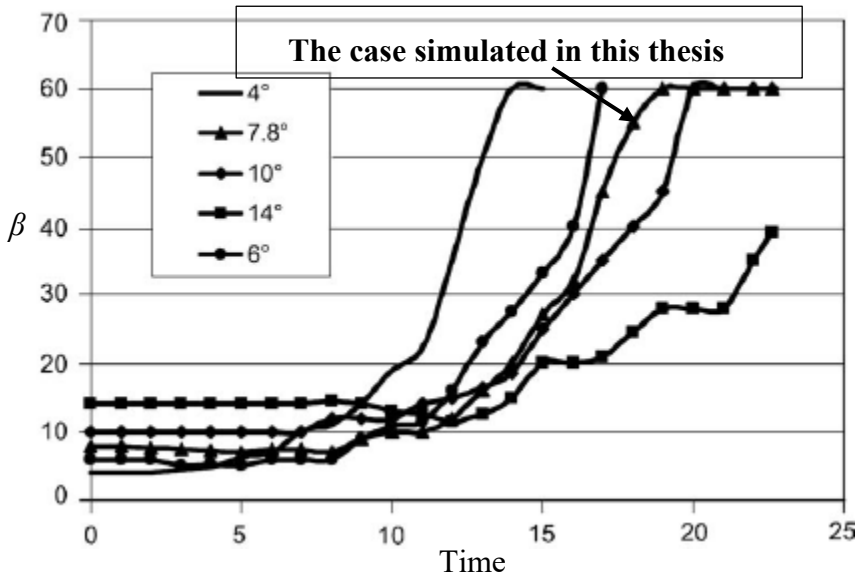

Figure 6.10. Evolution of impact angle β in the simulation of original paper (adapted from [75]).

Different from the impact welding case where the impact angle β and velocity v_p are close to constant, herein they are dynamically changing as a function of time, as shown in Figure 6.11 and Figure 6.12. The impact angle arrives at a stable value (about 60º), which is consistent with the original simulation as shown in Figure 6.10 (the curve with angle 10º). This is due to that it takes time to gradually impart the energy from the explosive gas to the flyer plate through FSI. Impact angle β increases with time, which can also be seen in Figure 6.13. Impact velocity v_p also grows with time and reaches a stable value, about 1000 m/sec. As mentioned earlier, jetting occurs only under certain combination of β and

v_p. Based on the two conditions discussed in section 2, when the impact velocity increases to 1000 m/sec, β must be big enough such that $\sin(\beta/2) > v_p/(2C_s)$ holds and the jetting is expected to form. Obviously, $\beta > 20^o$ is a valid option, since v_p =1000 m/sec and $\beta = 20^o$ are used in section 2 and jetting is formed. As shown in Figure 6.11, $\beta = 20^o$ is achieved at time around t = 1.5 μsec and after some accumulation of the plastic deformation, jetting is first observed at time 2.2 μsec. Here it takes about 0.7 μsec (= 2.2 μsec-1.5 μsec) to accumulate enough plastic deformation, which is consistent with the jetting time in impact welding case in the last section where it takes about 0.6 μsec (because the jetting first occurs at t = 0.6 μsec with a constant $\beta = 20^o$). In [75], it reports that the jetting starts at time 2.5 μse, which is close to our result 2.2 μsec. The progress of jetting is shown in Figure 6.13. As can be seen, the overall deformed configuration is very similar to the original simulation (see Figure 6.14). The jetting is modeled very well and it is better represented than that in [75] by comparing Figure 6.13 with Figure 6.14.

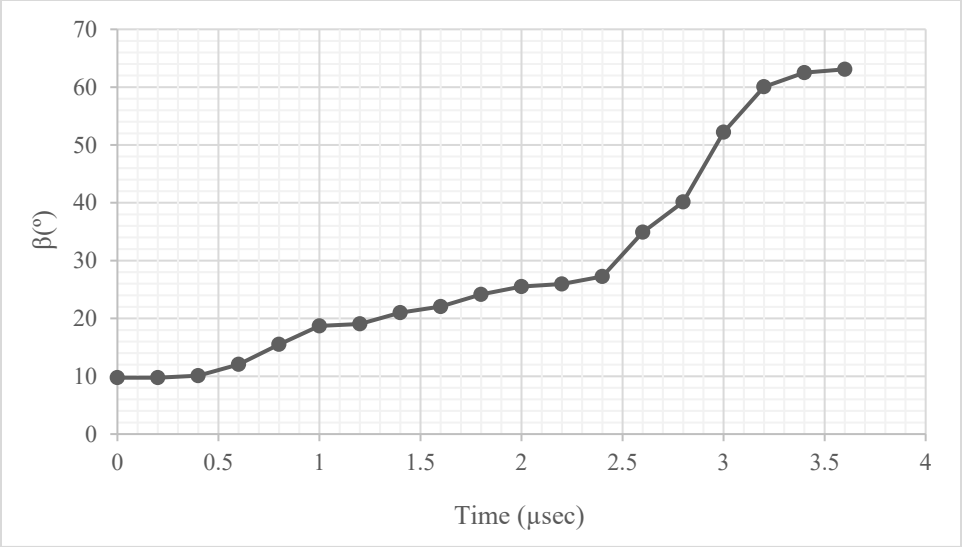

Figure 6.11. Evolution of impact angle β.

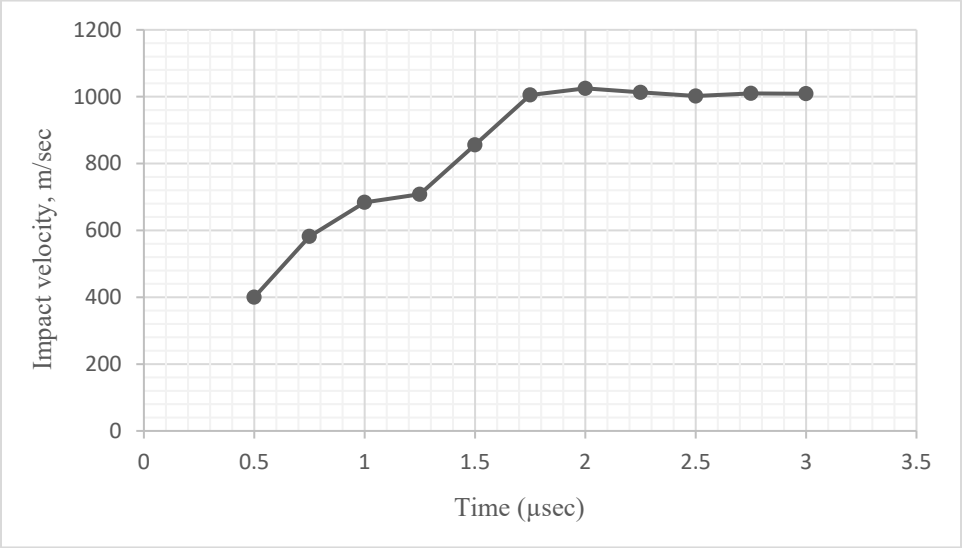

Figure 6.12. Evolution of impact velocity at the collision point.

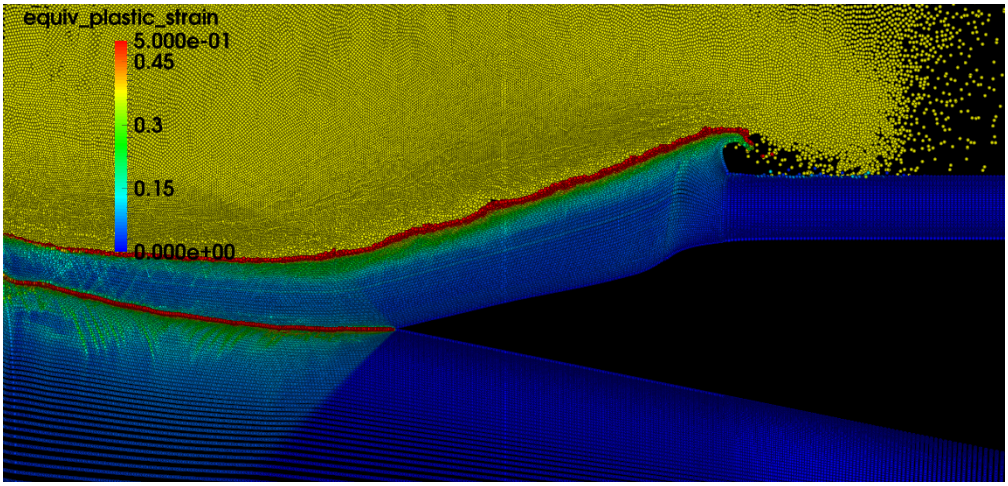

(a)

Figure 6.13. Numerical simulation of the explosive welding process: jetting formation (a) time t = 2.0 µsec, (b) time t = 3.0 µsec, (c) time t = 3.5 µsec.

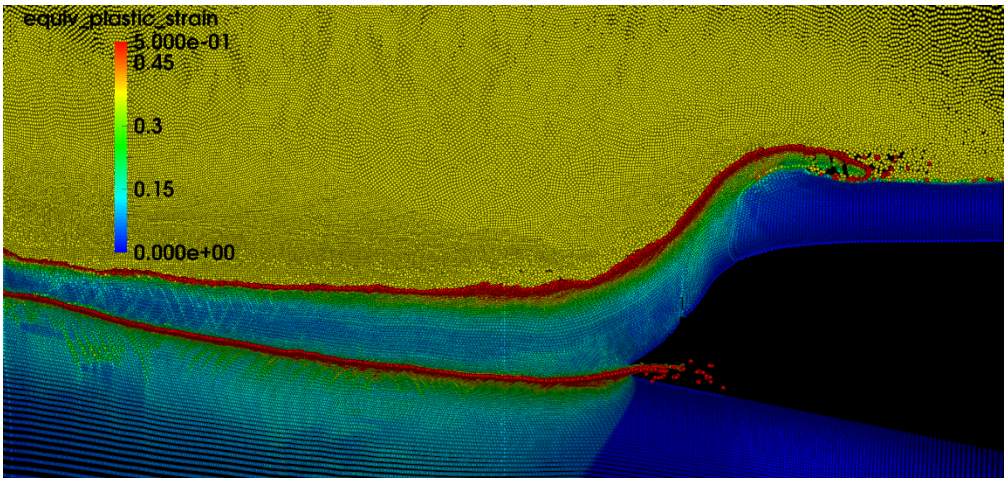

(b)

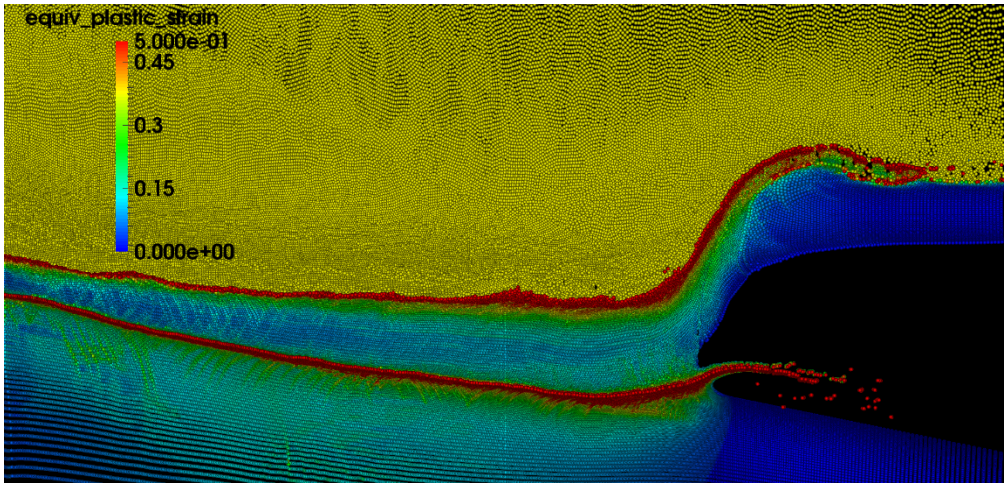

(c)

Figure 6.13. Numerical simulation of the explosive welding process: jetting formation (a) time t = 2.0 μsec, (b) time t = 3.0 μsec, (c) time t = 3.5 μsec. (Continued)

In Figure 6.13, we can see a narrow zone with high plastic strain at the impacting plate interface and FSI interface, which is due to the high shear stresses at these interfaces. The wavy interface is not obvious in this simulation, which is in agreement with the numerical result in [75] as shown in Figure 6.14.

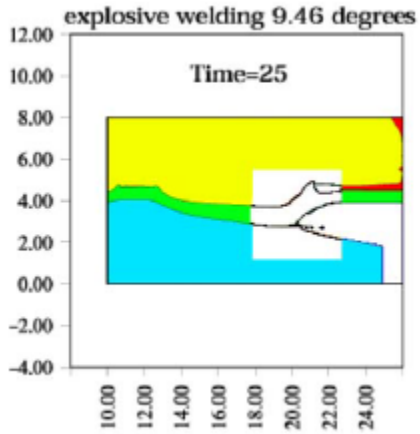

Figure 6.14. Jetting formation in the original paper (adapted from [75]).

6.4 CONCLUSION

In this chapter, the semi-Lagrangian RKPM framework discussed in chapter 5 is applied to model the explosive/impact welding process. An impact welding process is first modelled and analyzed, and the wavy interface and the jetting are well reproduced. The simulated jet velocity is consistent with the theoretical prediction and other publications. Finally, the explosive welding case, the capsule used in Mars Sample Return Mission [75] is recalculated and compared with the original simulation results. The dynamic changing of the impact angle, the forming of jetting are in agreement with the results in [75] and the jet formation is better represented in term of resolution.

This framework is shown well suited for modelling explosive/impact welding processes and is promising to be applied to design the parameters of the experiment in the future.

APPENDIX A: MODIFIED JOHNSON-COOK MATERIAL MODEL AND FAILURE CRITERION

The modified Johnson-Cook constitutive model [83] and failure criterion [84] are used to describe all the metals in this chapter. In the modified Johnson-Cook model, the equivalent stress is defined as

$$\sigma_{eq} = \left(A + B\overline{\varepsilon}^{n}\right)\left(1+\dot{\varepsilon}^{*}\right)^{C}\left(1-T^{*m}\right), \tag{6.2}$$

Where $\overline{\varepsilon}$ is the equivalent plastic strain and $\dot{\varepsilon}^{*} = \dot{\overline{\varepsilon}} / \dot{\varepsilon}_0$ represents the plastic strain rate normalized by a reference strain rate at which experiments were conducted to obtain the material properties. The normalized temperature $T^{*} = \left(T - T_r\right)/\left(T_m - T_r\right)$ is utilized to characterize thermal softening caused by adiabatic hearting due to the plastic work and T_r is the reference temperature, T_m is the melting temperature. Damage accumulation is expressed as

$$D = \sum \frac{\Delta\overline{\varepsilon}}{\varepsilon_f}, \tag{6.3}$$

where ε_f is the failure strain,

$$\varepsilon_f = \left[D_1 + D_2 e^{D_3\sigma^{*}}\right] + \left[1+\dot{\varepsilon}^{*}\right]^{D_4}\left[1 + D_5 T^{*m}\right], \tag{6.4}$$

where D_1-D_5 are five given material constants and the pressure-stress ratio σ^{*} is given by

$$\sigma^{*} = \frac{\sigma_{xx} + \sigma_{yy} + \sigma_{zz}}{3\sigma_{eq}}. \tag{6.5}$$

ACKNOWLEDGEMENTS

Chapter 6 is currently being prepared for submission for publication of the material. J.S. Chen, G. Zhou, 'Numerical Modeling of Explosive/impact Welding using Semi-Lagrangian Reproducing Kernel Particle Method'. The dissertation author was the primary investigator of this material.

Chapter 7

Conclusions

7.1 SUMMARY OF THE RESEARCH PERFORMED AND THE NOVEL CONTRIBUTIONS

In this dissertation, an RKPM based computational framework is developed to model two types of blast events, the transient dynamic failure of reinforced concrete column subjected to blast loading and explosive/impact welding processes, which involve strong shock waves in both fluid and solid, fluid-structure interaction (FSI), high strain rate phenomenon, material damage and fragmentations, multi-body contact. The main contributions of this study are summarized as following.

In this study, two hydrodynamic formulations are proposed under RKPM framework with physics-based shock modeling techniques. Essential shock physics is considered by introducing Godunov flux into RKPM and oscillation control is achieved by a gradient smoothing in pressure and velocity gradients. In particular, the second formulation is applicable to problems with shock-induced fragmentations, which is challenging for existing methods. A variety of benchmark problems are examed for these two formulations and the results agree well with reference solutions.

Another difficulty in blast modeling comes from FSI which involves the surface cracking and new surface generation in structures when fragmentations occur. In this work, the level set enhanced natural kernel contact (LSENKC) algorithm is adopted to address FSI with both solid and fluid fields discretized by Lagrangian particles. This contact algorithm does not require the definition of potential contact surfaces *a priori* and is effective for FSI involving fragmentations.

Finally, by combining the new developed RKPM hydrodynamic formulation (for strong shock waves in both solid and fluid) and the LSENKC contact algorithm (for FSI with fragmentation), the proposed computational framework is applied to model the

transient dynamic failure of reinforced concrete column subjected to blast loading and the explosive/impact welding processes with satisfactory results.

7.2 RECOMMENDATIONS FOR FUTURE STUDIES

Based on the research experience gained in this dissertation, directions for future research are recommended as follows:

- This framework can be further applied to simulate marine structures subjected to underwater explosion and soil structures subjected to the buried charge explosion, which share the key features with the two comprehensive problems modelled in Chapter 5 and 6 and are frequently encountered in defense.
- In the simulation of explosive/impact welding, prediction of meso-scale material properties is critical in determining the weld bond strength. In this work, only continuum scale is considered and microstructure effects are not investigated.
- Adaptive refinement in RKPM can be implemented to further improve the efficiency and accuracy of this framework.

Bibliography

[1] Belytschko, T., Lu, Y.Y. and Gu, L., "Element-free Galerkin methods," *International journal for numerical methods in engineering,* vol. 37, no. 2, pp. 229-256, 1994.

[2] Liu, W. K., Jun, S. and Zhang, Y. F., "Reproducing Kernel Particle Methods," *International Journal for Numerical Methods in Fluids,* vol. 20, no. 8, pp. 1081-1106, 1995.

[3] Monaghan, J.J., "Smoothed particle hydrodynamics," *Annual review of astronomy and astrophysics,* vol. 30, pp. 543-574, 1992.

[4] Guan, P. C., Chi, S.W., Chen, J.S., Slawson, T.R., and Roth, M.J., "Semi-Lagrangian reproducing kernel particle method for fragment-impact problems," *International Journal of Impact Engineering,* vol. 38, no. 12, pp. 1033-1047, 2011.

[5] Guan, P.C., Chen, J.S., Wu, Y., Teng, H., Gaidos, J., Hofstetter, K, and Alsaleh, M., "Semi-Lagrangian reproducing kernel formulation and application to modeling earth moving operations," *Mechanics of Materials,* vol. 41, no. 6, pp. 670-683, 2009.

[6] Kuhl, E., Hulshoff, S. and De Borst, R., "An arbitrary Lagrangian Eulerian finite-element approach for fluid–structure interaction phenomena," *International journal for numerical methods in engineering,* vol. 57, no. 1, pp. 117-142, 2003.

[7] Donea, J., Giuliani, S. and Halleux, J.P., "An arbitrary Lagrangian-Eulerian finite element method for transient dynamic fluid-structure interactions," *Computer methods in applied mechanics and engineering,* vol. 33, no. 1-3, pp. 689-723, 1982.

[8] Legay, A., Chessa, J. and Belytschko, T., "An Eulerian–Lagrangian method for fluid–structure interaction based on level sets," *Computer Methods in Applied Mechanics and Engineering,* vol. 195, no. 17, pp. 2070-2087, 2006.

[9] von Neumann, J., and Richtmyer, R.D., "A method for the numerical calculation of hydrodynamic shocks," *Journal of applied physics,* vol. 21, no. 3, pp. 232-237, 1950.

[10] Godunov, S.K., "Finite difference method for numerical computation of discontinuous solutions of the equations of fluid dynamics," *Math. Sbornik, translated US Joint Publ. Rel. Service, JPRS,* vol. 47, pp. 271-306, 1969.

[11] Benson, D.J., "Computational methods in Lagrangian and Eulerian hydrocodes.," *Computer methods in Applied mechanics and Engineering,* vol. 99, no. 2, pp. 235-394, 1992.

[12] Dobrev, V.A., Ellis, T.E., Kolev, T.V., and Rieben, R.N., "Curvilinear finite elements for Lagrangian hydrodynamics," *International Journal for Numerical Methods in Fluids,* vol. 65, no. 11, pp. 1295-1310, 2011.

[13] Kolev, T.V. and Rieben, R.N., "A tensor artificial viscosity using a finite element approach," *Journal of Computational Physics,* vol. 228, no. 22, pp. 8336-8366, 2009.

[14] Benson, D.J. and Schoenfeld, S., "A total variation diminishing shock viscosity," *Computational mechanics,* vol. 11, no. 2, pp. 107-121, 1993.

[15] Campbell, J.C. and Shashkov, M.J., "A tensor artificial viscosity using a mimetic finite difference algorithm," *Journal of Computational Physics,* vol. 172, no. 2, pp. 739-765, 2001.

[16] Dobrev, V.A., Kolev, T.V., and Rieben, R.N., "High-order curvilinear finite element methods for Lagrangian hydrodynamics," *SIAM Journal on Scientific Computing,* vol. 34, no. 5, pp. 606-641, 2012.

[17] Bazilevs, Y., Akkerman, I., Benson, D.J., Scovazzi, G. and Shashkov, M.J., "Isogeometric analysis of lagrangian hydrodynamics," *Journal of Computational Physics,* pp. 224-243, 2013.

[18] Monaghan, J.J. and Gingold, R.A., "Shock simulation by the particle method SPH," *Journal of computational physics,* vol. 52, no. 2, pp. 374-389, 1983.

[19] van Leer, B., "Towards the ultimate conservative difference scheme. IV. A new approach to numerical convection," *Journal of computational physics,* vol. 23, no. 3, pp. 276-299, 1977.

[20] van Leer, B., "Towards the ultimate conservative difference scheme. V. A second-order sequel to Godunov's method," *Journal of computational Physics,* vol. 32, no. 1, pp. 101-136, 1979.

[21] Harten, A., Engquist, B., Osher, S. and Chakravarthy, S.R., "Uniformly high order accurate essentially non-oscillatory schemes, III.," in *In Upwind and High-Resolution Schemes*, Springer Berlin Heidelberg, 1987, pp. 218-290.

[22] Liu, X.D., Osher, S. and Chan, T., "Weighted essentially non-oscillatory schemes," *Journal of computational physics,* vol. 115, no. 1, pp. 200-212, 1994.

[23] Cha, S-H., and Whitworth, A.P., "Implementations and tests of Godunov-type particle hydrodynamics.," *Monthly Notices of the Royal Astronomical Society,* vol. 340, no. 1, pp. 73-90, 2003.

[24] Chiu, E.K., Wang Q., and Jameson, A., "A conservative meshless scheme: general order formulation and application to Euler equations," *AIAA,* vol. 49th Aerospace Sciences Meeting, pp. 2011-651, 2011.

[25] Hietel, D., Steiner, K., and Struckmeier, J., "A finite-volume particle method for compressible flows," *Mathematical Models and Methods in Applied Sciences,* vol. 10, no. 9, pp. 1363-1382, 2000.

[26] Inutsuka, S., "Reformulation of smoothed particle hydrodynamics with Riemann solvers," *Journal of Computational Physics,* vol. 179, p. 238, 2002.

[27] Junk, M., "Do finite volume methods need a mesh?," *Springer Berlin Heidelberg,* 2003.

[28] Löhner, R., Sacco, C., Oñate, E. Idelsohn, S., "A finite point method for compressible flow," *International Journal for Numerical Methods in Engineering,* vol. 53, no. 8, pp. 1765-1779, 2002.

[29] Ma, Z. H., Wang, H., and Qian, L., "A meshless method for compressible flows with the HLLC Riemann solver," *arXiv,* p. 1402.2690, 2014.

[30] Quinlan, N.J., and Nestor, R.M., "Fast exact evaluation of particle interaction vectors in the finite volume particle method," *Meshfree Methods for Partial Differential Equations V. Springer Berlin Heidelberg,* pp. 219-234, 2011.

[31] Hopkins, P. F., "A new class of accurate, mesh-free hydrodynamic simulation methods," *Monthly Notices of the Royal Astronomical Society,* vol. 450, no. 1, pp. 53-110, 2015.

[32] Luo, H., Baum, J.D. and Lohner, R., "Edge-based finite element scheme for the Euler equations," *AIAA journal,* vol. 32, no. 6, pp. 1183-1190, 1994.

[33] Hietel, D., and Keck, R., "Consistency by coefficient-correction in the finite-volume-particle method," *Meshfree Methods for Partial Differential Equations,* pp. 211-221, 2003.

[34] Roth, M.J., Chen, J.S., Danielson, K.T. and Slawson, T.R., "Hydrodynamic meshfree method for high-rate solid dynamics using a Rankine–Hugoniot enhancement in a Riemann-SCNI framework," *nternational Journal for Numerical Methods in Engineering,* 2016.

[35] Roth, M.J., Chen, J.S., Slawson, T.R. and Danielson, K.T., "Stable and flux-conserved meshfree formulation to model shocks," *Computational Mechanics,* vol. 57, no. 5, pp. 773-792, 2016.

[36] Chen, J.S., Pan, C.H., Wu, C.T. and Liu, W.K., "Reproducing kernel particle methods for large deformation analysis of non-linear structures," *Computer Methods in Applied Mechanics and Engineering,* vol. 139, no. 1, pp. 195-227, 1996.

[37] Chen, J.S., Wu, C.T., Yoon, S. and You, Y., "A stabilized conforming nodal integration for Galerkin mesh-free methods," *International Journal for Numerical Methods in Engineering,* vol. 50, no. 1, pp. 435-466, 2001.

[38] Belytschko, T. and Lin, J.I., "A three-dimensional impact-penetration algorithm with erosion," *Computers & structures,* vol. 251, no. 1, pp. 95-104, 1987.

[39] Randles, P.W. and Libersky, L.D., "Smoothed particle hydrodynamics: some recent improvements and applications," *Computer methods in applied mechanics and engineering,* vol. 139, no. 1, pp. 375-408, 1996.

[40] Potapov, S., Maurel, B., Combescure, A. and Fabis, J., "Modeling accidental-type fluid–structure interaction problems with the SPH method," *Computers & Structures,* vol. 88, no. 11, pp. 721-734, 2009.

[41] Rabczuk, T. and Eibl, J., "Simulation of high velocity concrete fragmentation using SPH/MLSPH," vol. 56, no. 10, pp. 1421-1444, 2003.

[42] Rabczuk, T. and Eibl, J., "Modelling dynamic failure of concrete with meshfree methods," *International Journal of Impact Engineering,* vol. 32, no. 11, pp. 1878-1897, 2006.

[43] Wu, Y., "A stabilized semi-Lagrangian Galerkin meshfree formulation for extremely large deformation analysis," *Phd Thesis, Advisor: Chen, J.S., University of California at Los Angeles,* 2005.

[44] Chi, S.W., Lee, C.H., Chen, J.S. and Guan, P.C., "A level set enhanced natural kernel contact algorithm for impact and penetration modeling," *International Journal for Numerical Methods in Engineering,* vol. 102, no. 3-4, pp. 839-866, 2015.

[45] Yreux, E. and Chen, J.S., "A quasi-linear reproducing kernel particle method," *International Journal for Numerical Methods in Engineering,* 2016.

[46] Hillman, M. and Chen, J.S., "An accelerated, convergent, and stable nodal integration in Galerkin meshfree methods for linear and nonlinear mechanics," *International Journal for Numerical Methods in Engineering,* 2015.

[47] Belytschko, T. and Kennedy, J.M., "Finite element approach to pressure wave attenuation by reactor fuel subassemblies," *J. Press. Technology,* pp. 172-177, 1975.

[48] Chen, J.S. and Wang, H.P., "New boundary condition treatments in meshfree computation of contact problems," *Computer Methods in Applied Mechanics and Engineering,* vol. 187, no. 3, pp. 441-468, 2000.

[49] Chen, J.S., Hillman, M., and Rüter, M., "An arbitrary order variationally consistent integration for Galerkin meshfree methods," *International Journal for Numerical Methods in Engineering,* vol. 95, no. 5, pp. 387-418, 2013.

[50] Cheng, J., and Shu, C.-W., "A high order ENO conservative Lagrangian type scheme for the compressible Euler equations," *Journal of Computational Physics,* vol. 277, no. 2, pp. 1567-1596, 2007.

[51] Dukowicz, J.K., "A general, non-iterative Riemann solver for Godunov's method," *Journal of Computational Physics,* vol. 61, no. 1, pp. 119-137, 1985.

[52] Chen, J.S., Yoon, S. and Wu, C.T., "Non-linear version of stabilized conforming nodal integration for Galerkin mesh-free methods.," *International Journal for Numerical Methods in Engineering,* vol. 53, no. 12, pp. 2587-2615, 2002.

[53] Sod, G.A, "A survey of several finite difference methods for systems of nonlinear hyperbolic conservation laws.," *Journal of computational physics,* vol. 27, no. 1, pp. 1-31, 1978.

[54] Noh, W.F., "Errors for calculations of strong shocks using an artificial viscosity and an artificial heat flux," *Journal of Computational Physics,* vol. 72, no. 1, pp. 78-120, 1987.

[55] Sedov, L.I., Similarity and dimensional methods in mechanics, CRC press, 1993.

[56] Dukowicz, J.K., and Meltz, B.J., "Vorticity errors in multidimensional Lagrangian codes," *Journal of Computational Physics,* vol. 99, no. 1, pp. 115-134, 1992.

[57] R. LeVeque, Finite volume methods for hyperbolic problems, Cambridge university press, 2002.

[58] Puso, M.A., Chen, J.S., Zywicz, E. and Elmer, W., "Meshfree and finite element nodal integration methods," *International Journal for Numerical Methods in Engineering,* vol. 74, no. 3, pp. 416-446, 2008.

[59] L. Davison, Fundamentals of shock wave propagation in solids, Berlin: Springer-Verlag, 2008.

[60] Marsh, S. A., "LASL Shock Hugoniot Data," University of California Press, Berkley, 1980.

[61] S. Zhang, Detonation and its applications, Beijing: Press of National Defense Industry, 1976.

[62] Liu, M.B., Liu, G.R., Zong, Z. and Lam, K.Y., "Computer simulation of high explosive explosion using smoothed particle hydrodynamics methodology," *Computers & Fluids,* vol. 32, no. 3, pp. 305-322, 2003.

[63] Adley, M., Frank, A., Danielson, K., Akers, S., and O'Daniel, J., "The Advanced Fundamental Concrete (AFC) Model," ERDC/GSL TR-10-51, 2010.

[64] Ren, X., Chen, J.S., Li, J., Slawson, T.R. and Roth, M.J., "Micro-cracks informed damage models for brittle solids," *International Journal of Solids and Structures,* vol. 48, no. 10, p. 1560–1571, 2011.

[65] Blom, Frederic J, "A monolithical fluid–structure interaction algorithm applied to the piston problem," *Computer methods in applied mechanics and engineering,* vol. 167, no. 3, pp. 369-391, 1998.

[66] Wu, K.C., Li, B. and Tsai, K.C., "Residual axial compression capacity of localized blast-damaged RC columns," *International journal of impact engineering,* vol. 38, no. 1, pp. 9-40, 2011.

[67] Kinney, G.F., "Engineering elements of explosion," Naval Weapon Center, China lake, California, November 1968.

[68] Mousavi, A.A. and Al-Hassani, S.T.S., "Numerical and experimental studies of the mechanism of the wavy interface formations in explosive/impact welding," *Journal of the Mechanics and Physics of Solids,* vol. 53, no. 11, pp. 2501-2528, 2005.

[69] Ben-Artzy, A., Stern, A., Frage, N. and Shribman, " Interface phenomena in aluminium–magnesium magnetic pulse welding," *Science and technology of welding and joining,* vol. 13, no. 4, pp. 402-408, 2008.

[70] Chemin, C. and Qingming, T., "Mechanism of wave formation at the interface in explosive welding," *Acta Mechanica Sinica,* vol. 5, no. 2, pp. 97-108, 1989.

[71] Nassiri, A., Chini, G. and Kinsey, B, "Spatial stability analysis of emergent wavy interfacial patterns in magnetic pulsed welding," *CIRP Annals-Manufacturing Technology,* vol. 63, no. 1, pp. 245-248, 2014.

[72] Vaidyanathan, P.V. and Ramanathan, A.R., "Design for quality explosive welding," *Journal of Materials Processing Technology,* vol. 32, no. 1, pp. 439-448, 1992.

[73] Balakrishna, H.K., Venkatesh, V.C. and Philip, P.K., " Influence of Collision Parameters on the Morphology of Interface in Aluminum-Steel Explosion Welds," *In Shock Waves and High-Strain-Rate Phenomena in Metals,* pp. 975-988, 1981.

[74] Kore, S.D., Vinod, P.N., Kumar, S. and Kulkarni, M.R., " Study of wavy interface in electromagnetic welds," *Trans Tech Publications,* vol. 504, pp. 729-734, 2012.

[75] Grignon, F., Benson, D., Vecchio, K.S. and Meyers, M.A., "Explosive welding of aluminum to aluminum: analysis, computations and experiments," *International Journal of Impact Engineering,* vol. 30, no. 10, pp. 1333-1351, 2004.

[76] Nassiri, A., Chini, G., Vivek, A., Daehn, G. and Kinsey, B., "Arbitrary Lagrangian–Eulerian finite element simulation and experimental investigation of wavy interfacial morphology during high velocity impact welding," *Materials & Design,* vol. 88, pp. 345-358, 2015.

[77] Wang, Y., Beom, H.G., Sun, M. and Lin, S., "Numerical simulation of explosive welding using the material point method," *International Journal of Impact Engineering,* vol. 38, no. 1, pp. 51-60, 2011.

[78] Wang, X., Zheng, Y., Liu, H., Shen, Z., Hu, Y., Li, W., Gao, Y. and Guo, C., "Numerical study of the mechanism of explosive/impact welding using smoothed particle hydrodynamics method," *Materials & Design,* vol. 35, pp. 210-219, 2012.

[79] Swegle, J. W., D. L. Hicks, and S. W. Attaway, "Smoothed particle hydrodynamics stability analysis," *Journal of computational physics,* vol. 116, no. 1, pp. 123-134, 1995.

[80] J. Monaghan, "SPH without a tensile instability," *Journal of Computational Physics,* vol. 159, no. 2, pp. 290-311, 2000.

[81] Manikandan, P., Hokamoto, K., Deribas, A.A., Raghukandan, K. and Tomoshige, R., "Explosive welding of titanium/stainless steel by controlling energetic conditions," *Materials transactions,* vol. 47, no. 8, pp. 2049-2055, 2006.

[82] Vivek, A., Hansen, S.R., Liu, B.C. and Daehn, G.S., "Vaporizing foil actuator: A tool for collision welding," *Journal of Materials Processing Technology,* vol. 213, no. 12, pp. 2304-2311, 2013.

[83] Johnson, G.R. and Cook, W.H., "A constitutive model and data for metals subjected to large strains, high strain rates and high temperatures," *In Proceedings of the 7th International Symposium on Ballistics,* vol. 21, pp. 541-547, 1983.

[84] Johnson, G.R. and Cook, W.H., "Fracture characteristics of three metals subjected to various strains, strain rates, temperatures and pressures," *Engineering fracture mechanics,* vol. 21, no. 1, pp. 31-48, 1985.

[85] B. Crossland, Explosive welding of metals and its application, New York: Oxford University Press, 1982.